VOLUME 9 NUMBER 1-2 2022 ISSN 2409-6121; eISSN 2522-1361

Physical Sciences and Technology

National Nanotechnological Laboratory of Open Type
Institute of Experimental and Theoretical Physics

Physical Sciences and Technology is publishing two number in a year by al-Farabi Kazakh National University, al-Farabi ave., 71, 050040, Almaty, the Republic of Kazakhstan
website: http://phst.kaznu.kz/

Any inquiry for subscriptions should be send to:
Gauhar Mussabek, al-Farabi Kazakh National University
al-Farabi ave., 71, 050040, Almaty, the Republic of Kazakhstan
e-mail: gauharmussabek@gmail.com

SCOPE AND AIM

Physical Sciences and Technology provides an original paperback for the publication of peerreviewed research and review articles in all fields of Physics and related Technology. The topics, included in the scope, especially emphasize understanding of the physics underlying modern technology.

Subject areas may include, but are not limited to the following fields: Astronomy and Space Research, Theoretical Physics and Astrophysics, Plasma Physics and Related Technology, Chemical Physics and Related Technology, Condensed Matter Physics and Related Technology, Thermal physics and Related Technology, Nuclear Physics and Related Technology, Nanomaterials and Nanotechnology, Applied Atomic and Molecular Physics, Material Sciences and Related Technology, Electronics and Related Technology, Instrumentation, Photonics and Quantum Electronics, Signal processing.

The Journal is issued under the auspices of the National Nanotechnological Laboratory of Open Type and Institute of Experimental and Theoretical Physics and is published two times a year by the «Kazakh University» Publishing House. The International Editorial Board of the Journal consists of leading researchers from different countries of the world. The Journal is wide open for contributions that both lie at the far frontiers of contemporary physics and are particularly aimed at applications of the scientific principles of physics to modern technological problems.

IRSTI 29.27.47 https://doi.org/10.26577/phst.2022.v9.i1.01

Ionization cross section of noble gas atoms by electron impact

S. A. Maiorov[1,2*] and R. I. Golyatina[1]

[1]Prokhorov General Physics Institute of the Russian Academy of Sciences, Moscow, Russia
[2]Joint Institute for High Temperatures of the Russian Academy of Sciences, Moscow, Russia
*e-mail: mayorov_sa@mail.ru

(Received 17 January 2022; received in revised form 22 February; accepted 14 March 2022)

The paper presents an analysis of data on the cross sections for ionization by electron impact of noble gas atoms such as hydrogen, helium, neon, argon, krypton and xenon. For the selected sets of experimental and theoretical data an analytical formula is proposed, based on separate accounting for the knockout of electrons from the outer and inner shells, and the corresponding approximation coefficients are selected. By single-term and two-term analytical dependences, approximation errors and coefficients of the ionization cross sections of noble gas atoms were obtained. The obtained semi-empirical formula reproduces the values of the ionization cross sections in a wide range of energies with an accuracy of several percent. Energy dependence of the ionization cross section for an electron collision with a noble gas atoms were calculated and compared with available experimental data. The analysis of the approximation coefficients makes it possible to reduce the influence of errors in the initial experimental data and significantly increase the accuracy of estimating the ionization cross sections.

Key words: electron atomic collisions, ionization cross section, approximation of cross sections, noble gases.
PACS numbers: 34.80.Bm, 34.80.Dp, 51.50.+v, 52.80.Dy.

1 Introduction

The bibliography on cross sections of electron-atomic collisions has thousands of works, and probably an exhaustive review and selection of data is contained in the works [1–6]. However, it should be borne in mind that a critical analysis of the results of experimental data in the review work is very difficult due to the fact that the errors given in the original works of the order of 1–3% differ from each other sometimes by 50%. Therefore, in the review work, only a comparative analysis of the results obtained is really possible, which shows that at best, the relative errors of measuring cross sections are of the order of 5–10%, and more often 20–50%, sometimes reaching 100%.

The most convenient form of presenting experimental and computational-theoretical data is the selection of analytical approximations for them. We began a critical analysis and assessment of the cross sections for electron scattering by atoms of noble gases and vapors of some metals in a wide range of energies in [16–20], where approximations were proposed for the cross sections of elastic and inelastic collisions of electrons with rare gas atoms. Ionization by electron impact from the ground state of the atom is the most common method for the formation and maintenance of a gas-discharge plasma. From a large number of experimental and calculated data on the cross sections for ionization of atoms by electron impact, we have chosen by comparative analysis such data that allowed us to significantly expand the range of applicability of the proposed analytical dependences.

2 Approximation of the ionization cross section

The formulation of the problem of finding an analytical approximation of the ionization cross section of an atom by an electron impact is based on the use of known analytical estimates, the results of experimental measurements and numerical quantum mechanical calculations. In 1912, Thomson proposed the dependence of the ionization cross-section on the electron energy of the following form [21]:

$$\sigma_{ionization}(\varepsilon) = \frac{\pi e^4}{\varepsilon}\left(\frac{1}{I} - \frac{1}{\varepsilon}\right) \equiv 4\pi a_0^2 \frac{Ry^2(\varepsilon - I)}{I\varepsilon^2}, \quad (1)$$

which is obtained for the case of a stationary valence electron at the energy of the incident electron $\varepsilon > I$. Here, e is elementary charge, I is the first ionization potential, a_0 is Bohr radius, Ry is ionization energy of a hydrogen atom. Formula (1) gives a linear increase in the ionization cross section at a small excess of the collision energy over the ionization potential and reaches the maximum value $\sigma_{\max} = \pi e^4 / 4I^2 = \pi a_0^2 (Ry / I)^2$ at the energy of the incident electron $\varepsilon = 2I$, Ry=13.6 eV, $\sigma_0 = \pi e^4 = \pi a_0^2 = 0.876 Å^2$.

The first experiments on measuring the dependence of the ionization cross section on the energy showed that, in full accordance with Thomson formula (1), the initial part of the curve is described fairly well by a linear function up to energies of the incident electron $\varepsilon<2I$. But the maximum ionization cross section for all inert gases lies in the energy range $\varepsilon \in (3I, 7I)$. For the first time, a semi-empirical formula for approximating the initial part of the dependence of the ionization cross section on the energy of the incident electron was proposed by Compton and van Voorhees in 1925 [22]:

$$\sigma_{ionization}(\varepsilon) = C_i(\varepsilon - I), \quad I < \varepsilon < 2I.$$

Wannier proposed a power-law dependence with an exponent of 1.127 to approximate the initial part:

$$\sigma_{ionization}(\varepsilon) = C_i(\varepsilon - I)^{1.127}, \quad \varepsilon > I,$$

which takes into account the interaction of the incident and bound electrons [23, 24].

The first ionization potential I can serve as the natural scale of energy in the collision of an electron with an atom; therefore, it is convenient to go over to the dimensionless energy $x=\varepsilon/I$. In our works [17-20] for atoms of noble gases, hydrogen and some metals, a formula is proposed for the cross section of ionization of an atom by electron impact with three approximation coefficients α, β, γ:

$$\sigma_{ionization}(x) = \frac{\alpha \Delta x}{(1 + \beta \Delta x)^{\gamma}}, \quad (2)$$

где $x=\varepsilon/I$, $\Delta x = x - 1$, $x > I$. For $\alpha = 4\pi a_0^2 (Ry / I)^2$, $\beta = 1$, $\gamma = 2$ it coincides with Thomson's formula (1). The errors of approximation of experimental data by analytical dependence (2) for noble gases and vapors of some metals are in the range of 3-7%, which corresponds in order of magnitude to the errors of the experiments themselves. The maximum cross-section value according to (2) is achieved at $\Delta x = 1/(\beta(\gamma - 1))$.

To approximate the functional dependences of the cross sections on the collision energy, the sum of the series is often used, and the number of terms of the series used can be quite large. At a sufficiently high electron energy, ionization of the atom due to the knocking out of electrons from the inner shells of the atom can play a significant role. To take this factor into account, Lotz in [25-27] analyzed the experimental and theoretical data existing at that time and, within the framework of the shell model of the atom, proposed a formula that has the form

$$\sigma_{ionization}(\varepsilon) = \\ = \sum_1^n a_i q_i (1 - b_i \exp(-c_i \Delta x_i)) \ln(x_i)/x_i, \quad (3)$$

where q_1 is a number of electrons on the outer shell, q_i is the number of electrons on the next i-th inner shell, I_1 – first ionization potential of an atom, I_i is an ionization energy from the i-th inner shell of the atom, $x_i = \varepsilon / I_i$, $\Delta x_i = x_i - 1$, $x_i > 1$, a_i, b_i, c_i – fitting parameters. When using two or three terms of series (3), he obtained the coefficients of approximation of experimental data with an accuracy of 10-20%.

In this work, an attempt is made to take into account the ionization of an atom due to the knocking out of electrons from the inner shells on the basis of our earlier proposed formula (2). A logical way to take into account this ionization channel is to use a two-term approximation, in which the first term corresponds to ionization from the outer shell, and the second term describes ionization from the second shell

$$\sigma_{ionization}(\varepsilon) = q_1 \frac{\alpha_1 \Delta x_1}{(1 + \beta_1 \Delta x_1)^{\gamma_1}} + q_2 \frac{\alpha_2 \Delta x_2}{(1 + \beta_2 \Delta x_2)^{\gamma_2}}, \quad (4)$$

where $x_1 = \varepsilon / I_1, \Delta x_1 = x_1 - 1, x_1 > 1$, and $x_2 = \varepsilon / E_2, \Delta x_2 = x_2 - 1, x_2 > 1$.

If we put all the fitting coefficients to be the same for both shells, then in the two-term approximation we obtain a formula with three fitting coefficients α_0, β_0, γ_0:

$$\sigma_{ionization}(\varepsilon) = q_1 \frac{\alpha_0 \Delta x_1}{(1+\beta_0 \Delta x_1)^{\gamma_0}} + q_2 \frac{\alpha_0 \Delta x_2}{(1+\beta_0 \Delta x_2)^{\gamma_0}} \quad (5)$$

To determine the coefficients α_0, β_0, γ_0, the problem of minimizing the root-mean-square deviation of the cross sections from their experimental values was solved by the standard method of coordinate descent:

$$\Delta^2 = \frac{1}{N} \sum_{i=1}^{N} \left[\frac{\sigma_{fit}(x_i) - \sigma_{\exp}(x_i)}{\sigma_{\exp}(x_i)} \right]^2,$$

where $\sigma_{\exp}(x_i)$ – experimental values in points x_i: $i=1,...,N$, and $\sigma_{fit}(x_i)$ – cross-section values calculated by approximating functions. Minimizing the relative error instead of minimizing the absolute value of the error makes it possible to more correctly take into account the statistical weight of the cross sections at low and high electron energies, when the absolute values of the cross sections are small. However, the choice of optimization based on relative rather than absolute error leads to a greater error in determining the position of the maximum value of the ionization cross section. And in experiments it is the maximum value of the ionization cross section that is most accurately measured.

Table 1 shows the characteristics of noble gas atoms from [26-27] and experimental data on the measurement of ionization cross sections from [28-30]: the symbol and number of the atom, the static polarizability coefficient of the atom K_0, the first ionization potential I1 and the ionization potentials of the atom I_2, I_3 from the next two (second and third) inner shells, the number of electrons q_1, q_2 and q_3 on the outer and next two inner shells, as well as the energy range for which the experimental values of the ionization cross sections were obtained, their number, our estimate of the experimental data error, and a reference to the source of the experimental data.

Note that the energy of the first ionization of an atom due to the knocking out of electrons from the inner shells of an atom is usually slightly higher than the energy of the second ionization potential, i.e. the ionization potential of a singly ionized atom. Binding energies have been taken from paper [27]. A helium atom has two electrons forming one shell (q_1=2, q_2=0), therefore, for helium, formula (5) is a one-term approximation.

Table 1 – Characteristics of atoms and experimental results on measuring the ionization cross sections of noble gases

Atom characteristics								Experiment Data			
Symbol, Number	**K_0,a^3_0**	**I_1, eV**	**I_2, eV**	**I_3, eV**	**q_1**	**q_2**	**q_3**	**$\varepsilon_1 \div \varepsilon_N$, eV**	**N**	**Δ, %**	**Ref.**
H, 1	4.5	13.6	-	-	1	-	-	15- 4000	10	2%	Shah, 1987
He, 2	1.383	24.587	-	-	2	-	-	30 – 4000	21	2-3%	Heer, 1977
Ne, 10	2.68	21.564	48.5	869.5	6	2	2	30 – 4000	21	7%	Heer, 1979
Ar, 18	11.08	15.759	29.2	247.7	6	2	6	20 – 4000	22	6%	Heer, 1979
Kr, 36	16.74	13.996	27.5	93.7	6	2	10	20 – 4000	22	7%	Heer, 1979
Xe, 54	27.06	12.127	23.4	68.1	6	2	10	15 – 4000	23	11%	Heer, 1979

3 Results

The results of approximation of the ionization cross sections of noble gas atoms by electron impact by analytical dependencies (2) and (5) with three fitting coefficients are shown in Table 2. For comparison, there are also given the parameters of approximation of the ionization cross section of the hydrogen atom in the one-term approximation according to formula (2). In addition to the values of the approximation coefficients for these two approximations, the relative root-mean-square approximation errors for the single-term Δ_1 and two-term Δ_2 approximations are also given.

Table 2 – Coefficients and errors of approximation of the ionization cross sections of noble gas atoms by single-term and two-term analytical dependences

	α, Å^2	α_0, Å^2	β	β_0	γ	γ_0	Δ_1, %	Δ_2, %
H	0.827	-	0.351	-	1.91	-	2.0%	-
He	0.365	-	0.287	-	-	1.92	2.8%	-
Ne	0.383	0.0675	0.152	0.204	1.92	1.92	7.0%	7.3%
Ar	2.92	0.452	0.285	0.321	1.86	1.92	2.8%	5.5%
Kr	3.51	0.523	0.269	0.270	1.80	1.92	2.9%	7.4%
Xe	4.30	0.588	0.259	0.230	1.76	1.92	6.2%	11%

The results of the search for the minimum of the approximation error for the two-term approximation showed that for all gases the exponent is practically the same and its value is approximately equal to 1.92. Therefore, the parameter γ was fixed and set equal to 1.92, and the error was optimized for only two parameters.

Figures 1 – 5 show the plots of the ionization cross sections for all considered inert gases: helium, neon, argon, krypton and xenon, respectively. On each plot, the experimental data are marked with circles, the two-term analytical approximations are solid curves, the single-term ones are dashed lines, and the cross-section components corresponding to ionization from different shells in the two-term approximation (5) are dash-dotted lines. The splitting of the cross sections into ionization from the first and second shells shown in the plots for neon, argon, krypton, and xenon clearly shows the physical validity of the two-term approximation.

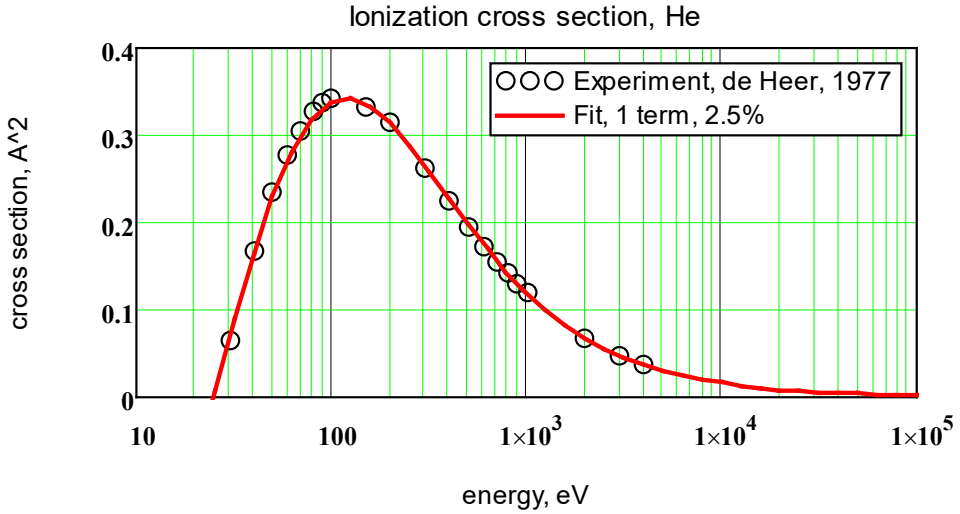

Figure 1 – Energy dependence of the ionization cross section for an electron collision with a helium atom: circles – experimental data, solid curve – approximation in the one-term approximation with a rms relative deviation of 2.5%

In a helium atom, the entire electronic system consists of two electrons, which form only one – the outer shell. The approximation of the cross section by two terms (4) with six fitting parameters and $I_1 = E_2 = 24.587\ eV$ leads to a very insignificant decrease in the relative error – from 2.8% to 2.1%. Obviously, such a decrease in the error when using a two-term approximation with six parameters is due to an increase in the number of fitting coefficients from three in formula (2) to six in formula (5). On this basis, we estimate the error of the experimental data [29] for helium at 2–3%. The maximum cross-section value according to (2) is achieved at $\Delta x = 1/(\beta(\gamma - 1)) \approx 1/\beta$. Accordingly, for the found approximation of the cross section, its maximum is 0.34 Å^2 and is reached at an energy of 125 eV.

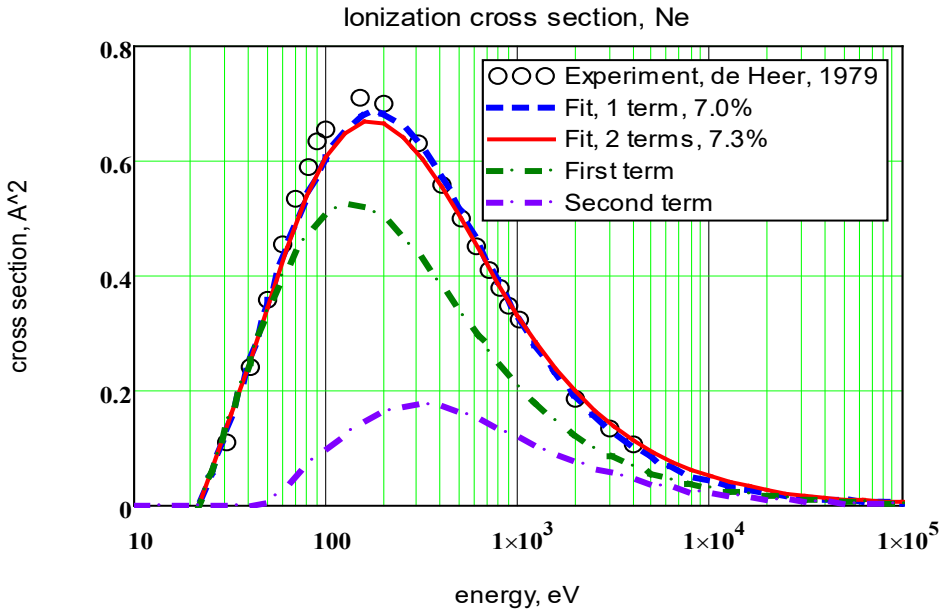

Figure 2 – Energy dependence of the ionization cross section for an electron collision with a neon atom: circles – experimental data, dashed and solid curves – approximation in the one-term and two-term approximations, dash-dotted curves – the first and second terms of the approximation

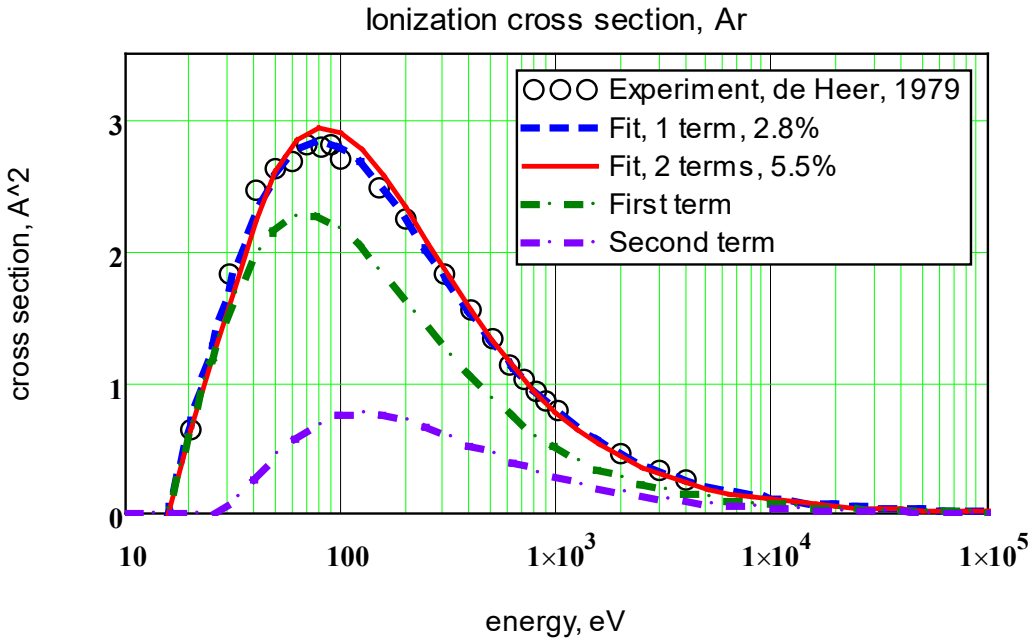

Figure 3 – Energy dependence of the ionization cross section for an electron collision with a argon atom

The neon atom has three shells – the outer shell has 6, the second and the inner one also have two electrons (10 in total). Ionization from the third shell is insignificant due to the large ionization potential – 869 eV. The approximation of the cross section in the two-term approximation leads to an insignificant

increase in the relative error – from 7% to 7.3%. According to the found approximation of the cross section, its maximum is 0.67 Å^2 and is reached at an energy of 160 eV. We estimate the error of experimental data [30] for neon at 7%.

The argon atom has 6 and 2 electrons on the outer and next inner shells, respectively, and the remaining shells closest to the nucleus are clearly not taken into account in the two-term approximation. Argon has six electrons on the third shell with an ionization potential of 248 eV. When choosing the approximation coefficients, naturally, their contribution to ionization is taken into account through the contribution of the experimentally measured cross sections. We estimate the error of experimental data [30] for argon at 6%. According to the found approximation, the maximum value of the cross section is 2.9 Å^2 and is reached at an energy of 90 eV.

The krypton atom has 6 and 2 electrons on the outer and next inner shells, respectively. As in argon, ionization of the shells closest to the nucleus affects the asymptotics of the dependence of the ionization cross section at high energies. In the two-term approximation, their influence is not explicitly taken into account. On the third shell, krypton has ten electrons with an ionization potential of 93.7 eV. Therefore, ionization from the third shell for krypton has a large effect on the ionization cross section near the maximum. In addition, after knocking out an electron from the third shell, autoionization of an electron from the outer shell is possible. To improve the accuracy for krypton and xenon, it is necessary to take into account the ionization from the third shell, i.e. use the three-term approximation [25]. However, when choosing the approximation coefficients and in the two-term approximation, their contribution to the ionization of the atom is naturally taken into account, since their contribution is present in the experimentally measured cross sections. We estimate the error of experimental data [30] for krypton at 7%. According to the found approximation of the cross section, its maximum is 3.9 Å^2 and is reached at an energy of 85 eV.

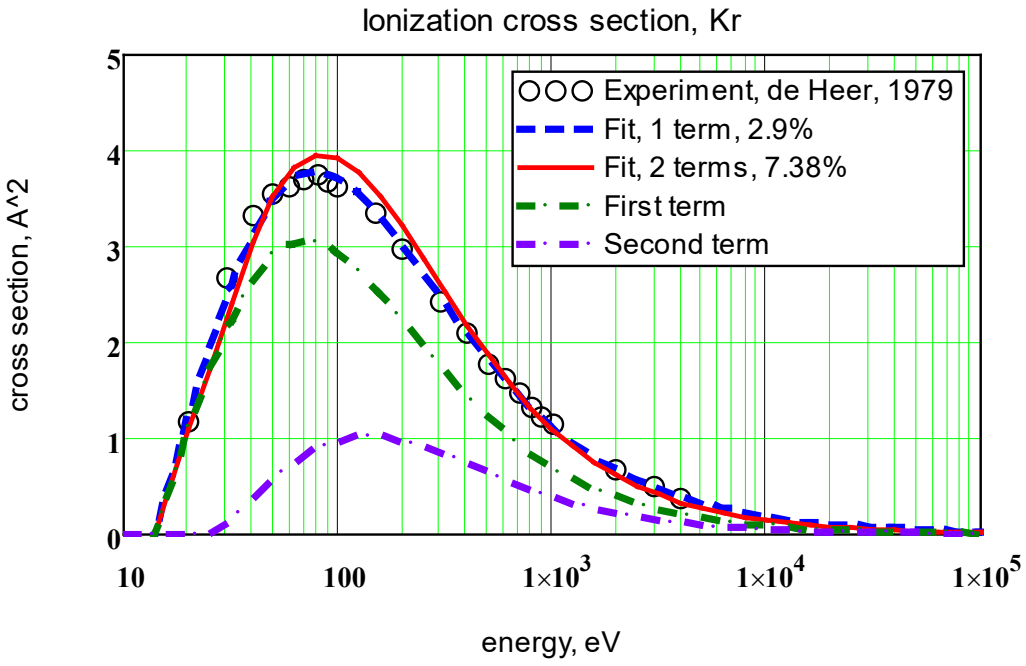

Figure 4 – Energy dependence of the ionization cross section for an electron collision with a krypton atom

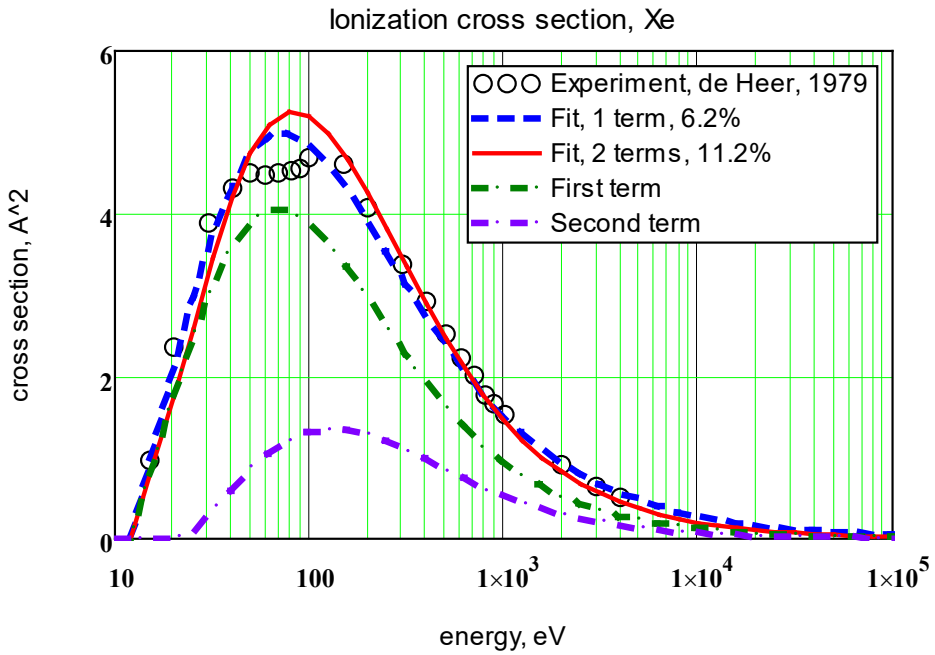

Figure 5 – Energy dependence of the ionization cross section for an electron collision with a xenon atom

The xenon atom has 6 and 2 electrons on the outer and next inner shells, respectively. On the third shell, xenon, like krypton, has ten electrons with an ionization potential of 68.1 eV. Therefore, ionization from the third shell for xenon has a large effect on the ionization cross section near the maximum. In addition, after knocking out an electron from the third shell, autoionization of an electron from the outer shell is possible. Ionization by knocking out electrons from deep shells strongly affects the asymptotics of the dependence of the cross section at high energies. The approximation of the cross section in the two-term approximation leads to an increase in the relative error from 6.2% to 11.2%; therefore, we estimate the error of the experimental data [30] for xenon at 11%. According to the found approximation of the cross section, its maximum is 5.2 Å^2 and is reached at an energy of 80 eV.

4 Conclusions

As follows from the data presented in the tables, the use of a two-term approximation purely formally leads to a significant increase (up to two times) in the error in approximating experimental data by analytical dependences. However, the addition of the second term is not accompanied by the addition of new adjustable constants – their number is still three. It can be assumed that a physically more adequate model, which takes into account the ionization of strongly bound electrons from the inner shells, gives more accurate data on real cross sections. The answer to this question can be obtained by analysis and comparison with various experimental data and the transition to consideration of other elements [31, 32]. In particular, for alkaline earth metals, which have only one electron on the outer shell, the effect of ionization from the inner shells will be greatest. Such a study is planned for the future.

The analysis of the obtained analytical dependences of the ionization cross sections of inert gas atoms by electron impact, together with the analysis of the corresponding experimental data, allows us to draw several important and interesting conclusions:

1. Since helium has only one electron shell, the variation of the coefficients of the first and second terms of the approximation for helium can apparently serve as an additional estimate of the experimental error. For helium an increase in the number of expansion terms from one to two does not lead to any noticeable increase in accuracy,

which indicates that the error is apparently caused not by the functional form of formula (2), but by errors in the experimental data.

2. In contrast to the one-term approximation (2), when using an approximation that takes into account ionization from the second shell, the value of the parameter γ can be chosen the same for all elements and equal to 1.92.

3. The division of the cross sections into ionization from the first and second shells shown in the graphs for neon, argon, krypton and xenon clearly indicates the physical validity of the two-term approximation. Therefore, the carried out mathematical processing of the experimental data makes it possible to achieve a significant increase in the accuracy in determining the cross sections by finding the analytical dependences obtained from the experimental data.

4. In addition, the analysis of the approximation parameters makes it possible to find their values for elements for which there are no experimental data.

References

1. E. Carbone, W. Graef, G. Hagelaar, D. Boer, M. Hopkins, J. Stephens, B. Yee, S. Pancheshnyi, J. van Dijk, L. Pitchford. Data needs for modeling low-temperature non-equilibrium plasmas: The LXC at project, history, perspectives and a tutorial // Atoms. – 2021. – Vol. 9. – P. 16. https://doi.org/10.3390/atoms9010016

2. A. Zecca, G.P. Karwasz, R.S. Brusa. One century of experiments on electron-atom and molecule scattering: A critical review of integral cross-sections // Riv. Nuovo. – 1996. – Vol. 19. – No 3. – P. 1. https://doi.org/10.1007/BF02742990

3. S. Pancheshnyi, S. Biagi, M.C. Bordage, G.J.M. Hagelaar, W.L. Morgan, A.V. Phelps, L.C. Pitchford. The LXCat project: Electron scattering cross sections and swarm parameters for low temperature plasma modeling // Chemical Physics. –2012. –Vol. 398. –P. 148. https://doi.org/10.1016/j.chemphys.2011.04.020

4. Z. Petrovic´, S. Dujko, D. Maric´, G. Malovic´, Z˘. Nikitovic´, O. Šašic´, J. Jovanovic´, V. Stojanovic´, M.J. Radmilovic´-Radenovic´. Measurement and interpretation of swarm parameters and their application in plasma modelling // J. Phys. D: Appl. Phys. –2009. –Vol. 42. –P. 194002. https://doi.org/10.1088/0022-3727/42/19/194002

5. J. Dutton. A survey of electron swarm data. // Journal of Physical and Chemical Reference Data. – 1975. – Vol. 4. –P. 577. https://doi.org/10.1063/1.555525

6. R. Campeanu. Electron impact ionization of helium, neon and argon at intermediate energies // Phys. Astron. Int. J. – 2019. –Vol. 3(6). –P. 230–233. https://doi.org/10.15406/paij.2019.03.00188.

7. M. Hahn, A. Müller, D. W. Savin. Electron-impact multiple-ionization cross sections for atoms and ions of helium through zinc // Astrophys. J. –2017. –Vol. 850. –P.122. https://doi.org/10.3847/1538-4357/aa9276

8. Sh. Ravinder, .P. Sharma S, K. Naveen. Electron impact ionization cross section – semi-empirical approach // Bulletin of Pure & Applied Sciences –2017. –Vol. 36 C (Chemistry) –P. 45–53. https://doi.org/10.5958/2320-320X.2017.00006.1

9. M.H. Belgacem, E. Guedda, H. Jelassi. Ionization cross section by electron impact of helium-like ions // Canadian Journal of Physics. –2021. –Vol. 99. No.– 11. –P. 969-974. https://doi.org/10.1103/PhysRevA.22.111

10. Y.H. Li. Ionization cross sections by electron impact for single ionization from the atomic ground state // Advanced Materials Research – 2014.– Vol. 998 – 999. –P.140–143. https://doi.org/10.4028/www.scientific.net/AMR.998-999.140

11. H. Tawara, T. Kato. Total and partial ionization cross sections of atoms and ions by electron impact // Atomic Data and Nuclear Data Tables – 1987.– Vol. 36. – P. 167-353. https://doi.org/10.1016/0092-640X(87)90014-3

12. M.S. Pindzola, F. Robicheaux, J.P. Colgan, M.C. Witthoeft, J.A. Ludlow. Electron-impact single and double ionization of helium // Phys. Rev. A. –2004. –Vol. 70. –P. 032705. https://doi.org/10.1103/PhysRevA.70.032705

13. P. L. Bartlett, A. T. Stelbovics. Calculation of electron-impact total-ionization cross sections // Phys. Rev. A. – 2002.– Vol. 66(1). – P. 012707. https://doi.org/10.1103/PhysRevA.66.012707

14. I.D. Kaganovich, E. Startsev, R. C. Davidson. Scaling and formulary of cross-sections for ion–atom impact ionization // New J. Phys. – 2006. – Vol. 8. -P. 278. https://doi.org/10.1088/1367-2630/8/11/278

15. X.Llovet, C.J. Powell, F. Salvat, A. Jablonski. Cross sections for inner-shell ionization by electron impact // Journal of Physical and Chemical Reference Data – 2014. – Vol. 43(1). – P. 013102. https://doi.org/10.1063/1.4832851

16. N.N. Skvortsova, S.A. Maiorov, D.V. Malakhov, V.D. Stepakhin, E.A. Obraztsova, A.I. Kenzhebekova, O.N. Shishilov. On the dust structures and chain reactions induced over the regolith by gyrotron radiation // JETP Lett. – 2019. – Vol. 109. P. 441–448. https://doi.org/10.1134/S0021364019070130

17. R.I. Golyatina, S.A. Maiorov. Analytical approximation of cross sections of collisions of electrons with atoms of inert gases. // Phys. Sci. Technol. – 2021. – Vol. 8. P. 4–13. https://doi.org/10.26577/phst.2021.v8.i1.01

18. R.I. Golyatina, S.A. Maiorov. Analytical cross section approximation for electron impact ionization of alkali and other metals, inert gases and hydrogen atoms. // Atoms. – 2021. – Vol. 9. – P. 90. https://doi.org/10.3390/atoms9040090

19. R.I. Golyatina, S.A. Maiorov. Analytical approximation of cross sections of collisions of electrons with inert gas atoms // Plasma Phys. Rep. – 2022. – Vol. 46(2) – P.3–13. https://doi.org/10.51368/2307-4469-2021-9-4-298-309

20. R.I. Golyatina, S.A. Maiorov. Characteristics of electron drift in an Ar–Hg mixture // Plasma Phys. Rep. – 2018. – Vol. 44– P. 453–457. https://doi.org/10.1134/s1063780x18040050

21. J.J. Thomson. XLII. Ionization by moving electrified particles. The London, Edinburgh, and Dublin. // Philos. Mag. J. Sci. – 1912. – Vol. 23. – P. 449–457. https://doi.org/10.1080/14786440408637241

22. K.T. Compton, C.C. Van Voorhis. Probability of ionization of gas molecules by electron impacts. II Critique. // Phys. Rev. – 1926. – Vol. 27. – P. 724–731. https://doi.org/10.1103/PhysRev.27.724

23. G.H. Wannier. The threshold law for single ionization of atoms or ions by electrons // Phys. Rev. – 1953. – Vol. 90. – P. 817–825. https://doi.org/10.1103/PhysRev.90.817

24. M. Gryziński. Two-particle collisions. I. General relations for collisions in the laboratory system // Phys. Rev. – 1965. – Vol. 138. – P. A305–A321. https://doi.org/10.1103/PhysRev.138.A305

25. W. Lotz. An empirical formula for the electron-impact ionization cross-section // Zeitschrift fur Physik. – 1967. – Vol. 206. – P. 205-211. https://doi.org/10.1007/BF01325928

26. W. Lotz. Electron-impact ionization cross-sections for atoms up to Z=108. // Z. Physik. – 1970. – Vol. 232. – P. 101- 107. https://doi.org/10.1007/BF01325928

27. W. Lotz. Ionization potentials of atoms and ions from hydrogen to zinc // J. Opt. Soc. Am. – 1967. – Vol. 57(7). – P. 873 – 878. https://doi.org/10.1364/JOSA.57.000873

28. M.B. Shah, D.S. Elliot, H.B. Gilbody. Pulsed crossed-beam study of the ionisation of atomic hydrogen by electron impact // J. Phys. B At. Mol. Phys – 1987. – Vol. 20. – P. 3501–3514. https://doi.org/10.1088/0022-3700/20/14/022

29. F. J. de Heer, R. H. J. Jansen. Total cross sections for electron scattering by He. // J. Phys. B: Atom. Mol. Phys. – 1977. – Vol. 10. – P. 3741–3758. https://doi.org/10.1088/0022-3700/10/18/030

30. F. J. de Heer, Jansen R. H. J., W. van der Kaay. Total cross sections for electron scattering by Ne, Ar, Kr and Xe // J. Phys. B: Atom. Mol. Phys. – 1979. – Vol. 12. – P. 979–1002. https://doi.org/10.1088/0022-3700/12/6/016

31. F. Blanco, F.F. da Silva, P. Limão-Vieira, G. García. Electron scattering cross section data for tungsten and beryllium atoms from 0.1 to 5000 eV // Plasma Sources Sci. Technol. –2017. – Vol. – 26. – P. 085004. https://doi.org/10.1088/1361-6595/aa7b02

32. J.M. Rost, T. Pattard. Analytical parametrization for the shape of atomic ionization cross sections // Phys. Rev .A – 1997. – Vol. 55(1). – P. R5–R7. https://doi.org/10.1103/PhysRevA.55.R5

Funded by Al-Farabi KazNU

IRSTI 27.35.51 https://doi.org/10.26577/phst.2022.v9.i1.02

Effect of laminar and turbulent flow on the collective motion of plasma microdischarges at atmospheric pressure

A.I. Ashirbek[1*], E.A. Usenov[1,2], M.K. Dosbolaev[3], M.T. Gabdullin[4] and T.S. Ramazanov[3]

[1]Institute of Applied Science and Information Technologies, Almaty, Kazakhstan
[2]NNLOT, Faculty of Physics and Technology, Al-Farabi Kazakh National University, Almaty, Kazakhstan
[3]IETP, Faculty of Physics and Technology, Al-Farabi Kazakh National University, Almaty, Kazakhstan
[4]Kazakhstan-British Technical University, Almaty, Kazakhstan
*e-mail: azamat.ashirbeck@gmail.com
(Received 25 January 2022; received in revised form 12 March; accepted 5 April 2022)

Dielectric barrier discharge (DBD) is used for many important applications in various sectors of science and technology. For example, for ozone generation, surface modification of polymers, in plasma medicine, and for decomposition of heavy volatile organic compounds. Nowadays, one of the actual problems is getting of uniformity of discharge distribution for high quality treatment of materials surfaces. To achieve uniform distribution of the discharge, several methods are available, one is to use different types of noble gases, and another is to use AC power supply with frequency varied in wide range. But besides this, another of the potential methods for obtaining a uniformly distributed discharge is to blow through the discharge gap flow of air. This method was used in this paper to conduct experiments which consisted of oscilloscoping voltage and current values, high-speed imaging, also gas flow simulation for comparison with the experiments. The obtained results show the dynamics of microdischarge motion in laminar and turbulent flow regimes, which supported by flow simulation.

Key words: plasma, dielectric barrier discharge, gas flow, gas flow modelling, microdischarges.
PACS numbers: 34.80.Bm, 34.80.Dp, 51.50.+v, 52.80.Dy.

1 Introduction

Dielectric barrier discharge (DBD), also called ‘’barrier’’ or ‘’silent’’ discharge, is a typical nonequilibrium AC discharge at atmospheric pressure [1]. The most important characteristic of the dielectric barrier discharge is that conditions for the generation of nonequilibrium plasma can be provided much more easily [2] compared to other types of alternative discharges [3] such as low-pressure discharges, high-pressure pulsed discharges or atmospheric pressure uniform arcs. Its simplicity in terms of geometric configuration, operating medium and operating parameters is irreplaceable. The conditions optimized in laboratory experiments can easily be adapted to large industrial equipments. The presence of a dielectric is the key to the limiting the current of the discharge. It limits the charge transported in the discharge, i.e. it limits the current flow into the system and almost uniformly distributes the discharge over the entire electrode area. Recently two main types of DBD designs have been proposed: volume barrier discharge (VBD), and surface barrier discharge (SBD)[4]. VBD consists of two parallel dielectric plates with electrodes mounted externally or two electrodes on one side of the dielectric. SBD device has a dielectric surface with a small but elongated electrode on one side of the dielectric and a metallic electrode coated on the opposite side [5,6]. Such devices are advantageous for industrial use because vacuum equipment can be avoided and DBD-based devices operate in the atmospheric pressure range.

In the electrode gap, following an electrical breakdown, current pulses or a charged plasma channel are generated. These current pulses are shaped like filaments, hence the term “filamentary discharge” could be used. These filament channels are also called microdischarges (MD), because the current through the filaments is very low. The

location of the occurrence of microdischarges on the electrode surface is random. However, after ignition, the microdischarges remain at this point for a long time (periods) – up to 300 half-periods at an applied voltage of 100 kHz (more precisely, the microdischarges slowly move through the monitoring area). This means that the displacement of the microdischarge in one half-period is less than 0.25 μm, which is negligible, compared to the diameter of the microdischarge. Thus, it can be concluded that there is a spatial memory in the microdischarge in the stationary DBD, the microdischarge in each subsequent half-period does not jump to an arbitrary point on the electrode surface, but appears exactly at the point of the surface where it was in the previous half-period. Currently, there is no standard point of view regarding the temporal and spatial 'memory' of microdischarges. The cause of the spatial memory effect for a subsequent microdischarge is the residual surface charge deposited on the barrier by a previous microdischarge. This charge can locally increase the electric field during the next half-period and hence provide a gas breakdown (i.e. the occurrence of a subsequent MD), preserving the site of occurrence.

The influence of air (gas) flow on the dynamics of MD channels in DBD is of great interest both from the point of view of fundamental research and for solving applied problems. At present one of the urgent tasks is to obtain uniform discharge distribution in DBD for high quality treatment of material's surfaces. To obtain such a discharge distribution there are several approaches, one of them is to use various types of noble gases and the other is to use AC power supply with high frequency. But apart from this, another potential method to obtain a uniformly distributed discharge in DBD is by blowing out the discharge gap with an air flow [7-10]. DBD in a gas flow is actively used in so-called cold plasma jets (cold plasma jets) in the field of plasma medicine and surface treatment of various materials. The presence of gas flow in the discharge gap allows efficient cooling of the discharge walls and the plasma channel itself to room temperature and controlling plasma chemical processes to obtain the desired biologically active components. Another application of gas flow in DBD is active control of gas flow dynamics in plasma actuators in order to stabilize turbulence at the interface with the surface of solids. These studies are mainly carried out with the help of surface DBD in the air atmosphere and have great perspectives for aeronautical applications [11]. Microdischarge DBD with actively blown gas in the discharge gap is often used in reactors for plasma-chemical decomposition of heavy volatile organic compounds (VOC) [12], for carbon dioxide (CO2) utilization and synthesis gas generation [13], and for dry methane reforming and hydrogen production. From this it can be concluded that studies of the effect of gas flow on the dynamics of micro-discharge channels for different modes of flow itself is an relevant task. In the present work we have carried out experiments to determine the effect of gas flow velocity on the structural and dynamic characteristics of microdischarge channels. Laminar and turbulent modes of blown gas flow into the discharge interval of a DBD with flat-parallel geometry of electrodes were considered. The trajectories of microdischarge channels have been determined by means of video imaging. In case of laminar mode of gas flow, the microdischarge channels move strictly in the central region and follow the direction of gas flow. For the turbulent mode, the presence of vortices in the trajectories of microdischarge channels is revealed. The corresponding gas flows have been simulated with the Comsol Multiphysics software package for specific experimental conditions, and have been compared with real trajectories of MD channels. The results showed that the MD channels completely follow the direction of gas flow in the discharge gap for laminar mode. In the turbulent mode, vortices and backward to the flow collective motion of MD channels are also observed.

2 Experimental set-up

A gas-discharge cell with a flat-parallel configuration, as shown in Figure 1, has been constructed for experiments with DBD. The design of electrodes in discharge cells has a flat geometry and consists of two parallel quartz plates, which play the role of dielectric ($\varepsilon = 3.5$), with parameters of 60mm x 60mm and a height of 2 mm. The air gap between the surfaces of the plates is h = 3 mm. One plate has a transparent conductive glass top coated with indium tin oxide (ITO), and is earthed via a low-inductive current shunt with resistance R = 51 Ohm. An aluminum foil is applied to the back of the second quartz plate and a high voltage from a PVM 500 sinusoidal generator is fed through it. Given the dimensions of the dielectric inserts for fixing the wires, the area of the discharge zone is 40x40 mm^2. The frequency and amplitude of the sinusoidal voltage varies between 20-30 kHz and 10-15 kV respectively.

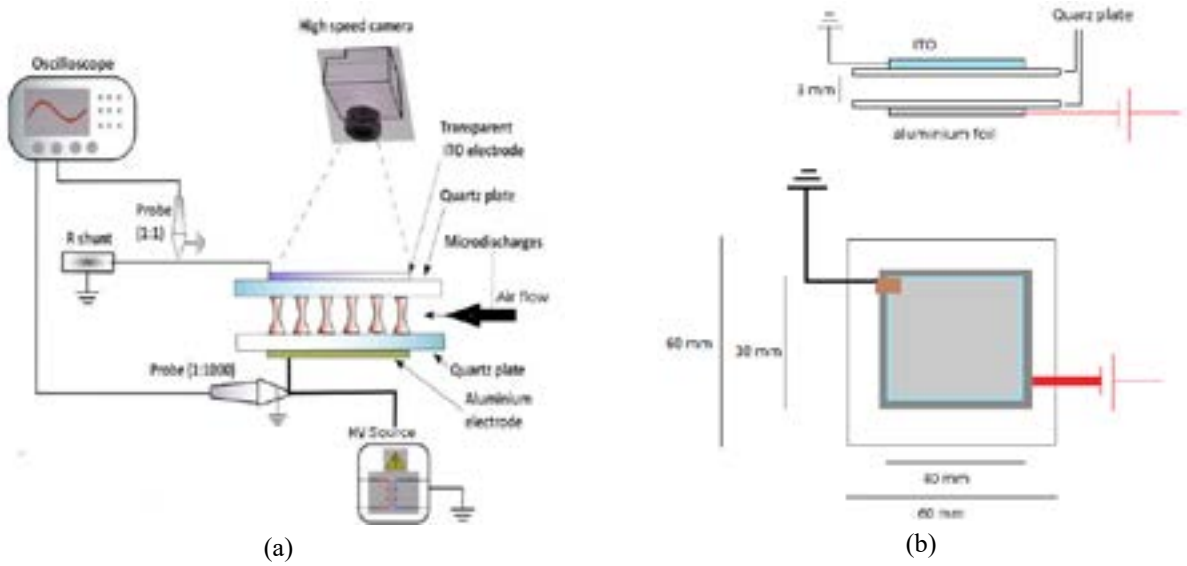

(a) (b)

Figure 1 – Scheme of the experimental setup (a) and geometry of the gas discharge cell (b)

All experiments were performed in a stream of air (at room temperature) directed along the walls of the plate. The gas flow velocity was varied up to 30 m/s inside the cell. Measurement of flow velocity was performed at the cell outlet, using Pitot tube with diameter 0.5 mm, equipped with micromanometer MMN-2400 (5)-1. The schematic in Figure 1 b explains the synchronized operation of a sinusoidal high voltage, a 4 channel digital oscilloscope (LeCroy WJ354A, 500 MHz) and a high-speed camera (Phantom VEO 710S). Microdischarge was photographed, with an overhead view through a transparent ITO conductor and a quartz plate. The whole circuit is started by switching on the key K1, which supplies the high voltage sine wave generator. The signal from the delay generator, received from the power supply, starts the high speed camera at the same moment. The discharge voltage was measured with a Tektronix P6015 high voltage divider (1:1000). The discharge current was measured with a current shunt.

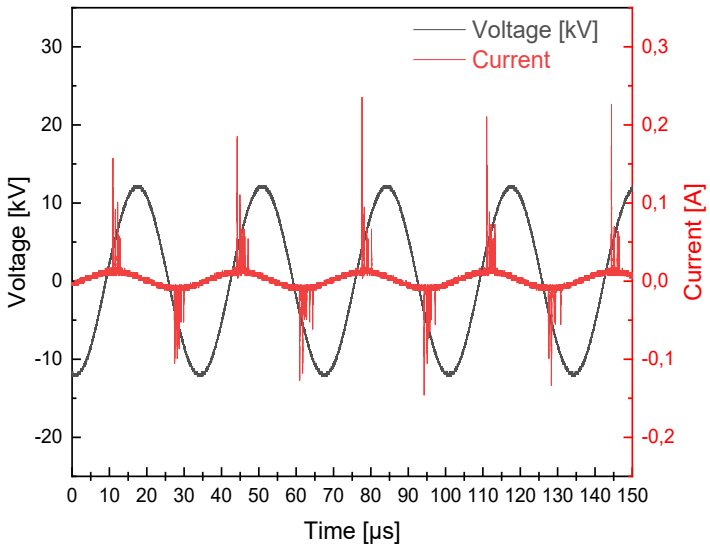

Figure 2 – Typical dynamic volt-ampere oscillogram of the DBD with plane-parallel electrode geometry. Each current spike in the oscillogram corresponds to the occurrence of one or more microdischarge channels

Figure 2 shows a typical voltage and current waveform of a volumetric barrier discharge. From this graph, it can be seen that, the voltage and current were indicated black and red color respectively. The highest number of voltage was approximately 12.5 kV, and with frequency 28.6 kHz. The current consisted of two parts, which involve a sinusoidal part called conductivity current and sharp ends called bias current.

3 Results

The resulting images for DBD without airflow, at h = 3 mm for a flat-parallel electrode geometry are shown in Figure 3. The images were acquired using a high-speed camera with a frequency of 25000 frames per second and an exposure time of 40 μs. Also, the number of microdischarges is calculated from 500 pictures and averaged.

In Figure 3 (a) the voltage U applied to the electrodes is 9.7 kV and the breakdown voltage is 4.8 kV. The average number of microdischarges is equal to 17. Further in the Figure 3 (b) U is equal to 10,45 kV, in this section more or less stable number of microdischarges is formed equal to 31. Increasing the U to 11.61 kV, in figure 3 (c) we get a fully filled gas-discharge cell in which the number of microdischarges is 53. And when U reaches 12.57 kV in a fully filled gas discharge cell more microrischarge appear and so the distance between the microrischarge decreases, as indicated in the Figure 3 (d). It can also be seen that on a maximally filled cell, the arrangement of microdischarges have a strict pattern and is an example of a self-organized structure [14,15].

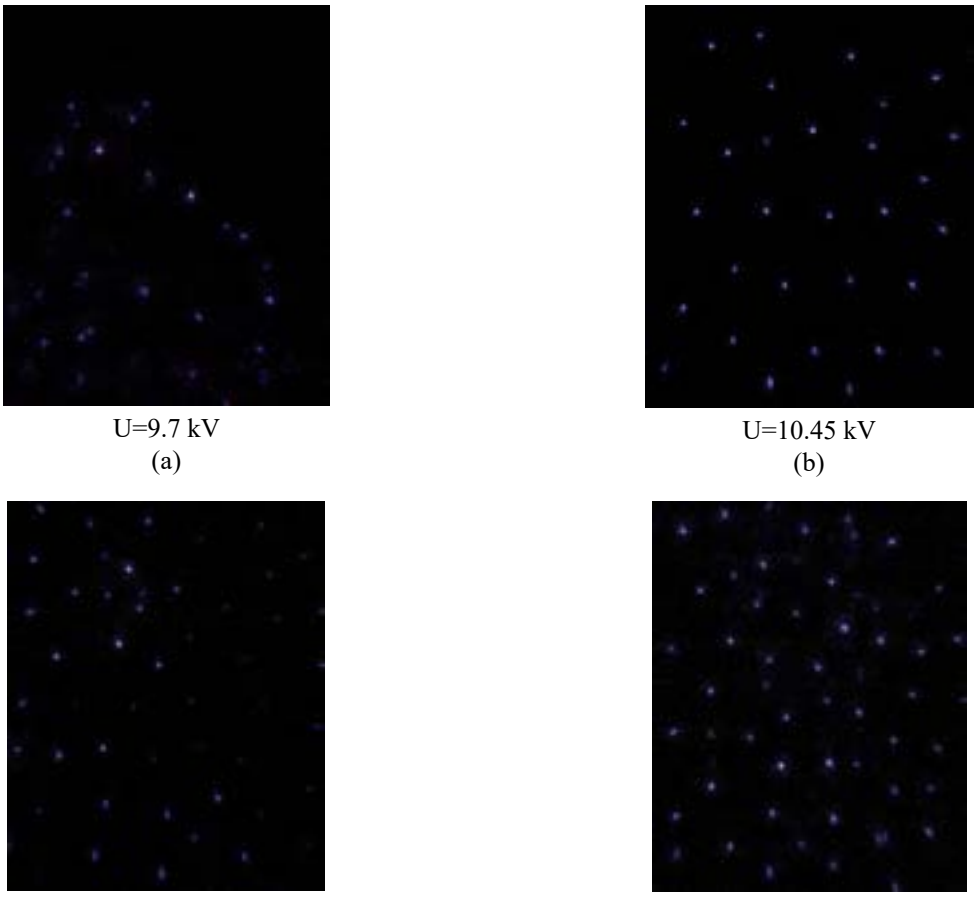

U=9.7 kV (a) U=10.45 kV (b)

U=11.61 kV (c) U=12.57 kV (d)

Figure 3 – Photographs of the VBD (top view) obtained using high-speed video recording without airflow, with different applied voltages, at h = 3 mm. and exposure time of 40 μs

4 Modelling results

When affected by the air flow [16-20], the microdischarges begin to move in the direction of the flow. By observing this phenomenon, it can be seen that depending on the flow velocity, the movement of the microdischarge has a different character. It is known that there are three types of gas dynamic flow regimes, changes between regimes are depended on the flow velocity of the gas. For this geometry, the Reynolds number for all three types of flow modes at certain flow velocities has been calculated. For clarity, microdischarge motions in laminar and turbulent flow are shown in Figure 4 below. In the figure 4 (a), it's first case, the flow velocity is 5 m/s and Reynolds number is 2100, which corresponds to laminar mode. In the figure 4 (b), it's second case, the flow velocity is 30 m/s and Reynolds number is 6200, corresponding to turbulent mode. Both figures were obtained at 24 fps, with an exposure time of 41 ms.

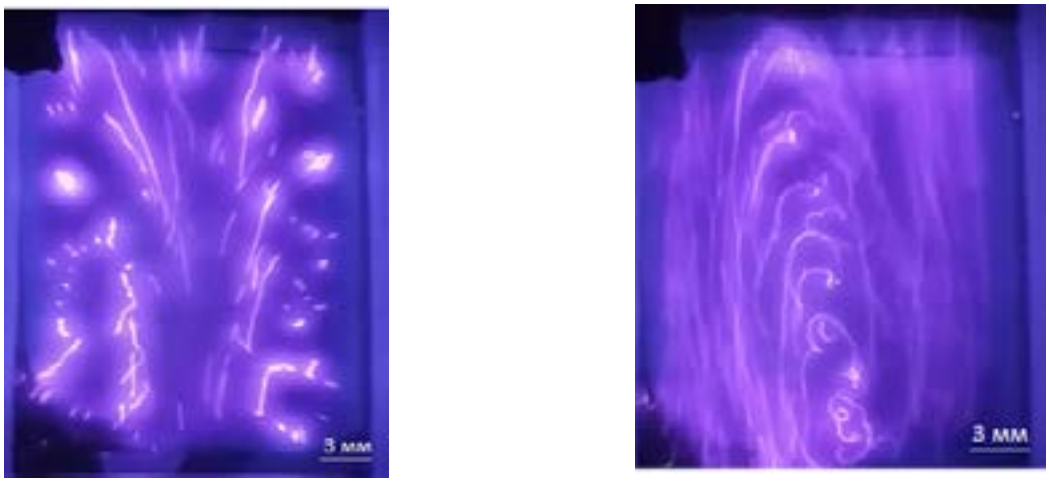

(a) (b)

Figure 4 – MD motion in laminar flow (a) and turbulent flow (b), frame rate 24 fps, exposure time 41 ms

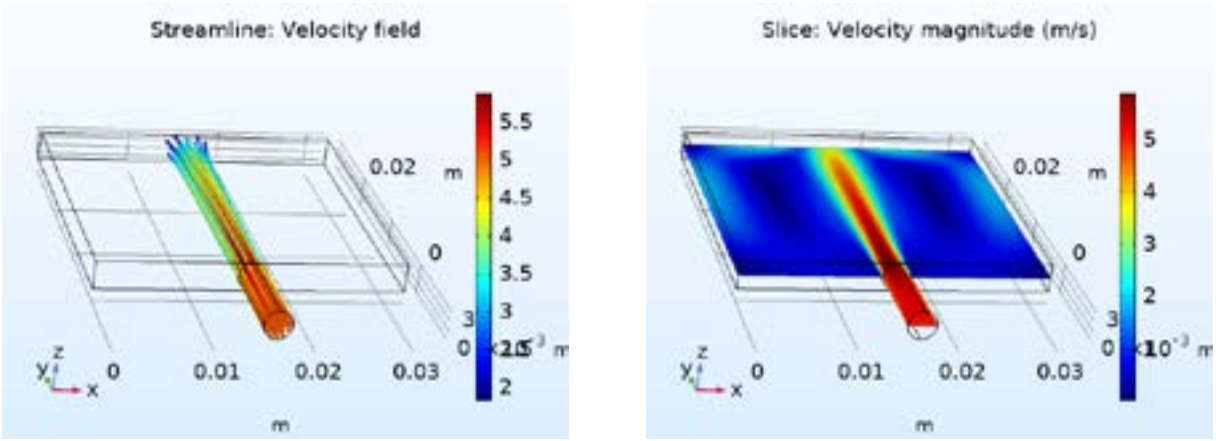

2(a) (b)

Figure 5 – Visualization of airflow in laminar mode, flow lines (a), surface velocity distribution (b)

Gas flow was modelled using the Comsol Multiphysics software. The Computational Fluid Dynamics (CFD) package was used for this purpose. The area between the active electrodes through which air is blown was chosen as the calculation area. The results are shown below as flow visualizations and as graphs.

Figure 5 (a) shows streamlines, i.e. flow lines, and Figure 5 (b) shows the velocity distribution of the gas flow in the interelectrode volume. The velocity values can be determined from the color scale on the right side of both figures. As the simulation results show, the maximum velocity value is 6 m/s. It can be seen from the flow visualization figure that at low velocities, the flow is uniform, but the area covered is limited. That is, the flow lines do not cover the entire inter-electrode area, but only that part which is coaxial to the inlet channel.

An increase in flow velocity leads to a transition from laminar to turbulent gas dynamic mode. Looking in detail at the flow simulation results in the turbulent mode, it can be seen that the flow lines gradually start to shift to the left side, then reaching the edge of the electrodes, passing along it, as shown in Figure 6(a). The velocity distribution itself over the electrode area is shown in Figure 6(b). The average flow velocity is in the range of 30-35 m/s. The flow velocity through the tube at the inlet of the discharge cell is 30 m/s. Further, with expansion of the discharge volume, the flow velocity reduces significantly and reaches 15-20 m/s at the exit through the inter-electrode space. It can also be noticed that near the opposite wall of the discharge cell the flow velocity starts to increase, indicating the occurrence of vortices inside the cell.

On the right edges of both figures are indicators that shows the velocity at a certain point on a color scale. When the gas velocity reaches turbulent values, the movement of the MD is vortex-like, as are the flow lines of the blown air.

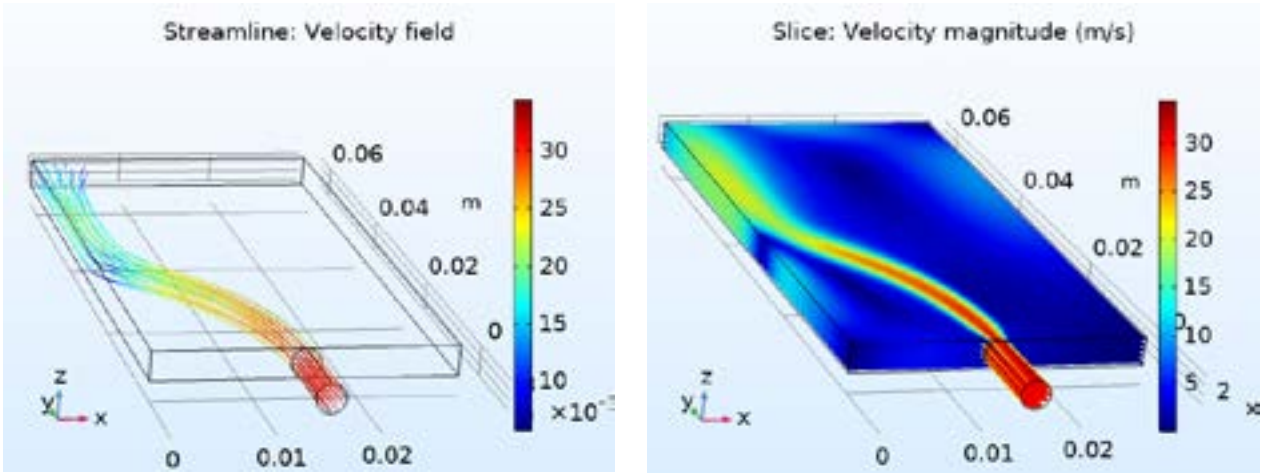

(a) (b)

Figure 6 – Visualization of airflow in turbulent mode.
Flow lines (a) and surface velocity distribution (b)

Figure 7 shows the velocity line cutting plots at different distances from the inlet channel, which are derived from figures 5 (a) and 6 (a). For laminar flow, (Figure 7a) three lines have selected and their positions from electrode width are 10 mm, 20 mm, 30 mm. The inlet channel is located at the position 17 mm of electrode length. As the electrode width position increased, the speed value of flow decreased, it can also be seen in the decrease in velocity peak along the inlet channel axis. At the same time closer to the walls the flow velocity starts decreasing and reaches some peak near the side walls of the discharge cell. At a position 30 mm from electrode width, the gas flow velocity increases along the edges of the main flow and there is a tendency for the flow to be more evenly distributed. For turbulent flow, Figure 7 (b), similar to the first case, 3 lines are chosen, but with different distances from the

electrode widths of 15 mm, 30 mm and 50 mm. It can be seen that the velocity near the inlet channel is at its maximum and then the velocity peak shifts closer to the walls. This observation indicates the presence of eddies in the air flow lines and the formation of backward flow.

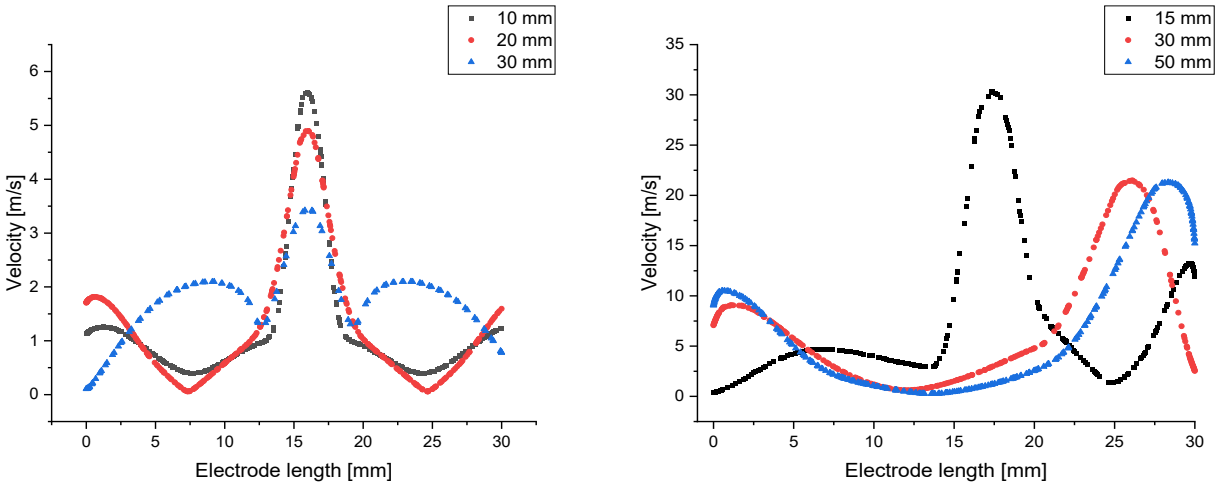

(a) (b)

Figure 7 – Velocity line slice graph at different distances from the inlet channel (a) for laminar flow, (b) for turbulent flow

It is necessary to pay attention to the collective motion of MD's in the discharge gap and the similarity of their trajectory and gas flow lines at different gas-dynamic regimes. The simulation results obtained in laminar mode (Figure 5) completely repeat the trajectory of gas flow lines. The MD channels move only along the central axis of the inlet channel, with only some perturbations away from this axis. In the turbulent regime, the collective motion of MDs has a vortex-like character, which is consistent with the simulation results. In both cases, neutral atoms and molecules of the blown air in the flow transfer momentum to the active particles of the plasma channel (ions, excited atoms) through frequent collisions. In this case, the volume residual charges of the microdischarge channel begin to move along the flow and create a new location of the plasma on the electrode surface. Despite the discrete structure of the microdischarge channels, when imaging with relatively long exposure times, the trajectory and motion of the MD channels appears to be continuous. Our results further confirm the possibility of controlling the collective dynamics of the MD channels by airflow and the importance of gas-dynamic flow regimes for this purpose.

5 Conclusions

Careful analysis of the presented results on DBD microdischarge in gas flow shows that the overall discharge behavior, also the dynamics and structure of the MD completely change with increasing flow rate, as has been shown under different flow regimes. In this paper, results have been obtained on the MD dynamics in a flat surface multi-layer DBD and compared with the flow simulation results on Comsol. The discharges have special electrode arrangements in the form of "flat parallel plate" and are generated by a variable (27-32 kHz) sinusoidal voltage. Rapid visualization of the filaments and their synchronization with electrical diagnostics using an oscilloscope show that the discharge has different phases depending on the flow rate and gas-dynamic regimes. The obtained results of simulation of gas flow in the discharge gap are similar to the movement of MD under different gas-dynamic regimes. Comparison of experimental results with simulation results shows that the microdischarges move uniformly along the flow direction at laminar flow velocities. However, as the flow velocity increases up to turbulent mode, the MD motions have

a vortex-like character. Directional air flow strongly influences the dynamics of microdischarge channels in the DBD and allows studying different properties of the discharges and the possibility of controlling the collective dynamics of MDs.

Acknowledgements

This work was supported by grant AP09258963 from the Science Committee of the Ministry of Education and Science of Kazakhstan

References

1. R. Brandenburg. Dielectric barrier discharges: Progress on plasma sources and on the understanding of regimes and single filaments // Plasma Sources Sci. Technol. Leibniz Institute for Plasma Science and Technology (INP Greifswald), Felix-Hausdorff-Strasse 2, Greifswald, D-17489, Germany: Institute of Physics Publishing. – 2017. – Vol. 26. – № 5. – P.053001.

2. E.A. Usenov et al. The memory effect of microdischarges in the barrier discharge in airflow // Plasma Phys. Reports. – 2020. – Vol. 46. – № 4. – P. 459–464.

3. O. V. Penkov et al. A review of recent applications of atmospheric pressure plasma jets for materials processing // J.Coatings Technol. Res. – 2015. – Vol. 12. – № 2. – P. 225–235.

4. Y.A. Ussenov et al. Dust particle synthesis by the combined plasma source at atmospheric pressure // IEEE Trans. Plasma Sci. Institute of Electrical and Electronics Engineers Inc. – 2019. – Vol. 47. – № 8. – P. 4159–4164.

5. Y. Ussenov et al. Particle formation during deposition of SiOx nanostructured thin films by atmospheric pressure plasma jet // Jpn. J. Appl. Phys. – 2020. –Vol. 59(3). – P. 14-23.

6. T. Jingfeng, W. Liqiu, H. Yuxin, S. Jian, Y. Daren, Z. Chaohai**.** Repetitive **n**anosecond **v**olume **di**scharges under airflows// Plasma Science and Technology. – 2016. – Vol. 18. – P. 273.

7. Fan Z., H Qi., Y. Liu, H. Yan, Ch. Ren**.** Investigation of airflow effects on the dielectric barrier discharge with single/double discharge channel arrangement// Physics of Plasmas. – - 2016. – Vol. 23. – P. 123520.

8. Z. Fan, H. Yan, Y. Wang, Y., H. Liu Guo, Ch. Ren**.** Effect of airflow on the space-time distribution of filaments in dielectric barrier discharge at atmospheric pressure// Physics of Plasmas. – 2018. – Vol. 25. – P. 053517.

9. K. H. Schoenbach, K. Becker**.** Pressure effect on a tandem hollow cathode discharge in argon// Eur. Phys. J. D. – 2016. – Vol. 70. – P. 29.

10. Yu. S. Akishev, M. Yu. Zaitsev, V. A. Kopiev, A. V. Petryakov, N. I. Trushkin. Influence of a barrier discharge on the gas-dynamic parameters of the plasma jet formed by it// Applied Physics. – 2018. – Vol. 6. – P. 14. (In Russian).

11. K. Fujii. Three flow features behind the flow control authority of DBD plasma actuator: Result of high-fidelity simulations and the related experiments// Applied Sciences. – 2018. – Vol. 8. – P. 546

12. S. P. Das, G. Dalei, A. A Barik. Dielectric barrier discharge (DBD) plasma reactor// IOP Conf. Series: Materials Science and Engineering. – 2018. – Vol. -P. 410.

13. A. Ozkan, T. Dufour, T. Silva**.** How do the barrier thickness and dielectric material influence the filamentary mode and CO_2 conversion in a flowing DBD?// Plasma Sources Science & Technology. – 2016. – Vol. 25. – No 2. – P. 11.

14. W. Fan, Z. Sheng, L. Dong, F. Liu, X. Zhong, Y. Cui, F. Hao, T. Du**.** Formation of side discharges in dielectric barrier discharge // Scientific Reports. – 2017. – Vol. 7. – No 8368.

15. **E. H. Matlis, T. C. Corke, B. Neiswander, A. J. Hoffman**. Electromagnetic wave transmittance control using self-organized plasma lattice metamaterial// Journal of Applied Physics. – 2018. – Vol 124. – P. 093104.

16. J. F. Tang, M. Tang, D. S. Zhou, P. T. Kang, X. M. Zhu, C. H. Zhang**.** Effect of airflow on the space-time distribution of filaments in dielectric barrier discharge at atmospheric pressure // Plasma Sci. Technol. – 2019. – Vol 21. -P. 044001.

17. P. Peschke, S. Goekce, P. Leyland, P. Ott**.** Investigation of nanosecond pulse dielectric barrier discharges in still air and in transonic flow by optical methods // J. Phys. D – 2016. – Vol. 49. – 025204.

18. Yu. Akishev, O. Goossens, T. Callebaut, C. Leys**,** A. Napartovich, N. Trushkin**.** The influence of electrode geometry and gas flow on corona-to-glow and glow-to-spark threshold currents in air // J. Phys. D – 2001. – Vol. 34 – P. 8.

19. Y. S. Akishev, G. Aponin, A. Balakirev, M. Grushin, V. Karalnik, A. Petryakov, N. Trushkin**.** Role of the volume and surface breakdown in a formation of microdischarges in a steady-state DBD // Eur. Phys. J. D – 2011 Vol. 61. – P. 421.

20. R. Tschiersch, S. Nemschokmichal, M. Bogaczyk, J. Meichsner**.** Self-stabilized discharge filament in plane-parallel barrier discharge configuration: formation, breakdown mechanism, and memory effects // J. Phys. D – 2017 – Vol. 50 – 415206.

IRSTI 27.35.51 https://doi.org/10.26577/phst.2022.v9.i1.03

Modeling of solar flares like an electrical circuit in plasma focus devices

B.M. Useinov[1], A.M. Zhukeshov[2]*, A.A. Solodovnik[1], N.M. Alimova[1], A.T. Gabdullina[2], Z.M. Moldabekov[2] and A.U. Amrenova[2]

[1]M. Kozybayev North Kazakhstan University, Petropavlovsk, Kazakhstan.
[2]Al-Farabi Kazakh National University, Almaty, Kazakhstan.
*e-mail: zhukeshov@physics.kz

(Received 31 January 2022; received in revised form 24 February; accepted 25 March 2022)

Based on theoretical ideas about different plasma processes in Nature and Space, for example of Solar flares, a conceptual model approach is proposed based on the analogy of the flash flow with processes in an electrical circuit. Quite close in a number of parameters to the flashes are the processes of evolution of plasma objects in the "Plasma focus" setup. Based on the physical similarity of processes of this kind, patterns have been studied that make it possible to trace the change in plasma temperature depending on changes in the operating parameters of the setup. The parameters of the model corresponding to the maximum approximation to the conditions of the flash process are revealed. A program has been developed, calculations and analysis of the dependence of the plasma temperature on the parameters of the setup have been carried out: gas mass, velocity of incoming particles, load resistance in the plasma focus. It is shown that the physical model of a solar flare "Electric Circuit" can be implemented on the basis of an operating plasma focus setup, taking into account the scaling of processes.

Key words: solar flares, plasma focus, discharge current, inductance of the circuit, velocity of incoming particles, temperature, energy release, electrical circuit, pressure.
PACS numbers: 34.80.Bm, 34.80.Dp, 51.50.+v, 52.80.Dy.

1 Introduction

The processes occurring in the Sun's atmosphere attract the interest of science by their influence on a wide range of phenomena in the atmosphere and in the Earth's magnetic field. The main source of such influence is solar flares and associated eruptive prominences and coronal plasma emissions. This led to interest in the development of solar flare models. The latter is especially relevant in connection with the appearance of physical setups which allow to achieve conditions close to those that are characteristic of flash activity. The most promising from this point of view are the data obtained with the help of pulsed plasma accelerators, which are of interest not only in applied terms, but also as model setups for studying processes occurring in space objects. We propose the use of an experimental thermonuclear reactor "plasma focus" to study the nature of solar flares.

2 The theoretical part

For the empirical study of phenomena atypical for terrestrial conditions, it is promising to create physical setups that would model the behavior of an object, both in terms of physical laws and conditions that determine their evolution.

The study is about recreating a number of key circumstances associated with chromospheric solar flares using a controlled thermonuclear reactor (CTR) "Plasma Focus". The criterion for the possibility of implementing this is a comparative analysis of the physical compatibility of the complex parameters of the two objects of study. Four parameters are considered in comparison (table 1): the physical mechanism of the process, the composition of the working substance, the presence of a neutron output, parametric characteristics of the plasma generated during the process [1-3].

Table 1 – The comparison of plasma parameters in the CTR and in the solar flare

The CTR «Plasma Focus»	**The solar flare**
The formation mechanism	
The electric current passes through the insulator between the electrodes, forming a current-plasma sheath when a capacitor bank is discharged. Then it "collapsed" into a dense pinch formation on the contact with the substance	The convergent currents promote the compression of the photospheric plasma, and the shear currents promote the tension. As a result, the free magnetic energy is released, contributing to the flare process – the "expansion" of the plasma.
Parameters	
$I_{max}=10^6$ A, $T=10^6$ K, $v=10^8$cm/s, $n=10^{18}$cm^{-3}	$I_{max}=10^6$ A, $T=10^7$ K, $v=10^7$cm/s, $n=10^{-17}$cm^{-3}
The neutron output	
It is presented	It is presented
The working substance	
the deuterium or the mixture of deuterium-tritium	the hydrogen plasma

The proximity of the parameters of the plasma generated in the first and second cases is noticeable, which suggests the prospect of using the UTR setup to study solar flares. The analogy of the mechanism of formation of a solar flare with an electric circuit requires attention to two circumstances [4]:

- a flash is a non-stationary process, for the description of the energy release of which Ohm's law in its classical expression is not applicable:

$$j = s*E \quad (1)$$

- the main role in the dissipation of electric current energy during a flash belongs to the neutral component of the plasma during the collision of ions with neutrals.

The basis of the physical model of the flash is the coronal magnetic arch. In the nodes of its convective structures, the bases of supergranule cells are located with a size of about R0 ≈ 30 thousand km and a convection velocity of about 0.1-0.3 km/s. The EMF that occurs during convective movements in the photosphere supports an electric current flowing in the arch from one base to another and closing in the chromosphere. At a convection velocity of about 0.1 km / s, the radius of the current tube approaches 103 km, the magnetic field at an altitude of 500 km on the axis of the arch is characterized by an induction of about 2 ×103 Gs, and the current reaches 3 ×1011 A. The inductance of the arch reaches a value of the order of 10 Gn, the current energy in the circuit reaches values of the order of 5×1022 – 5 ×1024 J [5-7]. The latter determines the energy release of the flare associated with the grooved instability of the chromosphere (Fig. 1).

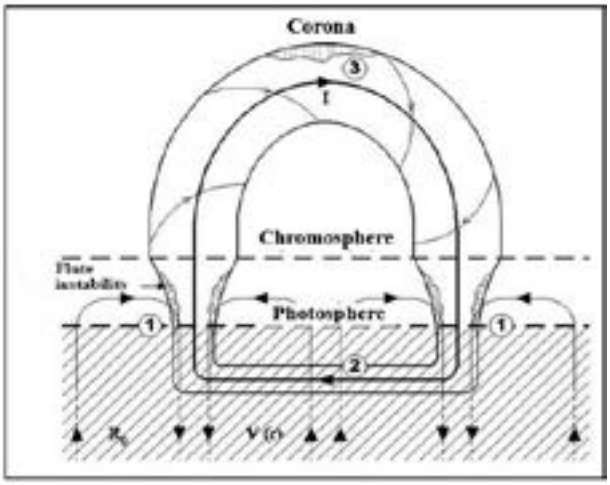

Figure 1 – Structure of the pre-flare coronal arch with current

The formation in question has a resistance R, an inductance L, and a capacity C. Then the current fluctuations in the arch can be described in the language of an RLC circuit with a capacity depending on the magnitude of the electric current according to the law:

$$C(I) = \frac{\pi * a^4 * \rho}{l * I^2} \quad (2)$$

where p is the plasma density, a is the radius of the tube, l is the length of the arch. The oscillation period determined by formula:

$$P = 2 * \pi \sqrt{L * C(I)} \approx 10 l I_{11} C \quad (3)$$

The latter ratio makes it possible to estimate the magnitude of the electric current in the flash by the period of plasma oscillations.

Since the "plasma focus" setup is an electrical circuit, the law of conservation of energy will be written in the form:

$$CU^2/2 = mv^2/2 + 3Rm/2M \quad (4)$$

where m is the mass of the plasma clot, v is its velocity.

In experiments on the UTR setup, the value of 3Rm/2M is close to one. The change in the velocity of particles occurs according to a well – known law:

$$v = v_m \cdot (1 - e^{-\frac{t}{\tau}}) \quad (5)$$

where τ=R*C.

Substituting the value (5) into (4) and expressing T, we obtain a formula for estimating the temperature:

$$T = \frac{C \cdot U^2 - m \cdot v_m^2 \cdot (1 - e^{-\frac{t}{\tau}})^2}{2} \quad (6)$$

3 The experimental part

This makes it possible to trace the change in plasma temperature depending on the change in the setup parameters and determine the parameters that allow achieving the maximum approximation to the physical parameters of the flash plasma.

According to formula (6), calculations of the dependence of the plasma temperature on the mass of the gas, the velocity of the particles and the parameters of the UTR "Plasma focus" were carried out, the results of which are presented in Figures 2 and 3.

An increase in the resistance value of the setup leads to a decrease in temperature by about 1.5 times, which brings its value closer to the real parameters of the surface temperature of the Sun. Then the influence of pressure in the plasma focus on the value of particle velocity is considered. The obtained results are shown in Figure 4.

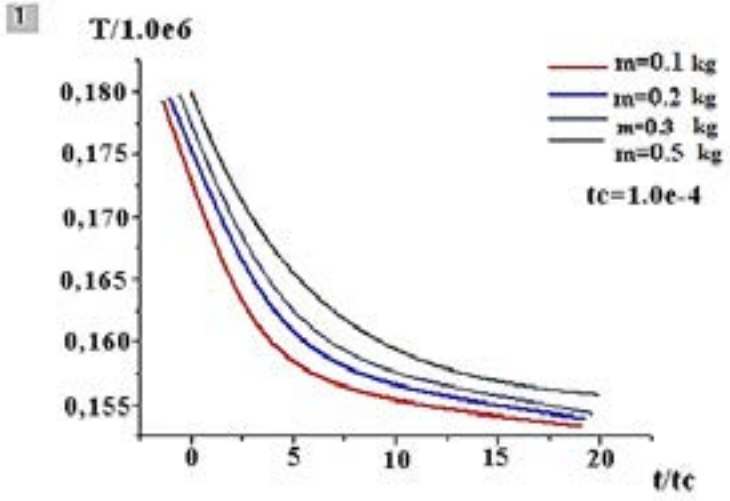

Figure 2 – The dependence of the plasma temperature in the flash model on the mass of the gas. The range of gas mass change corresponds to the setup

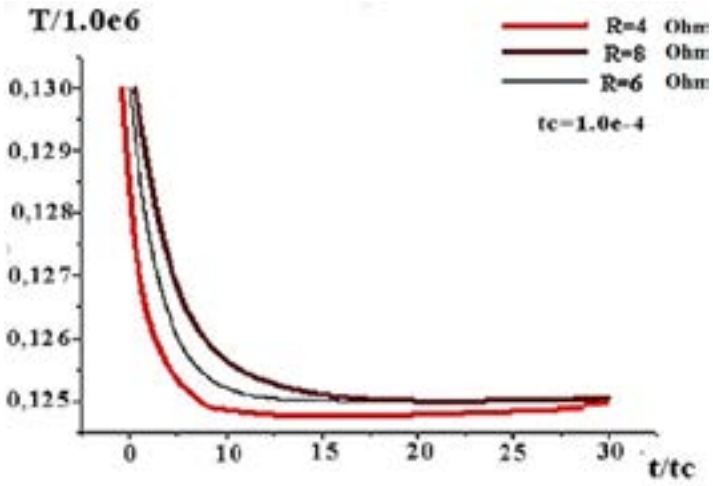

Figure 3 – Temperature dependence on setup's parameters

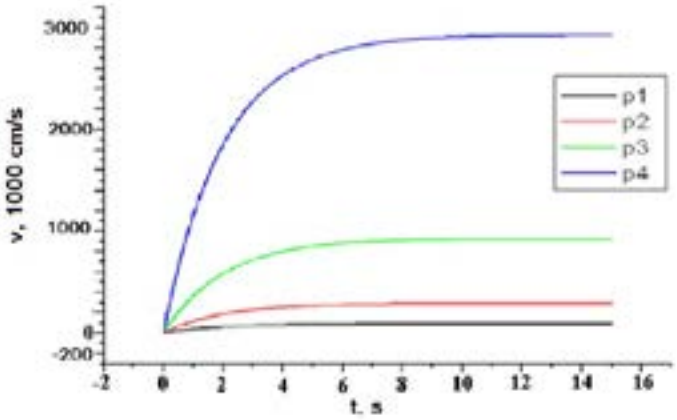

Figure 4 – Dependences of the plasma clot velocity on the pressure

The value of the velocity in all cases increases smoothly, reaching saturation, like plasma particles in a solar flare, where particles due to Joule heat gradually increase the speed and at the moment of the explosive process reach a value that allows them to fly out of the Sun.

On the basis of the obtained data, the dependence of the plasma clot temperature on the velocity of particles interacting with each other was modeled. The results are shown in Figure 5.

As can be seen, the temperature output strongly depends on the velocity of the incoming particles. The optimal value is considered to be the velocity case V_4, corresponding to the minimum pressure in the plasma focus.

Since the plasma focus is similar to an oscillatory circuit, scaling of the real flash and the size of the plasma focus was used to idealize the flash model in the setup. As noted, in order to obtain a flash in the "electric circuit" model, the resistance value must be close to zero, which corresponds to the opening of the circuit and a short circuit, and the inductance of the model must be at least 10 Hn, which is not feasible in real conditions. Taking into account the fact that the aim was to study the physical parameters of the plasma focus for modeling a solar flare, a standard value of the inductance of the plasma focus coil of the order of 10^{-9} Hn was used [8-10]. As a result, the dependence of the current strength on the resistance value of the circuit is shown in Figure 6.

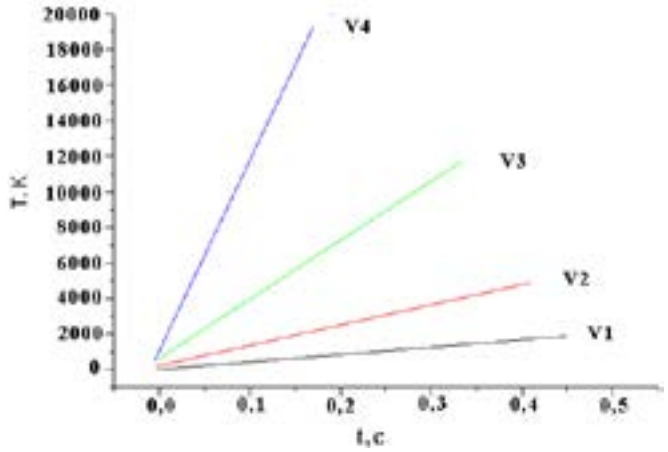

Figure 5 – Dependence of the plasma clot temperature on the velocity of the incoming particles (v1=1000 m/s, v2=2000 m/s, v3= 8000 m/s, v4=28000 m/s)

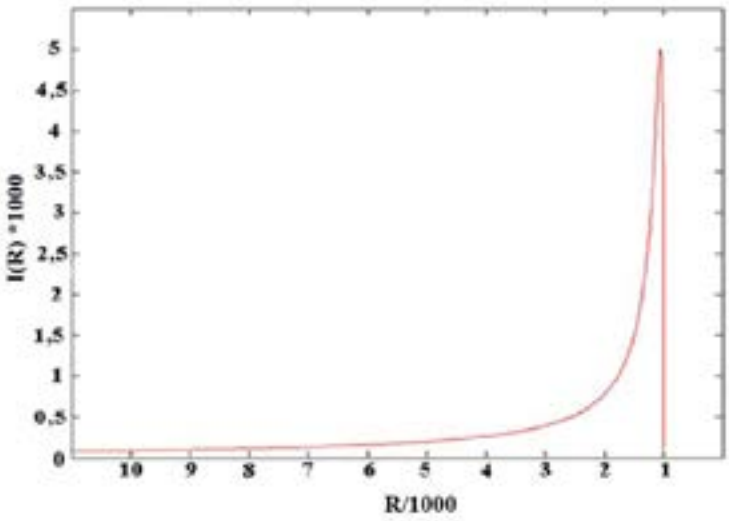

Figure 6 – Dependence of the current strength on the value of the circuit resistance

Here, a change in resistance to zero leads first to a sharp increase in current, and then to a decrease in its value – the opening of the current, this moment corresponds to an explosion in the current layer or a short circuit situation in the circuit. Changing the inductance value in the coils by 3 orders of magnitude leads to a decrease in the maximum current by 2 times and an increase in the resistance in the circuit by an order of magnitude. Figure 6 shows a graphical view of this situation. There is no abrupt termination of the current, but there is a gradual zeroing of its value, which confirms the analogy of the plasma focus with a solar flare, where there is a gradual decline in energy output, with a series of successive weakening flashes. Calculations for the dependencies shown in Figures 5 and 7 were carried out according to the formulas:

$$I = \frac{\mathrm{E}}{\sqrt{(\mathrm{R}*f)^2+(\omega*\mathrm{L}-\frac{1}{\omega*\mathrm{C}})^2}} \quad (8)$$

$$f = \frac{M*V*p}{R*T} \quad (9)$$

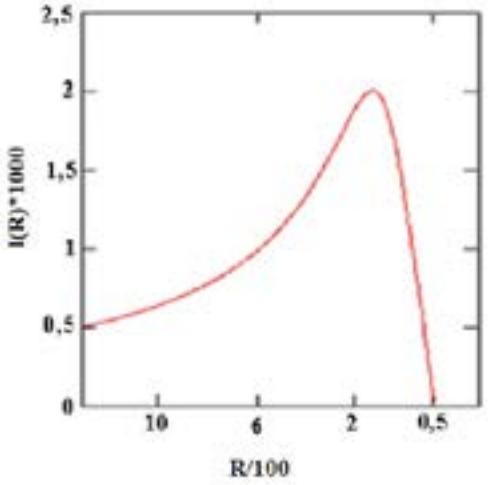

Figure 7 – Dependence of the current strength on the parameters of the circuit

Analysis of the consideration of various situations in the "electric circuit" model, expressed in changes in the parameters of the setups: a change in the resistance in the plasma focus, the amount of working substance and a change in the velocity of the incoming particles, the results are obtained that constitute an idealized model of a solar flare. This conclusion is based on a comparative analysis of data obtained from the RHESSI satellites and processed by specialists of the V. G. Fesenkov Astrophysical Institute and presented in Figure 7 [11-15].

The figure highlights three areas (time intervals are counted by the plasma focus) from 0 to 7 seconds, from 7 to 25 seconds and from 25 seconds to 32 seconds. The best matches of theoretical and real results are observed here. Although values differing in name are compared, however, both the temperature index and the value of the current strength are directly related to the energy output. Since the task of the study was to search for processes similar to natural ones and to prove the possibility of studying solar flares at the Plasma Focus setup, the comparison of these parameters is legitimate.

It should be noted that the average period of processes occurring in the area of a real flash is 65 seconds, and in the Plasma focus is 10 microseconds. From here it is not difficult to get the value of the so-called difference coefficient 65 * 105. Since the size of a standard plasma focus is about 1 meter, multiplying the difference coefficient by the length of the plasma focus, you can get an approximate size of a solar flare of about 6.5 thousand km, which is quite consistent with the length of the average arch 10^{10} cm.

In addition, we compared the results obtained from solar activity from November 2 to 4, 2003, presented in Figure 9, part a, and the theoretical dependence of the current strength on the changing resistance in the plasma focus [16]. The left side of the figure shows the energy spectra for ions of four substances H, He, O, and Fe in the preflare and flare fluxes of the events in 2003. Since in our model the working substance in the plasma focus was deuterium, in that way we compare the curve corresponding to hydrogen. As we can see, that at 8 a.m. on November 2, the value of hydrogen particles (middle part of the graph) per cm^2 fluctuates in the region of 10, at 21.00 p.m. this value changes to 10^0 and the value was 10^{-1}at 3 a.m. on November 4. It indicates a gradual accumulation of energy and the formation of a maximum at a minimum value of the matter's ions per unit area, which can be explained by the "flute instability" of the solar flare model "electric circuit", which we have discussed it above.

At the same time, by idealizing the processes occurring in the plasma focus, results were obtained that are close to real data in that a change in the amount of the working substance makes it possible to obtain a maximum (short circuit) of the current strength [17-19].

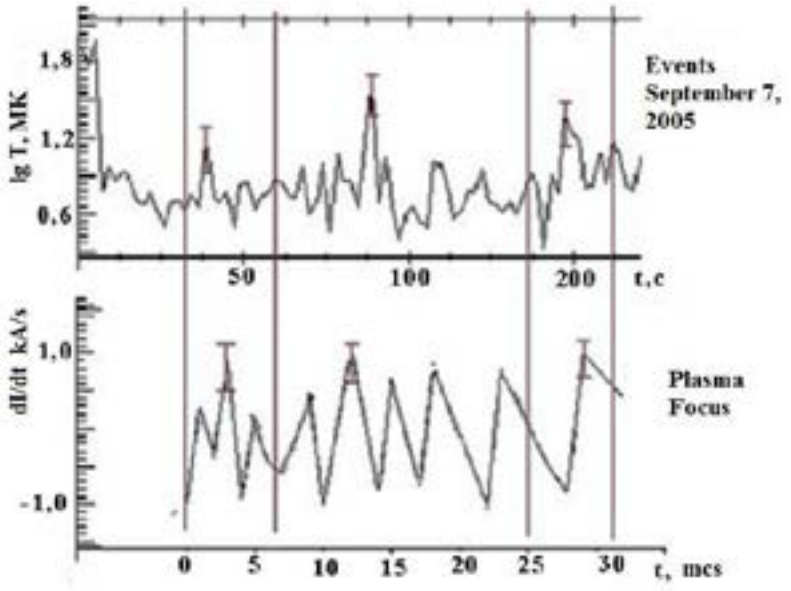

Figure 8 – The logarithmic dependence of the solar flare's temperature on September 7, 2005 and the oscillogramme of the derivative of the plasma focus current

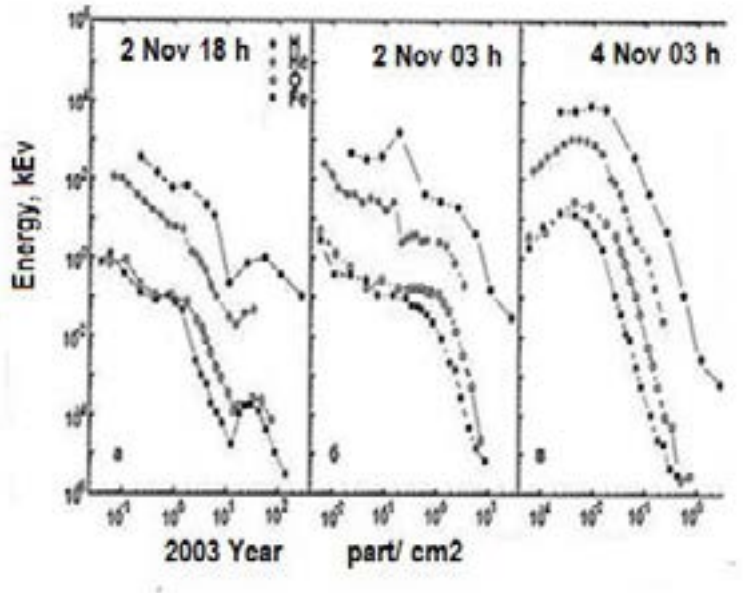

Figure 9 – The energy spectra of substances in flare flows on November 2-4, 2003 and the dependence of the current strength on the parameters of the oscillatory circuit

The estimation of the proximity of the presented processes is obtained as a result of the conversion of the maximum current value into the electronic temperature, according to the formula

$$T = \frac{I^2}{2\pi c^2 a_1^2 k n_e} \qquad (10)$$

we obtain the value of temperature about 10^6 K, while the energy value can be rounded off such as $1eV \approx 10^4$ K. Then the final value will correspond to an energy of 0.1 keV, the difference coefficient is 10^4, such discrepancy can be explained by the scaling of processes, but there is tracedvisually the similar morphology of accumulation processes and the energy release in both processes.

4 Conclusions

In that way, we can conclude that the physically conceptual model of the solar flare “electric circuit” has found its implementation on the basis of the PF, taking into account the scaling of the flare process to the real PF setup. As a result of the simulation, the data were obtained that do not contradict the real ones and have a relative coincidence with the non-stationary processes, the processes of the formation of an energy surge.

Acknowledgements

This research has been funded by the Science Committee of the Ministry of Education and Science of the Republic of Kazakhstan (Grant No. AP15473243).

References

1. E.C. Hagen, D. Lowe, R. Obrien at al. PPPS-2013: Fast framing camera images of neutron production cessation at high currents in a Dense Plasma Focus machine// IEEE PPPS 2013 Conf., San Francisco, California, USA. -2013. -P. 7BB1. https://doi.org/10.1109/PLASMA.2013.6634885

2. A. M. Zhukeshov, A.U. Amrenova, A.T. Gabdullina et al. A plasma formation in pulsed coaxial gun at continuously filling regime // American Journal of Physics and Applications. – 2013. – Vol. 1, No. 1. – P. 5-9. https://doi.org/10.11648/j.ajpa.20130101.12

3. E. J. Lerner, M. Syed et al. Confined ion energy >200 keV and increased fusion yield in a DPF with monolithictungsten electrodes and pre-ionization // Physics of Plasmas. – 2017. – Vol. 24. – P. 102708. https://doi.org/10.1063/1.4989859

4. A.M. Zhukeshov, B.M. Useinov, A.T. Gabdullina, et al. Investigation of diffusion processes at metal target irradiation by pulsed plasma flow // Proc. of 21st International Symposium on Heavy Ion Inertial. July 18-22, 2016, Astana, Kazakhstan.

5. A. Zhukeshov, A. Amrenova, A. Gabdullina, et al. Pulsed plasma accelerator for steel samples surface modification // Thes. of 43 Int. Conf. IEEE ICOPS/ june 19-23, 2016, Banff, Canada. -P.1.

6. S. N. Polukhin, A. M. Dzhamankulov, A. E. Gurey et al. Measurement by the laser-optical method of the velocity of plasma jets generated in a kilojoule plasma focus for various gases // Plasma Physics, -2016. -Vol. 42. -No. 12. -P. 54–60 (in Russian).

7. A.N. Mayorov, V.Ya. Nikulin, A.V. Oginov et al. Investigation of axial plasma flows in a PF-4 plasma focus facility // P.N. Lebedev Institute of the Russian Academy of Sciences. –2015. – No. 7. – P. 3-13. (in Russian).

8. A.M. Zhukeshov, B.M. Ibraev, Sh.G. Giniyatova, et al. Development of the discharge chamber of the experimental setup "Plasma Focus" // Bulletin of ENU, 2016, No. 2, pp. 386 – 389. in Russian).

9. V.V. Vikhrev, S.V. Suslin. Jet formation in the plasma focus // Proceedings XLII Int. Zvenigorod Conference on Plasma Physics and Controlled Thermonuclear Fusion, 2015, p. 180. (in Russian)

10. B.B. Mikhalyaev, M.S. Ruderman, E. Naga Varun. Fast sausage solitons and super nonlinearity in coronal loops // Geomagnetism and Aeronomy. -2016. -Vol. 56. -№ 8. -P. 1040. https://doi.org/10.1134/S0016793218070149

11. Myachin D. Yu. "Structure and development of non-spotted solar flares": dissertation of Can. Phys.-Math. Sciences. Irkutsk, 2015. 214 p. (in Russian)

12. V. Abramov-Maximov, V. Borovik, L. Opeikina, A. Tlatov. Peculiarities of the development of active regions on the Sun prior to strong X-class flares: Joint analysis of data from the RATAN-600 radio telescope and SDO space observatory // Solar. Phys., -2015. -Vol. 290. -P. 53. https://doi.org/10.1134/S0010952514010018

13. A.A. Soloviev et al. Proceedings of Conf. SSZF-2017 (this collection), GOI RAS, 2017. (in Russian)

14. N. Mittal et al., On the statistical characteristics of radio-loud and radio-quiet halo coronal mass ejections and their associated flares during solar cycles 23 and 24 // New Astronomy. – 2016. – Vol. 47. – P. 64-80. https://doi.org/10.1016/j.newast.2016.02.004

15. V. Abramov-Maximov, V. Borovik, L. Opeikina, et al. Dynamics of microwave sources associated with the neutral line and the magnetic-field parameters of sunspots as a factor in predicting large flares // Solar Physics. -2015. -Vol. 290. -P. 53–77. https://doi.org/10.1007/s11207-014-0605-8

16. V.M. Bogod, L.V. Yasnov. Determination of the structure of the coronal magnetic field using microwave polarization measurements // Solar Phys., -2016. -Vol. 291. -P. 3317–3328. https://doi.org/10.1007/s11207-016-0936-8

17. L. Soto et al. Characterization of the axial plasma shock in a table top plasma focus after the pinch and its possible application to testing materials for fusion reactors // Physics of Plasmas. – 2014. – Vol. 21. – P. 122703. https://doi.org/10.1063/1.4903471

18. P.V. Strekalova, Y.A. Nagovitsyn, A. Riehokainen, et al. Long-period variations in the magnetic field of small-scale solar structures // Geomagnetism and Aeronomy. – 2016. – Vol. 56. – P.1052–1059. https://doi.org/10.1134/S0016793216080211

19. A.G. Tlatov, N.N. Skorbehz, V.N. Ershov. Numerical processing of sunspot images using the digitised long-term archive of the RGO observatory // AIP Conference Series. – 2016. – Vol. 504. – P. 237.

Funded by Al-Farabi KazNU

IRSTI 29.19.31 https://doi.org/10.26577/phst.2022.v9.i1.04

Determination of the resistance of external parameters to the degradation of the parameters of silicon photocells with input nickel atoms

N.F. Zikrillayev, E.B. Saitov, K.S. Ayupov and I.A. Yuldoshev

Tashkent State Technical University, Tashkent, 100095, Republic of Uzbekistan
e-mail: elyor.saitov@yandex.ru

(Received 17 March 2022; received in revised form 5 April; accepted 29 April 2022)

Currently, there is a growing need for high-performance photocells with increased stability of parameters to external influences, such as thermal and radiation resistance. This work is devoted to the study of photocells available in the volume of an ordered micro- and nanostructure based on silicon doped with impurity nickel atoms. The study of the formation of micro- and nanoclusters of impurity atoms in silicon photocells that were subjected to additional high-temperature processing makes it possible to determine the degradation of nickel clusters, which strongly affect the electrical parameters of photocells. It is shown that impurity nickel atoms will increase the stability of the electrophysical parameters of photocells under the influence of both high temperature and radiation. The results obtained in the study showed that the introduction of nickel impurity atoms into the volume of silicon-based photocells leads to temperature and radiation resistance, and also increases efficiency.

Key words: cluster, nickel, degradation, diffusion, photocell, self-organization, semiconductor, doping, supersaturation factor, solubility, low-temperature annealing.
PACS numbers: 73.43.Fj, 73.50.Pz.

1 Introduction

One of the new and promising methods for creating nanosized structures in the crystal lattice of a semiconductor is the formation of nanoclusters of impurity atoms with the participation of uncontrolled defects in the crystal lattice, since this method of creating nanosized structures, in contrast to the existing methods of molecular beam epitaxy, which require complex expensive equipment, has the following advantages [1, 2]:

– allows one to create nanoscale structures evenly distributed throughout the volume of the crystal;

– makes it easy to control the structure, composition, distribution of nanoscale structures and their ordering;

– this method can be used to obtain a material with stable electrophysical parameters and external influences, such as temperature and radiation [1, 3];

– allows you to control the charge state of nanoclusters in a wide range (N+(-)n, where n>3), that is, to create multiply charged centers in a semiconductor, which are the basis for a very promising material for nanophotonics [4-7].

This paper presents original experimental results on the study of the electrical and photoelectric properties of photovoltaic cells based on silicon with nanoclusters of impurity nickel atoms. Investigation of the influence of high-temperature processing and the influence of radiation γ – irradiation on the electrophysical parameters of the obtained photocells. It is shown that such a study significantly increases the possibility of large-scale use of photocells based on silicon doped with impurity nickel atoms under extreme conditions and also increases the efficiency of their operation.

Therefore, the main goal of this work is to show that under certain conditions of doping with impurity nickel atoms, nanoclusters are formed and to show the possibility of controlling the size and distribution of clusters in silicon.

2 Technology for obtaining materials and research method

Recently, specialists in the field of nanotechnology and nanoelectronics have paid great attention to the technology of obtaining self-organizing impurity clusters with controlled structures [8–11]. In this regard, some interesting results on the implantation of Co and Ge ions in Si, as well as on the ion implantation of other atoms in semiconductor materials, should be noted [12–17]. As far as we know, technologies for obtaining self-organizing clusters of impurity atoms using diffusion technologies have not been sufficiently studied at present. And the diffusion technology for obtaining nanosized structures is not only a more accessible and cheap method that allows large-scale production, but also makes it possible to create nanosized structures of various types and a given distribution and density over the volume of the crystal.

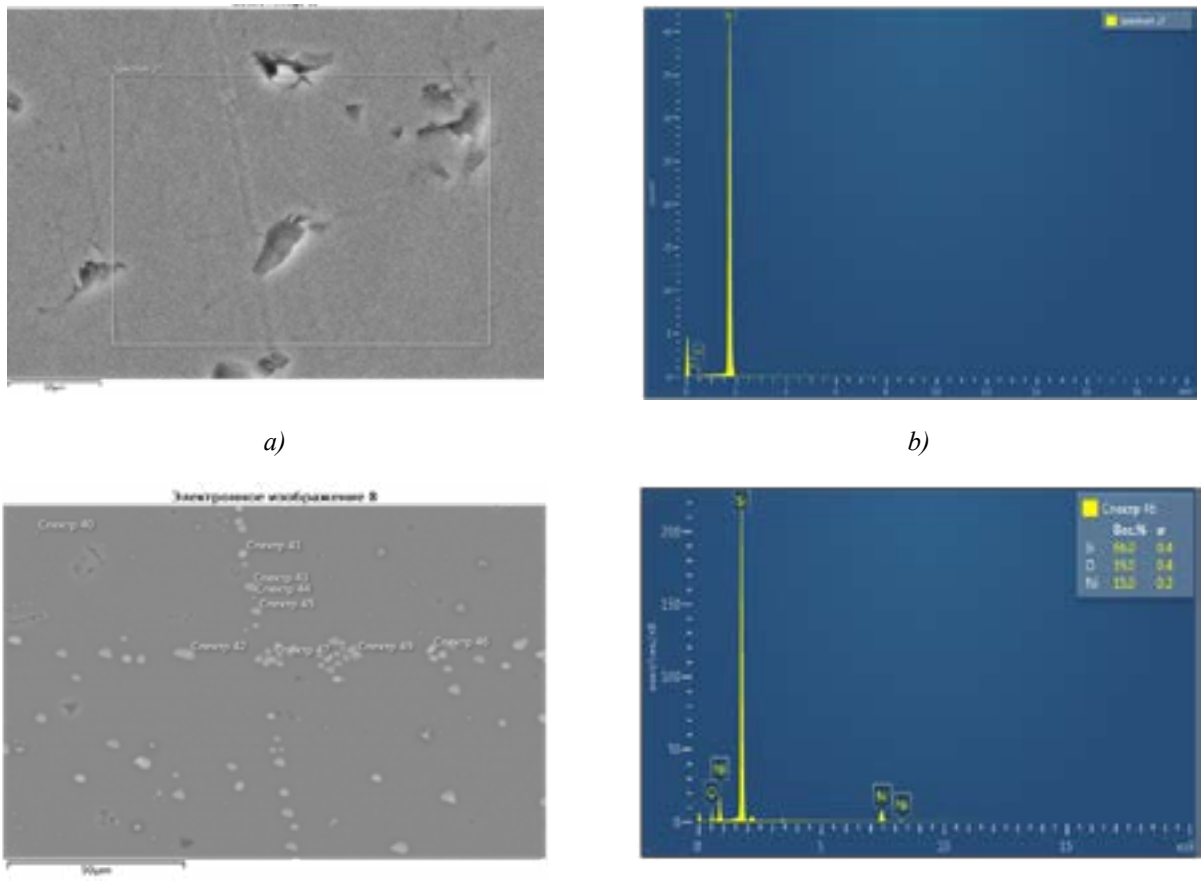

a) *b)*

c) d)

Figure 1 – Pictures of the surfaces of photovoltaic cells with nickel clusters (REM):
a) – Control sample surface without clusters; b) – spectrum without cluster zones;
c) – with cluster zones at Ni = 9.5%; d) – with cluster zones at Ni = 15%

Using an EVOMA-10 electron microscope, the surface of polished photocells was examined at a certain temperature. Figure 6 shows a structural analysis of photocell plates with impurity nickel atoms, which were obtained using an electron microscope of the brand Oxford Instruments ZEISS EVOMA-10.

The obtained results prove that in photocells there are clusters of impurity nickel atoms in the range of 9–15%, while the experimental error was within the error of σ=0.1–0.2%.

3 Experimental results and their discussion

The stability of the electrophysical parameters of the obtained photocells, when operating under experimental conditions such as elevated temperatures and

relatively high radiation intensities, leading to the formation of various defects, which lead to a strong change in the parameters of the base material. This is due to the fact that during high-temperature operations, the concentration and size of clusters that form impurity nickel atoms change. To elucidate the nature of the change in the electrophysical parameters of photocells based on silicon doped with impurity nickel atoms into silicon, studies were carried out on the effect of additional thermal annealing on the open circuit voltage and short circuit current of control photocells [18–20].

The study of the effect of additional high-temperature annealing after the formation of a p-n junction led to a decrease in the initial parameters of photocells. The short-circuit current and open-circuit voltage of photocells depended quite strongly on the characteristics of the initial structures of photocells (the depth of the p-n junction, the doping concentration of the frontal and base regions). It was found that the higher the temperature and time of additional high-temperature annealing, the stronger the decrease in the initial $U_{o.c.v.}$ and $I_{sh.c.c.}$, and the degradation is more pronounced in the case of a shallow (less than 1 μm) p-n junction. For a photocell with a deep p-n junction, the change in the initial parameters was less pronounced [21-24]. Tables 1 and 2 show data on the change in the open circuit voltage and short circuit current of the control photocell depending on the temperature of thermal annealing at an annealing time of 1 hour. Table 1 shows the data for the starting material SEC-0.5.

Table 1 – Changes in the open-circuit voltage and short-circuit current of control photocells based on SEC-0.5 depending on the temperature of thermal annealing at an annealing time of 1 hour

Depth p-n, microns	Options	Annealing temperature, °C.				
		Initial	900	1000	1100	1200
0,5	U_{xx}, mV	527	491	439	402	374
	$J_{кз}$, mA	16,8	14,2	12,8	11,6	10,7
1	U_{xx}, mV	595	572	546	514	497
	$J_{кз}$, mA	20,5	18,5	17,5	16,6	15,8
3	U_{xx}, mV	588	568	552	534	514
	$J_{кз}$, mA	17,3	15,6	14,8	14,1	13,5

The study of the effect of additional heat treatment on the parameters of photocells with clusters of impurity nickel atoms at T = 600 and 650 °C for 3 hours showed that no practical changes were observed in the electrophysical parameters of photocells. In the control samples after heating at T = 600 °C, a decrease in the short-circuit current by 3-6% of the initial value was observed [25-27]. During heat treatment of photocells doped with nickel atoms, a decrease in the initial values of $I_{sh.c.c.}$ was observed. and $U_{o.c.v}$. After heat treatment, an increase in $I_{sh.c.c}$ and $U_{o.c.v}$ was observed in some photocells. This connection was more pronounced in photocells having a low dopant concentration with the formation of low energy levels. For example, on heat-treated photocells, impurities in the original silicon (boron or phosphorus), which form small energy levels, go into the compensation position [28-31]. As a result of interaction with impurities that form deep energy levels, the values of $U_{o.c.v.}$ and $I_{sh.c.c}$. photocells drop to zero.

After the formation of the p–n junction, a decrease in the parameters of additionally heat-treated photocells was observed. If the heat treatment time was longer, then this sharply reduced the initial values of $U_{o.c.v.}$ and $I_{sh.c.c}$.

Tables 2 and 3 provide information on the change in open circuit voltage and short circuit current depending on heat treatment for 1 hour. Table 2 shows the data on the initial starting material PhES -4.5. Table 3 shows the electrophysical parameters of photocells made of PhES-40 silicon. Additional heat treatment time 1 hour.

Table 4 shows the electrophysical parameters of photocells made on SEC-10 grade silicon. Additional heat treatment time 1 hour.

Table 5 shows the electrophysical parameters of photocells made on the basis of SEC-0.5 silicon and subjected to additional heat treatment t=1 hour.

Table 2 – Data obtained for photocells based on PhES-4.5 silicon

Additional heat treatment temperature, °C	Average cluster sizes, microns	$U_{o.c.v}$, mV	$I_{sh.c.c.}$, mA/cm^2
1200	1-2	514	13,5
1100	1,5-2	534	14,1
1000	2,5-3	552	14,8
900	1,5-2	568	15,6
Control sample	-	588	17,3

Table 3 – Electrophysical parameters of photocells made on the basis of silicon grade PhES-40

Additional heat treatment temperature, °C	Average cluster sizes, microns	$U_{o.c.v}$, mV	$I_{sh.c.c.}$, mA/cm^2
1200	1 – 2	374	10,7
1100	2 – 5	402	11,6
1000	2 – 7	439	12,8
900	2 – 8	491	14,2
Control sample	-	527	16,8

Table 4 – Electrophysical parameters of photocells made on the basis of SEC -10 silicon

Additional heat treatment temperature, °C	Average cluster sizes, microns	$U_{o.c.v}$, mV	$I_{sh.c.c}$, mA/cm^2
1200	1 – 2	497	15,8
1100	2 – 5	514	16,6
1000	2 – 5	546	17,5
900	2 – 20	572	18,5
Control sample	-	595	20,5

Table 5 – Electrophysical parameters of photocells made on the basis of silicon grade SEC -0.5

Additional heat treatment temperature, °C	Average cluster sizes, microns	$U_{o.c.v}$, mV	$I_{sh.c.c}$, mA/cm^2
1100	0,5 – 1	480	20,9
1000	1 – 1,5	482	21,4
900	1,5 – 2,5	498	45,7
800	2,5 – 3	506	28,1
Control sample	0,5 – 1	507	20,5

The study of the effect of γ-radiation was carried out in the range of irradiation doses from 10^5 to 10^9 R/sec on the electrical parameters of photocells based on silicon with clusters of nickel atoms. Figures 2 and 3 show the results of studying the dependences of the short-circuit current and open-circuit voltage on the dose of γ-radiation.

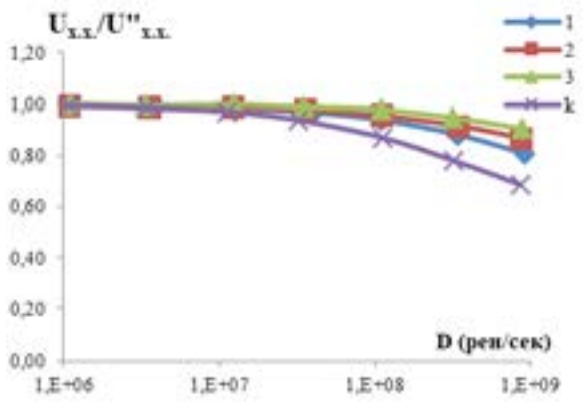

1, 2, 3 – concentration of nickel atoms respectively Ni 10^{15} cm^{-3}, 10^{16} cm^{-3}, 6×10^{16} cm^{-3}, j – control photocell.

Figure 2 – Change in open circuit voltage of photocells

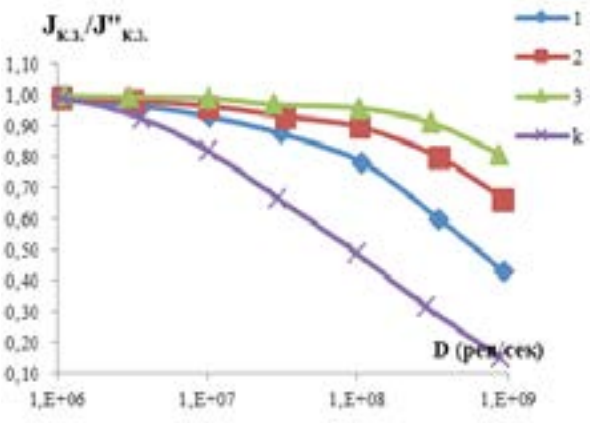

1, 2, 3 – concentration of nickel atoms respectively Ni 10^{15} cm^{-3}, 10^{16} cm^{-3}, 6×10^{16} cm^{-3}, j – control photocell.

Figure 3 – Change in the short circuit current of photocells

The dependence of the open-circuit voltage of photocells on the dose of γ-radiation is shown in Figure 2. Here the concentration of nickel impurity atoms was respectively equal to: 1 – 1×10^{15} cm^{-3}, 2 – 1×10^{15} cm^{-3}; 3 – 6×10^{16} cm^{-3}, j – for the control sample with no impurity of nickel. Such dependences were obtained in the study of changes in the short circuit current on the dose of γ radiation (Fig. 3).

After irradiation of photocells additionally doped with nickel atoms with an optimal concentration of γ-radiation with a dose of 10^9 R, the open circuit voltage drops by 8–10% relative to non-irradiated samples. In the same samples, the short-circuit current decreased by 15–18%. Under the same conditions, the degradation of the parameters of the control photocells subjected to irradiation amounted to 25–30% in voltage and 70–80% in current. When irradiated with gamma rays with a dose of up to 10^9 R, the electrophysical parameters of photocells with introduced nickel atoms did not exceed 5 and 10%, respectively.

When irradiated with a dose of up to 10^7 R, the change in the values of the open-circuit voltage and short-circuit current was no higher than 1–2%.

4 Conclusions

The uniqueness of silicon-based solar cells with nanoclusters of nickel atoms lies in the fact that the electrophysical parameters are thermally stable and radiation resistant, which play an important role in solar node operation. Based on the results of the data obtained, the following important conclusion can be drawn – the radiation stability of photocells additionally alloyed with nickel atoms improves the open-circuit voltage and short-circuit current by two to four times relative to the parameters of control photocells made without impurity nickel atoms. This shows that the introduction of impurity nickel atoms into silicon leads to thermal stability and radiation resistance, which lead to an increase in the efficiency of photocells.

Silicon-based solar cells with nanoclusters of nickel atoms have unique functionality in the field of modern photovoltaics.

The work was financially supported by the Ministry of Innovative Development of the Republic of Uzbekistan within the framework of the project F-OT-2021-497 – “Development of the scientific foundations for the creation of solar cogeneration plants based on photovoltaic thermal batteries”.

References

1. B.A. Abdurakhmanov, M.K. Bakhadirkhanov, K.S. Ayupov, H.M. Iliyev, E.B. Saitov, A. Mavlyanov, H.U. Kamalov. Formation of clusters of impurity atoms of nickel in silicon and controlling their parameters // Nanoscience and Nanotechnology. -2014. -Vol. 4. -No. 2. -P. 23-26.

2. E. Saitov. Study of quantitative and qualitative characteristics of nickel clusters and semiconductor structures // Journal of Materials Science and Chemical Engineering. -2016. -No.4. -P. 30-35.

3. M.K. Bakhadyrkhanov, A.Sh. Mavlyanov, U.Kh. Sodikov, M.K. Khakkulov. Silicon with binary unit cells as a novel class of materials for future photoener- getics // Applied Solar Energy. -2015. -Vol. 51. -No. 4. -P. 258–261.

4. B.A. Abdurakhmanov, M.K. Bakhadirkhanov, H.M. Iliyev, S.B. Isamov, E.B. Saitov, A. Mavlyanov, H.U. Kamalov, Z. Saparniyazova, O. Sattarov, U.Kh. Sodikov, N.F. Zikrillayev. Silicon with clusters of impurity atoms as a novel material for photovoltaics // Nanoscience and Nanotechnology. -2014. -Vol.4(3). -P. 41-43.

5. M.K. Bakhadyrhanov., U.X. Sodikov., D. Melibayev., T. Wumaier., S.V. Koveshnikov., K.A. Khodjanepesov., J. Zhan. Silicon with clusters of impurity atoms as a novel material for optoelectronics and photovoltaic energetics // Journal of Materials Science and Chemical Engineering. -2018. -Vol. 6. -P.180–190.

6. J. Toshov, E. Saitov. Portable autonomous solar power plant for individual use// E3S Web of Conferenccs RSES 139. -2019. -Vol. 01087. -P. 1-4, 2019.

7. N.F. Zikrillaev., S.A. Tachilin. E.B. Saitov. Efficient inverters for alternative energy sources // International scientific-practical conference “Problems of modern engineering” Andijan May 16-17, 2013. -P. 1.

8. N. Zikrillayev, E. Saitov, B. Botirov, B. Nasirdinov, Yu. Kurbanov, F. Turayev, N. Shodiyeva. Study of the results of diffusion doping technique for producing heterostructures (Si-Ge) using microprobe analysis // Austrian Journal of Technical and Natural Sciences. -2019. -No.1-2. -P.56-61.

9. E.B. Saitov. Technology of manufacturing solar cells with clusters of Ni atoms // Asian Journal of Multidimensional Research (AJMR). -2019. -Vol.8. -No.3. -P. 494-499.

10. Yu. M Kurbonov, E.B Saitov, B. M. Botirov. Analysis of the influence of temperature on the operating mode of a photovoltaic solar station. ICECAE 2020, IOP Conf. Series: Earth and Environmental Science 614 (2020) 012034. DOI: 10.1088/1755-1315/614/1/012034

11. Saitov E.B. Optimal model for additional operation of the storage system for photovoltaic wind power plants // E3S Web of Conferences, Sustainable Energy Systems: Innovative Perspectives, SES 2020; Saint-Petersburg; Russian Federation; 29 October 2020. -2020. -Vol. 220. -P. 01080. https://doi.org/10.1051/e3sconf/202022001080

12. E.B. Saitov, Y.B. Sobirov, I.A. Yuldoshev, I.R. Jurayev, S. Kodirov. Study of solar radiation and wind characteristics in various regions of Uzbekistan // E3S Web of Conferences, Sustainable Energy Systems: Innovative Perspectives, SES 2020; Saint-Petersburg; Russian Federation; 29 October 2020. -2020. -Vol. 220. -P. 01061. https://doi.org/10.1051/e3sconf/202022001061

13. E.B. Saitov. Renewable energy development in Uzbekistan: Current status, problems and solutions // E3S Web Conf. Rudenko International Conference “Methodological problems in reliability study of large energy systems” (RSES 2020). -2020. -Vol. 216. -P. 01134. https://doi.org/10.1051/e3sconf/202021601134

14. S. Shoguchkarov, I. Yuldoshev, E. Saitov, A. Boliev. The effect of the surface geometry of a photovoltaic battery on its efficiency // E3S Web Conf. Rudenko International Conference “Methodological problems in reliability study of large energy systems” (RSES 2020). -2020. -Vol. 216. -P. 01149. https://doi.org/10.1051/e3sconf/202021601149

15. E.B. Saitov., J.B. Toshov., A.O. Pulatov., B.M. Botirov., Yu.M. Kurbanov. Networked interactive solar panels over the roof photovoltaic system (PVS) and its cost analysis at Tashkent state technical University E3S Web Conf. Rudenko International Conference “Methodological problems in reliability study of large energy systems” (RSES 2020). -2020. -Vol. 216. -P. 01133. https://doi.org/10.1051/e3sconf/202021601133

16. I. Sapaev, E. Saitov, N. Zoxidov, B. Kamanov. Matlab-model of a solar photovoltaic station integrated with a local electrical network // IOP Conference Series: Materials Science and Engineering, -2020. -Vol. 883. -No. 1. -P. 012116. https://doi.org/10.1088/1757-899x/883/1/012116

17. J. Toshov., E. Saitov. Portable autonomous solar power plant for individual use // E3S Web of Conferences. -2019. -Vol. 139. -P. 01087. https://doi.org/10.1088/1757-899X/883/1/012116

18. M.K. Bakhadyrkhanov, S.A. Valiev, N.F. Zikrillaev, E.B. Saitov, S.A. Tachilin. Silicon photovoltaic cells with clusters of nickel atoms // Applied Solar Energy (English translation of Geliotekhnika). -2016. Vol. 52(4).-P. 278–281. https://doi.org/10.3103/S0003701X1604006X

19. N. Zikrillayev, E. Saitov. Silicon materials -the future of photovoltaics. Monograph. Lab Lambert Academic Publishing. Chisinau, Republic of Moldova. ISBN: 987-620-0-50311-4. 2019, 96 p.

20. N.F. Zikrillaev, E.B. Saitov, O.B. Tursunov A.J. Khusanov, K.K. Kurbonaliev. Features of self-oscillatory processes in a strongly compensated silicon with nanoclusters of impurity atoms // European Journal of Molecular & Clinical Medicine. -2021. -Vol. 8. -Iss. 1. -P.935-939.

21. E.B. Saitov, N.F. Zikrillayev. Photovoltaic effect in silicon with Schottky micro-barriers created on the basis of nickel impurity atoms and spectral characteristic // European Journal of Molecular & Clinical Medicine. -2021. -Vol. 8. -Iss. 1. -P. 982-992.

22. Y.S. Ergashov, B.E. Umirzakov. Structure and properties of a bilayer nanodimensional $CoSi_2$/Si/$CoSi_2$/Si system obtained by ion implantation //Technical Physics. -2018. -Vol. 63(12). -P. 1820-1823.

23. Y.S. Ergashov. Composition and properties of nanoscale Si structures formed on the CoSi2/Si(111) surface by Ar+ ion bombardment // Technical Physics. -2017. -Vol. 62(5). -P. 777-780.

24. Y.S. Ergashov, D.A. Tashmukhamedova, F.G. Djurabekova, B.E. Umirzakov. Effect of surface microroughness on the composition and electronic properties of CdTe/Mo(111) films Bulletin of the Russian Academy of Sciences: Physics. -2016. -Vol. 80(2). -P. 138-140.

25. B.E. Umirzakov, D.A. Tashmukhamedova, M.A. Tursunov, Y.S. Ergashov, G.K. Allayarova. Escape depth of secondary and photoelectrons from CdTe films with a Ba film // Technical Physics. -2019. -Vol. 64(7). -P. 1051-1054.

26. E.S. Ergashov, Z.A. Isakhanov, B.E. Umirzakov. Transmission of electromagnetic waves through thin Cu films // Technical Physics. -2016. -Vol. 61(6). -P. 953-955.

27. Y. Ergashov, B. Donaev, S. Khudainazarov, J. Normuminov. Formation of photoelectron spectra of alloys niobium-molybdenum-zirconium. E3S Web of Conferences. -2021. -Vol. 264. -P. 05036.

28. E. Yokub, U. Boltakhodja. Electron spectroscopy of CdMeTe nanostructures created on CdTe surface under ion bombardment // E3S Web of Conferences. -2020. -Vol. 178. -P.01079.

29. Z.E. Mukhtarov, Z.A. Isakhanov, B.E. Umirzakov, T. Kodirov, E.S. Ergashev. Effect of implantation of active metal ions on the elemental and chemical compositions of the CdTe surface // Technical Physics. -2015. -Vol. 60 (12). -P. 1880-1883.

30. Y.S. Ergashov, D.A. Tashmukhamedova, B.E. Umirzakov. On the synthesis of nanoscale phases of metal silicides in the near-surface region of silicon and the study of their electronic structures by passing light // Journal of Surface Investigation. -2017. -Vol.11 (2). -P. 480-484.

31. Y.S. Ergashov, D.A. Tashmukhamedova, E. Rabbimov. Energy spectra of SiO_2 nanofilms formed on a silicon surface by ion implantation // Journal of Surface Investigation. -2015. -Vol.9 (2). -P. 350-354.

Funded by Al-Farabi KazNU

IRSTI 29.19.16 https://doi.org/10.26577/phst.2022.v9.i1.05

The effect of deposition technique on formation of transparent conductive coatings of SnO_2

E. A. Dmitrieva[1], I. A. Lebedev[1], E. A. Grushevskaya[1], D. O. Murzalinov[1], A. I. Fedosimova[1], A. E. Kemelbekova[1*], Zh.Sh. Kazhiev[1], Zh.K. Zhaysanbayev[2] and A. T. Temiraliyev[1]

[1]Satbayev University, Institute of Physics and Technology, Almaty, Kazakhstan
[2]Border Academy of National Security Committee of the Republic of Kazakhstan, Almaty, Kazakhstan
*e-mail: a.kemelbekova@mail.ru
(Received 17 March 2022; received in revised form 20 April; accepted 10 May 2022)

The producing technology of transparent conductive layers is the basis for many optoelectronic devices. To increase transparency and conductivity at low-cost and controlled methods is an important challenge. Studied samples of SnO_2 coatings were obtained by sol-gel method. The deposition of films on glass substrates was carried out by dip coating, spin-coating and sprays-pyrolysis methods. According to micro-weighing, the film thickness varies from 250 nm to 290 nm. The layer with the most uniform thickness was achieved using spray pyrolysis. Films deposited by this technique exhibit the greatest transparency and lowe*st* resistance. It is important to note that these samples have the minimum scatter of resistance values depending on the surface area. In case dip coating technique the resultant film contains open- and closed-type blisters. This confirms the fact of inhomogeneous surface morphology of these films. X-ray diffraction analysis showed that films obtained by spin-coating and dipping methods contain SnO_2 crystallites, the size of which does not exceed 10.3 nm; while films obtained by spay pyrolysis are amorphous. This is because the formation of the structure in the spay pyrolysis proceeds faster due to the substrate heating.

Key words: thin films, SnO_2, sol-gel method, spray pyrolysis, spin-coating, dip coating, transparency, structure, resistance.
PACS numbers: 61.43.Dq, 39.30.+w.

1 Introduction

Films based on tin dioxide have a wide range of applications. For example, they are used as a sensitive element in gas analyzers. A transmittance of more than 80% over a wide wavelength range and low resistance make SnO_2 attractive for the production of transparent conductive coatings. The ability of the lattice oxygen to participate in chemical reaction and, at by its end, to be renewed by the oxygen from the gas phase, allows to use SnO_2 as a catalyst for oxidation processes. Tantalum-doped SnO_2 serves as capacitor electrodes in next-generation dynamic random access memory (DRAM) [1-8].

The properties of tin oxide films depend on surface homogeneity, stoichiometry, adhesion to the surface of the substrate, and other parameters. The dominant mechanism of the formation of spatial structures is self-organization, a significant contribution to which is made by doping additives [9-12]. At the same time, the preparation method (magnetron sputtering, sol-gel method, etc.) has a significant effect on the formation of the films.

In this work, films were obtained by the sol-gel method. Due to the mild conditions of solution chemistry, this method ensures the formation of the SnO_2 compound without the appearance of other tin oxides in the films [13].

The method of films applying to a substrate, as a part of the producing process of investigated sample and a device based on it, effects on quality and cost. Quality, in particular, is associated with the application of a coating uniform in thickness, as well as its purity. An important aspect is the speed and controllability of the coating applying process. In sol-gel technology, there are three methods for applying

films - dipping, spin-coating and spray pyrolysis. These methods are low cost, due to do not involve complex equipment and simple in use.

The work advantage is a comprehensive analysis of SnO_2 films which synthesized by the sol-gel method and deposited by various methods to obtain coatings with increased transparency and surface conductivity.

2 Materials and Methods

Tin oxide films were obtained from the $SnCl_4$/EtOH film-forming system with a tin ion concentration of 0.11 mol/L. The formation of a sol and its transition into a gel occurred on the surface of the substrate.

When a film-forming system is applied to a substrate, tin tetrachloride reacts with water (from air, 3-3.5% in ethanol and 5 mol of H_2O per 1 mol of $SnCl_4$ in tin tetrachloride crystalline hydrate) with the formation of a tin hydroxide sol and hydrochloric acid.

$$SnCl_4+4H_2O \rightarrow Sn(OH)_4+4HCl \quad (1)$$

Evaporation of the solvent and reaction by-products leads to the interaction between the sol particles and the formation of a gel in which the solvent molecules are enclosed in a flexible, but sufficiently stable three-dimensional network formed by tin hydroxide particles.

Heating to 400°C promotes the removal of hydrochloric acid and solvent. As a result of this, $Sn(OH)_4$ decomposes to form water and the desired tin oxide by the reaction:

$$Sn(OH)_4 \quad SnO_2 + 2H_2O \quad (2)$$

As a result, a thin film of tin (IV) oxide is formed on the surface of the substrate. The surface tension was determined by the stalagmometric method. At the next step we consider each way of the film deposition in detail.

Dip coating technique. A film-forming system was applied on one side of the glass substrate, dried for 1-2 minutes and then annealed in air at 400°C for 15 minutes.

Spin coating technique. A film-forming system was applied to a substrate mounted on a spinner. Rotation speed - 3000 rpm, time - 3 seconds. Then the samples were dried with an infrared emitter from room temperature to 80°C for 1 minute. At the final stage, the samples were annealed in a muffle furnace at t = 400°C for 15 minutes.

Spray pyrolysis technique. A film-forming system was sprayed at a pressure of 1.8 atm onto a substrate heated to 400°C.

In all cases 15 layers were deposited.

The film thickness was determined by micro-weighing. When calculating the thickness of the films, the following formula was used:

$$d = (m_{sample} - m_{substrate})/(\rho_{(tin\ oxide)} * S^{substrate}) \quad (3)$$

where:

d – film thickness;

m_{sample} – mass of the sample;

$m_{substrate}$ – mass of the glass substrate;

ρ_{tin} – oxide is the density of cassiterite taken as 7 g/cm^3;

$S_{substrate}$ – area of the glass substrate.

3 Results and Discussion

The transmission spectra were measured on a UNICO SpectroQuest 2800 spectrophotometer. The morphology of the films was studied using a JSM-6490LA, JEOL scanning electron microscope. The structure of the films was determined using x-ray diffraction analysis on a DRON-6 diffractometer.

Table 1 shows the thicknesses of the films calculated by the micro-weighing method.

Table 1 – Film thickness calculated from micro-weighing measurement

Deposition technique	Thickness, nm
Dip coating	270±14
Spin coating	250±14
Spray pyrolysis	290±14

From the Table 1 it is seen that the thickness of the films varies from 250 nm to 290 nm. It is assumed that the film is uniformly distributed over the surface of the substrate and has the density of a natural SnO_2 crystal (cassiterite).

Figure 1 shows the distribution of forces acting on the film-forming system, depending on the deposition method.

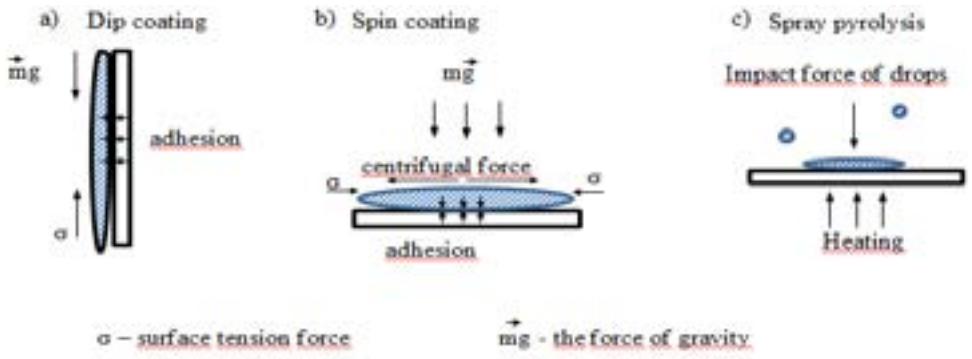

Figure 1 – Scheme of the distribution of forces depending on the deposition technique

As can be seen from Figure 1a, when a film-forming system is applying by dipping, the force of gravity, the adhesion force to the substrate surface and the surface tension force act on the $SnCl_4$/EtOH system. The net force tends to gather the fluid into the sphere.

In this case, adhesion causes a bonding between the solid substrate and the fluid contacting with it. Wetting is the result of such a bond. The Dupre-Young equation [14-15] shows the relationship between adhesion and wetting:

$$W_a = \sigma_{12} (1 + \cos \theta) \quad (4)$$

where σ_{12} is a surface tension at the interface between two phases (liquid-gas); θ is a contact angle; W_a is a reversible work of adhesion.

The surface tension of the film-forming system = $21.8 \cdot 10^3$ N/m, the contact angle in the system "glass substrate / film-forming system" (θ) tends to zero. Then $W_a \approx 43.6 \cdot 10^3$ N/m.

On the lower part of a vertically arranged substrate, there is a formation of a liquid drop that is balanced by gravity and surface tension. At this, on the upper part of the sample, the evaporation of the solvent and the course of reaction (1) lead to the formation of solid phase of $Sn(OH)_4$ (sol) and its structuring (gel). Removing a drop of a film-forming solution from a sample, we take a portion of the liquid mass, thereby disturbing the force balance. Now the forces of surface tension prevail, and the film-forming system moves up until the force balance is reached. At this time, the film thickness increases in this place. Further annealing fixes the obtained film on the substrate. Thus, in case of dip coating technique, the film has a thickness variation in different parts of the sample.

During spin-coating deposition (Fig. 1b), such forces as adhesion, surface tension and centrifugal force act on the film-forming system. The speed and time of rotation were selected experimentally based on the fact that the surface should be smooth. Under the action of centrifugal forces, part of the film-forming system "flies away" from the surface of the substrate. There is a formation of a thin layer, which, after the rotation stop, begins to pull toward the center from the substrate edges under the action of surface tension. There might be a fracture formation due to small surface defects, which breaks the film integrity. To fix the layer, the film was heated by an infrared emitter immediately after the rotation stop and then annealed.

Films obtained by spin coating are more uniform in thickness, in contrast to films prepared by dipping technique. However, the interference pattern is observed along the edge of substrate at a distance of about 0.5 cm. This indicates the thickness inhomogeneity of the film.

Deposition by spray pyrolysis (Fig. 1c) takes place on a hot substrate. The film-forming system is supplied under pressure. The main role is played by the size and sedimentation rate of the droplets. Contact with a hot substrate leads to evaporation of the solvent and the course of reactions (1) and (2).

In this case, the interference pattern was not observed on the obtained samples. This indicates a more uniform layer thickness.

3.1 Surface morphology

Analysis of the surface morphology of obtained samples using electron microscopy showed that the films prepared by dip coating contain blisters, depicted in Figure 1.

The figure on the left shows open- and closed-type blisters; the right image shows the sizes of the open blister.

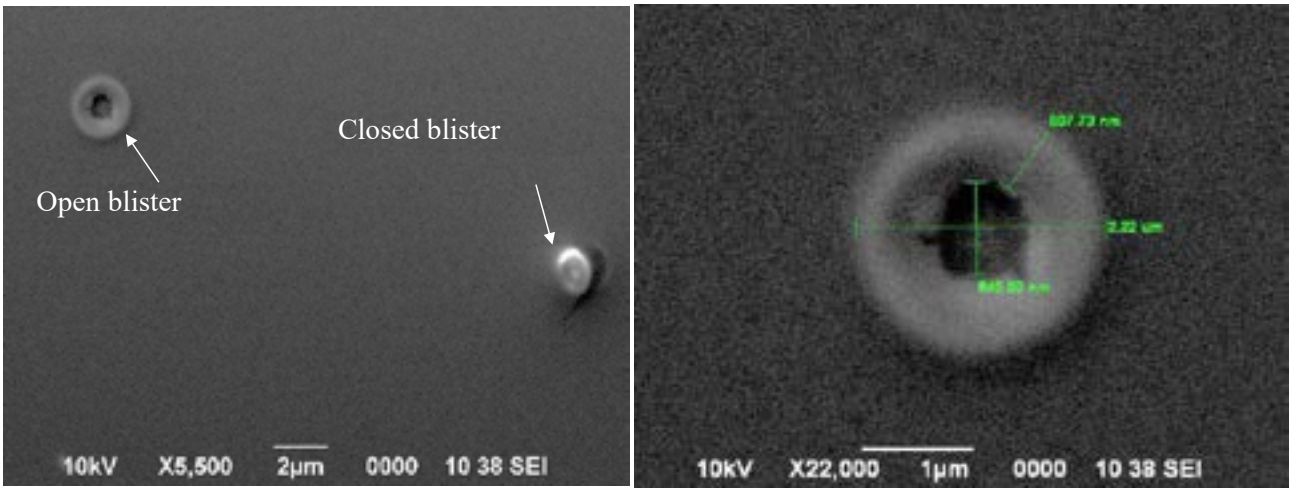

Figure 2 – Blisters on the surface of a film deposited by dip coating technique

In this work, multilayer films were obtained. Each layer was annealed at 400°C. The deposition of layers on a substrate that not cooled down completely (the temperature of the each layer is not exceed 60°C), leads to the formation of solvent vapors and reaction products at the "film – substrate" interface. The vapors "lift" an unhardened film. Thus, blisters are formed when a film-forming system is applied to a heated surface. As a result, the films demonstrate inhomogeneous surface morphology [16-18].

3.2 Optical properties

Figure 3 shows the transmission spectra of thin SnO_2 films deposited by different techniques.

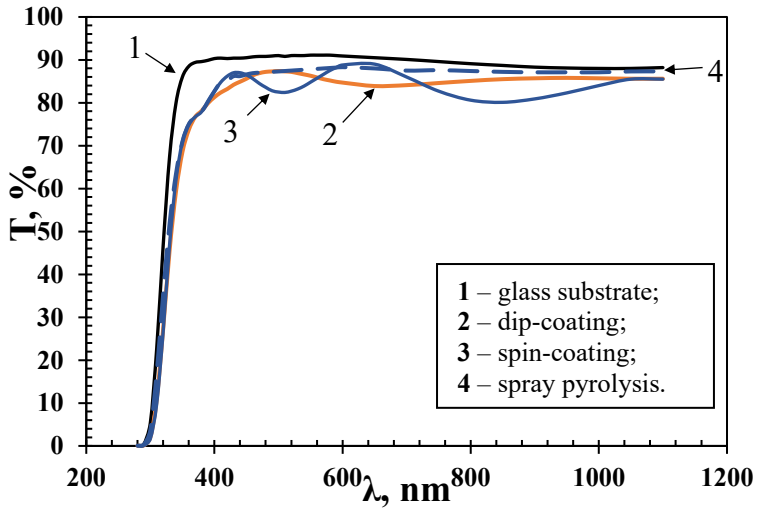

Figure 3 – Transmission spectra of films prepared by different methods

As can be seen from Figure 3, films deposited by different methods have a transmittance of more than 80% in the range λ = 380-1100 nm. This makes them attractive as transparent coatings. On the spectra of films deposited by spin coating and dip coating, interference peaks are observed. There are no interference peaks in the transmission spectrum of a film deposited by the pyrolysis spray method. The value of transmittance of the film deposited by the pyrolysis spray method is the highest and is more

than 86% in the wavelength range from 440nm to 1100nm.

Based on the available interference peaks, the parameters of the films were calculated using the envelope method [19]. The results of the calculation are shown in table 2.

Table 2 – Film parameters calculated from interference peaks

	Dip coating	Spin coating
Film thickness, nm	296	375
Extinction coefficient	$11.0 \cdot 10^{-3}$	$8.1 \cdot 10^{-3}$
Refraction index	1.689	1.722
Absorption coefficient	$2.89 \cdot 10^{3}$	$3.37 \cdot 10^{3}$

From table 2 it is seen that the thickness of the films calculated from the transmission spectra is greater than the thickness calculated by the micro-weighing method. This discrepancy is due to the difference between the density of the films and the density of cassiterite. Thus, the film deposited by spin coating is less dense than the film deposited by dipping.

3.3 Electrical resistance of the films

The resistance of the films was determined by 10 measurements in different parts of the samples. The distance between the contacts is 1 mm. Student's coefficient for 10 measurements with a reliability of 0.95 = 2.262. The error was calculated by the formula:

$$\Delta\bar{A} = t_{\gamma,n-1}\frac{\sqrt{\frac{\sum_{i=1}^{n}(A_i-\bar{A})^2}{n-1}}}{\sqrt{n}} \quad (5)$$

where is an absolute error; is a Student's coefficient; is a value of the i-th measurement; is an arithmetic mean value, *n* is the number of measurements.

Table 3 – The average values of the active resistance of the films

Deposition technique	**Resistance**
Dip coating	198±29 kΩ
Spin coating	193.5±16.6 kΩ
Spray pyrolysis	13.3±0.8 kΩ

From the Table 3 it is seen that the resistance of the films deposited by dip- and spin-coating are close. The resistivity of films deposited by spray pyrolysis is much lower and equals to 13.3 ± 0.8 kΩ.

The scatter of values over the sample surface is noteworthy. The fluctuation of the resistance value depending on the surface area equals to ± 29 kΩ (14.6%), ± 16.6 kΩ (8.6%) and ± 0.8 kΩ (6.0%) for the films deposited by dip coating, spin coating and spray pyrolysis, respectively. Films deposited by spray pyrolysis have a lower resistance and a smaller scatter of values depending on the surface area. This makes them more attractive for use as conductive coatings.

3.4 X-ray diffraction analysis

Tin oxide signal in raw XRD spectra was weakly expressed as the halo from the glass substrate prevailed. Using the method that allows to increase the signal-to-noise ratio [20], the following data were obtained and analyzed. Figure 4 shows the results of X-ray diffraction analysis of SnO_2 films.

Figure 4 show the films obtained by spray pyrolysis are amorphous. Films obtained by spin coating and dipping method contain SnO_2 crystallites.

The average crystallite size (D) of the synthesized samples was estimated by X-ray line broadening according to the Scherrer formula [21]:

$$D = (k\lambda / (\beta \cos\theta)) \quad (6)$$

where k is a Scherrer constant, usually taken as 0.9, but its value strongly depends on the crystallite shape [22]; λ is X-ray wavelength; θ is a Bragg diffraction angle; β is a line broadening at half the maximum intensity (in rad).

The measurement accuracy was calculated from the broadening of the diffraction line Δβ = 0.1 rad. The results of the calculation of crystallite sizes are shown in Table 4.

Table 4 shows that SnO_2 films deposited by dip coating and spin coating are nanocrystalline. The crystallite size does not exceed 10.3 nm.

The formation of the amorphous structure of the films obtained by spray pyrolysis is probably associated with the high rate of reactions (1) and (2), since deposition occurs on a heated substrate. Consequently, crystallite formation will occur with further increase in the duration and temperature of annealing.

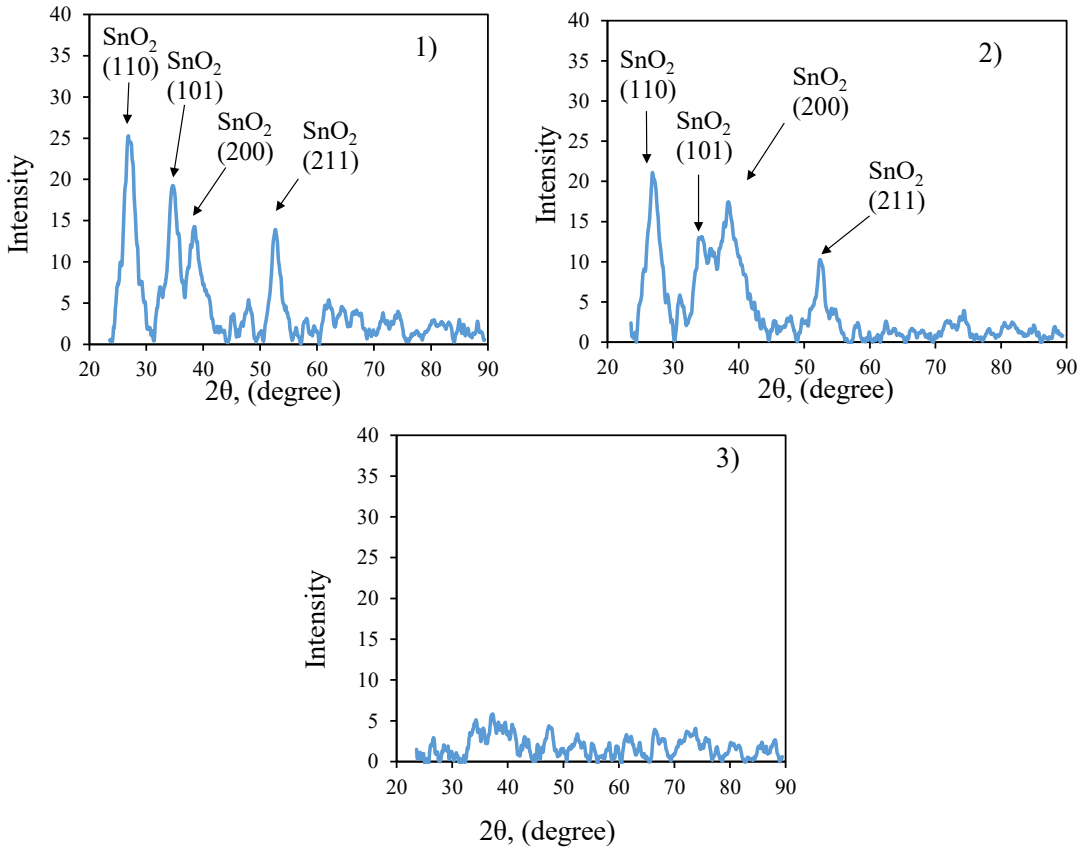

Figure 4 – X-ray diffraction pattern of films deposited by different techniques (1 – dip coating, 2 – spin coating, 3 – spray pyrolysis)

Table 4 – Sizes of SnO_2 crystallites

Deposition technique	SnO_2			
	(110)	(101)	(200)	(211)
Dip coating	6.2±0.2 nm	6.6±0.2 nm	7.7±0.2 nm	9.1±0.3 nm
Spin coating	6.5±0.2 nm	5.2±0.2 nm	4.6±0.2 nm	10.3±0.3 nm

4 Conclusions

Visual inspection and SEM analysis showed that films deposited by spray pyrolysis technique demonstrate the best surface morphology and thickness uniformity, comparing to films formed by dip coating technique that contain blisters, and spin coated films having interference patterns on the edges.

Films deposited by all three different methods have a transmittance of more than 80% in the range of 380-1100 nm. However, the highest transmittance of 86%, and the minimum electrical resistance were observed in the films deposited by spray pyrolysis. Moreover, the films obtained by this method demonstrate the highest sheet resistance uniformity (with the value scatter of 6%). These qualitative advantages make spray pyrolysis deposition technique the effective and optimal method for creating transparent conductive coatings based on tin dioxide.

XRD analysis revealed that dip coating and spin coating deposition techniques form nanocrystalline SnO_2 films, with the crystallite size of 10.3 nm and less. Films deposited by spray pyrolysis have an amorphous structure. This explained by the high rate of sol-gel processes on heated substrate. The process of the crystallites formation in this method can be controlled by increasing the duration and temperature of annealing.

Acknowledgments

This research was funded the program № AP09058002 «Investigation of the properties of dynamic memory based on Si_3N_4/Si and the formation of silicon nanoclusters with increased photoluminescence intensity» by the Committee of Science of the Ministry of Education and Science of the Republic of Kazakhstan.

References

1. E.A. Dmitriyeva, D.M. Mukhamedshina, K.A. Mit', I.A. Lebedev, I.I. Girina, A.I. Fedosimova, E.A. Grushevskya. Doping of fluorine of tin dioxide films synthesized by sol-gel method // News of the National Academy of Sciences of the Republic of Kazakhstan (series of geology and technical sciences). – 2019. – Vol.433. – P.73-79. https://doi.org/10.32014/2019.2518–170X.9.

2. E.A. Grushevskaya, S.A. Ibraimova, E.A. Dmitriyeva, I.A. Lebedev, K.A. Mit', D.M Mukhamedshina., A.I. Fedosimova, A.S. Serikkanov, A.T. Temiraliev. Sensitivity to ethanol vapour of thin films SnO_2 doped with fluorine // Eurasian Chemico Technological J. – 2019. – Vol.21. – P.13–17. https://doi.org/10.18321/ectj781.

3. H.F. Guo, Z.W. Chen, X. Wang, Q.F. Cang, C.H. Ma, X.G. Jia, N.Y. Yuan, J.N. Ding. Significant increase in efficiency and limited toxicity of a solar cell based on Sb_2Se_3 with SnO_2 as a buffer layer // Journal of Materials Chemistry C. – 2019. – Vol. 7(45). – P. 14350–14356, https://doi.org/10.1039/c9tc04169a.

4. D. Wang, S.C. Chen, Q.D. Zheng. Poly(vinylpyrrolidone)-doped SnO_2 as an electron transport layer for perovskite solar cells with improved performance // Journal of Materials Chemistry C. – 2019. – Vol.7 (39). – P. 12204-12210. https://doi.org/10.1039/c9tc04269e.

5. B. Matthias, D. Ulrike. The surface and materials science of tin oxide // Progress in Surface Science. – 2005. – Vol. 79. – P. 47–154. https://doi.org/10.1016/j.progsurf.2005.09.002.

6. R.Y. Zhang, F.F. Zhu, Y. Dong, X.M. Wu, Y.H. Sun, D.R. Zhang, T. Zhang, M.L. Han. Function promotion of SO_4 2-/Al_2O_3-SnO_2 catalyst for biodiesel production from sewage sludge // Renewable energy. – 2020. – Vol. 147. – P. 275– 283. https://doi.org/10.1016/j.renene.2019.08.141.

7. Z. Chen, T.T. Fan, Y.Q. Zhang, J. Xiao, M.R. Gao, N.Q. Duan et al. SnO_2 catalyzed simultaneous reinforcement of carbon dioxide adsorption and activation towards electrochemical conversion of CO_2 to HCOOH // Applied catalysis b-environmental. – 2020. – Vol. 261. – P. 118243–118249. https://doi.org/10.1016/j.apcatb.2019.118243.

8. B.H. Zhang, L.Z. Sun, Y.Q. Wang, Chen S., J.T. Zhang. Well-dispersed SnO_2 nanocrystals on N-doped carbon nanowires as efficient electrocatalysts for carbon dioxide reduction // Journal of energy chemistry. – 2020. – Vol. 41. – P. 7–14. https://doi.org/10.1016/j.jechem.2019.04.022.

9. C.J. Cho, M.S. Noh, W.C. Lee, C.H. An, C.Y. Kang, C.S. Hwang, S.K. Kim. Ta-doped SnO_2 as a Reduction-Resistant Oxide Electrode for DRAM Capacitors // Journal of Materials Chemistry C. – 2017. – Vol. 5(36). – P. 9405-9411. https://doi.org/10.1039/c7tc03467a.

10. A.I. Fedosimova, E.A. Dmitrieva, I.A. Lebedev, A.T. Temiraliev, M.E. Abishev, B.A. Baitimbetova, Yu.A. Ryabikin, A.S. Serikkanov. Modeling the process of formation of fractal structures in thin films // IOP Conf. Series: Journal of Physics: Conf. Series. – 2018. – Vol. 1141, Id. 012004. – P. 1–7. https://doi.org/10.1088/1742–6596/1141/1/012004.

11. D.M. Mukhamedshina, A.I. Fedosimova, E.A. Dmitriyeva, I.A. Lebedev, E.A. Grushevskaya, S.A. Ibraimova, K.A. Mit', A.S. Serikkanov. Influence of plasma treatment on physical properties of thin SnO_2 films obtained from $SnCl_4$ solutions with additions of NH_4F and NH_4OH // Eurasian Chemico-Technological Journal. – 2019. – Vol.21(1). – P.57 – 61. https://doi.org/10.18321/ectj791.

12. E.A. Dmitrieva, D.M. Mukhamedshina, N.B. Beisenkhanov, K.A. Mit'. The effect of NH_4F and NH_4OH on the structure and physical properties of thin SnO_2 films synthesized by the sol-gel method // Glass Physics and Chemistry. – 2014. – Vol.40. – No1. – P. 31-36. – https://doi.org/10.1134/S1087659614010076.

13. J.W. Drelich, L. Boinovich, E. Chibowski, C. Della Volpe, L. Holysz, A. Marmur, S. Siboni. Contact angles: History of over 200 years of open questions // Surface Innovations. – 2020. – Vol. 8(1-2). –P. 3-27. https://doi.org/10.1680/jsuin.19.00007.

14. T. Guo, J.Y. He, X.L. Pang, A.A. Volinsky, Y.J. Su, L.J. Qiao. High temperature brittle film adhesion measured from annealing-induced circular blisters // Acta materialia. – 2017. – Vol. 138. – P.1–9. https://doi.org/:10.1016/j.actamat.2017.07.026.

15. I.A. Karapatnitski, K.A. Mit', D.M. Mukhamedshina, N.B. Beisenkhanov. Optical, structural and electrical properties of tin oxide films prepared by magnetron sputtering // Surface and Coat.Technol.. – 2002. – Vol. 151 – 152. – P. 76 – 81.

16. F.K. Konan, B. Hartiti, A. Batan, B. Aka. X-ray diffraction, XPS, and Raman spectroscopy of coated ZnO:Al (1−7 at%) // nanoparticles // E-Journal of Surface Science and Nanotechnology. –2019. –Vol. 17. P. 163-168. https://doi.org/10.1380/ejssnt.2019.163.

17. F.K. Konan, J.S. Ncho, H.J.T. Nkuissi, B. Hartiti, A. Boko. Influence of the precursor concentration on the morphological and structural properties of zinc oxide (ZnO) // Materials Chemistry and Physics. – 2019. – Vol.229. – P. 330-333. https://doi.org/10.1016/j.matchemphys.2018.12.082.

18. N.M. Tompakova, E.A. Dmitrieva, E.A. Grushevskaya, I.A. Lebedev, A.S. Serikkanov, D.M. Mukhamedshina, K.A. Mit. The effect of three-minute hydrogen plasma treatment on the structure and properties of SnO_2 thin films //Recent Contributions to Physics. – 2019. – № 4(71). – P. 67–74. https://doi.org/10.26577/RCPh-2019-i4–9. (in Russian)

19. N. K. Mishra, Ch.Kumar, A. Kumar, M. Kumar, P. Chaudhary, R. Singh. Structural and optical properties of SnO_2–Al_2O_3 nanocomposite synthesized via sol-gel route //Materials Science-Poland. – 2015. – Vol. 33(4). – P.714-718. https://doi.org/10.1515/msp-2015–0101.

20. D.M. Mukhamedshina, N.B. Beisenkhanov, K.A. Mit', V.A. Botvin, I.V. Valitova, E.A. Dmitrieva. Influence of plasma treatments on the properties of SnOx thin films //High Temperature Material Processes. – 2006. – Vol. 10(4). – P. 603-615. https://doi.org/10.1615/HighTempMatProc.v10.i4.110.

21. S.-K.Song. Color-octet mechanism in γ+→pJ/ψ+X // Phys. Rev. – 1999. –Vol. 60. –. P. 11137 – 11148.

22. B.N. Mukashev, A.B. Aimagambetov, D.M. Mukhamedshina, N.B. Beisenkhanov, K.A. Mit, I.V. Valitova, E.A. Dmitrieva. Study of structural, optical and electrical properties of ZnO and SnO_2 thin films // Superlattices and Microstructures. – 2007. – Vol. 42(1-6). – P. 103-109. https://doi.org/10.1016/j.spmi.2007.04.057.

Funded by Al-Farabi KazNU

IRSTI 47.09.53 https://doi.org/10.26577/phst.2022.v9.i1.06

Features of structural-phase states of Co-Cr-Al-Y composite coatings after heat treatment

As. Zhilkashinova[1,*], M. Skakov[2], Al. Zhilkashinova[1], N. Prokhorenkova[3], M. Abilev[1]

[1]Sarsen Amanzholov East Kazakhstan University, Ust-Kamenogorsk, Kazakhstan
[2]National Nuclear Center, Kurchatov, Kazakhstan
[3]D. Serikbayev East Kazakhstan Technical University, Ust-Kamenogorsk, Kazakhstan
*e-mail: a_zhilkashinova@kemont.kz
(Received 18 March 2022; received in revised form 6 May; accepted 14 June 2022)

This article describes the results of studying the structural-phase state of composite Co-Cr-Al-Y coatings in the initial state and after thermal treatment, obtained because of using the developed magnetron method for applying multilayer coatings with a controlled concentration of constituent elements. According to the results of SEM measurements, it was revealed that unannealed coatings form dense coatings with a columnar structure. The results of transmission electron microscopy confirm the SEM and EDS measurements, and there are clear layer boundaries in the structure for each type of multilayer coating. A distinctive feature of the synthesized layers is the almost complete absence of a crystalline structure for all types of Co-Cr-Al-Y multilayer coatings, which is apparently due to the amorphous properties of cobalt and its tendency to form metallic glasses. The main process occurring during the heat treatment of the studied multilayer coatings is the formation of a spinel-type phase.
The obtained results of experimental studies give new, deeper ideas about the processes of formation of structural-phase states of composite coatings obtained by magnetron sputtering.

Key words: coating; structural-phase state; magnetron; phase; spinel; layer-by-layer deposition.
PACS number: 82.90.+j

1 Introduction

One of the urgent problems in the field of mechanical engineering is the development of technology for improving the strength and performance properties of coating materials for critical parts of power plants [1]. Of great importance is the development of new methods of influencing the structure and properties of coatings, and the complex use of existing developments, the optimal combination of which can create new opportunities for directed influence on the structure and properties of the resulting coatings [2, 3]. At the same time, the structural-phase state has a significant impact on the physical, mechanical and operational properties of coatings.

The vast majority of heat-shielding coatings, including those for gas turbine blades, have an operating principle based on the ability of the surface layer of such coatings to oxidize with the formation of a protective film based on aluminum oxide Al_2O_3 [4]. The chemical composition (and mainly the amount of aluminum) is the main factor that determines the performance and other protective properties of such coatings [5, 6]. Therefore, in the bulk of the work on the study of heat-shielding coatings, considerable attention is paid to establishing the relationship between the composition of the coating and its protective properties. The relationship between the structure and properties of the coating is analyzed slightly [7].

However, all the accumulated experience in the development and operation of gas turbines shows that, in addition to the chemical composition, one of the most important characteristics of a heat-resistant coating should be considered its structure [8-11]. The coating structure determines not only its strength, ductility, fracture toughness, fatigue resistance, and other properties, but also its heat resistance [12]. Obtaining an optimal structure is

an important condition for achieving the required properties of coatings [13]. Therefore, the further industrial development and widespread use of new effective heat-resistant coatings and progressive fundamentally new technologies for their creation are undoubtedly associated with the need for deep systematic structural studies of these coatings at all stages of their creation and operation, identification of the general patterns of structure formation of both coating materials and the coating itself, the diffusion interaction of the coating with the protected heat-resistant alloy and with the protective oxide film, the processes of change and degradation of the structure under the influence of a wide variety of external factors. These factors determine the role and mechanisms of influence of a particular alloying element or a complex of such elements on the formation of the structure and properties of the coating during deposition and technological heat treatment, on the dynamics of degradation of both structure and properties during operation [14-17].

Methods for studying the states and properties of coatings are widely covered in the literature [18]. Along with a large number of publications devoted to the original research, there are reviews on this topic, monographs, textbooks and reference books [19,20].

However, the above studies were mainly based on coating methods, while studies in terms of the structural-phase state and the relationship between the structure and properties of the coating were not fully investigated.

Along with this, the study of composite coatings is of great interest from a scientific point of view. They can have effects that other materials do not have. The microstructure of a film differs significantly from the structure of a bulk material of the same composition, and the properties of thin films are largely determined by their morphology. Structural defects in bulk materials, which do not significantly affect the properties, in thin films can radically affect their behavior. Surface roughness practically does not affect the characteristics of bulk materials, while for film materials it can be a factor that determines many parameters. Therefore, when studying thin-film materials, it is possible to discover new phenomena and patterns that can become the basis for creating fundamentally new technologies and devices.

At the same time, the analysis showed the relevance of studying the structural-phase state and properties of composite coatings, since at present, in conditions of limited material resources in the industrial complex, technologies that increase the durability (resource) of machine parts and assemblies are of particular importance.

The aim of this work is to study the structural-phase state of the composite Co-Cr-Al-Y coating obtained by using the developed magnetron method for applying multilayer coatings with a controlled concentration of constituent elements, in the initial state and after heat treatment.

2 Materials and methods

The object of the study was Co-Cr-Al-Y multilayer coatings (1-, 2-, 4-, and 8-layers), which were deposited on a single-crystal silicon substrate with [100] crystallographic orientation.

The coatings were deposited by the magnetron method on an ion-plasma setup, which was a vacuum chamber with two magnetron-sputtering systems of an unbalanced type and an ion source with a closed electron drift [21].

The structural-phase state and elemental composition were determined by scanning electron microscopy using a JEOL-2200FS (Japan) (EDX) INCA ENERGY scanning electron microscope (Oxford Instruments, UK). Accelerating voltage was up to 30 kV; resolution was up to 3 nm, instrumental magnification was up to x300,000. Samples were placed in a mold with a diameter of 30 mm, filled with epoxy filler, dried, and then the resulting puck was ground and polished.

The structure and microstructure of the annealed samples were studied using a ThemisZ electron microscope (Thermo Fisher Scientific, USA) with an accelerating voltage of 200 kV and a limiting resolution of 0.07 nm. Images were recorded using a Ceta 16 CCD array (Thermo Fisher Scientific, USA). The instrument is equipped with a SuperX (Thermo Fisher Scientific, USA) energy-dispersive characteristic X-ray spectrometer (EDX) with a semiconductor Si detector with an energy resolution of 128 eV.

Sample preparation for TEM studies was reduced to obtaining a cross section by grinding with etching. A scratch was applied with a scriber (Fine Point Diamond Scriber 54467, Ted Pella, USA) to the substrate on the reverse side of the sample. The coated substrate is cleaved along the scratch line by applying the required scalpel pressure. Bonding of individual parts takes place with the front sides (films on substrates) in such a way that two ends

become visible. A special epoxy two-part adhesive EpoxyBond 110TM 2-Part Adhesive manufactured by Allied High Tech Products, Inc. was used.

A quartz cylinder with a diameter of 5 mm was used. Wax was applied on the surface of this cylinder and a gluing of the samples was attached with the ends up. Then the sample was polished at the LEICA EM TXP grinding and polishing plant. The samples were subjected to additional thinning using ion etching. The copper ring with the sample was placed in a special holder for the Gatan Precision ION polishing system model 691 ion etching station. The sample was placed in the microscope holder EM-21010/21020: Single Tilt Holder for TEM JEOL-2200FS (JEOL, Japan) (Figure 1).

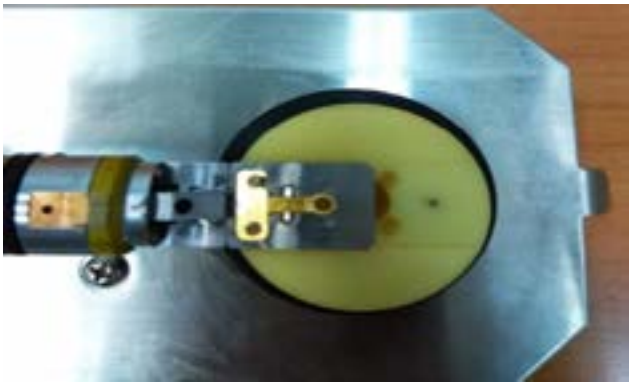

Figure 1 – Sample holder EM-21010/21020: Single Tilt Holder for TEM JEOL-2200FS

X-ray phase analysis was performed on a Shimadzu XRD 6000 instrument with a Cu anode Kα (λ = 0.154 nm) by the grazing beam method (shooting angle 15°) in the range 2θ = 20-80°. Due to the low intensity of the peaks, the initial signal was approximated by Gaussian curves. Studies were also carried out using the X-ray powder diffraction method on the ARLX'tra instrument (ThermoFisher Scientific). The sample before each shooting was fixed with glue on an amorphous polycarbonate cuvette. Shooting of film samples was performed using symmetrical (Bragg-Brentano) geometry, in the angle range of 15-70°, and asymmetric geometry, in the range of 20-50°. The PDF-2 database compiled by the International Committee on Diffraction Data JCPDS (ICDD) was used as a reference file.

The heat treatment of the coatings was carried out on a MILA-5000 unit (ULVAC-RICO (Japan), equipped with IR halogen lamps with a total power of 4 kW and a maximum radiation intensity in the range of 0.8-1.2 μm. The unit allows operation in the temperature range from up to 1000 °C with a maximum temperature increase rate of 100 °C/min. On this installation, work was carried out to heat the samples at 400 °C, 800 °C and 1000 °C. The heating took place in a programmed mode with a given rate of reaching the desired temperature, as well as during the transition from one annealing temperature to another. The annealing time at a given temperature or sequentially at several temperatures also passed in the programmed mode.

3 Results and discussion

The study of the structure and composition of multilayer coatings was carried out using electron microscopy. One of the results of the study of the cross section of coatings and the corresponding energy dispersive spectrum is shown in Figure 2.

According to the results of SEM measurements, it was revealed that the Co-Cr-Al-Y system forms dense coating with a columnar structure typical for metal coatings. The images on Figure 2 show that during the deposition process a coating was formed, which has a high-relief character. The thickness of all synthesized Co-Cr-Al-Y coatings varies within 2.0±0.2 μm, and the thickness of an individual layer is 0.4 μm. The distribution of the constituent elements of the coating from point to point practically does not change. We believe that the presence of silicon atoms in the composition of the coatings is due to it's getting there precisely from the detection of the substrate itself, since the distribution of silicon atoms over the depth and width of the coating is uniform. The presence of an oxygen peak in the EDS spectrum is due to its adsorption on the cut surface after removal from the vacuum chamber.

Transmission microscopy results confirm the SEM and EDS measurements. Figures 3 and 4 show transmission microscopy images and corresponding elemental mapping. Elemental mapping by constituent elements showed that with a relatively uniform distribution of Al and Y in the thickness of the coating, the layers of enriched/depleted Co/Cr alternate in accordance with the parameters of magnetron sputtering described in [22, 23]. A large amount of Y in the substrate during elemental mapping is associated with the superposition of the spectra of Y and Si in the EDS spectrum.

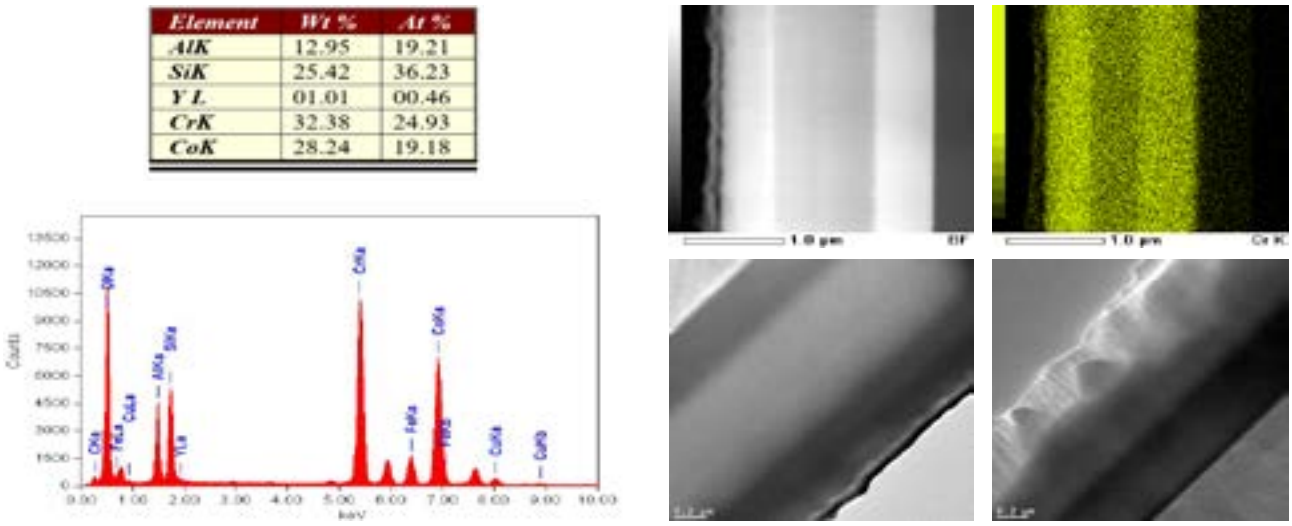

Element	Wt %	At %
AlK	12.95	19.21
SiK	25.42	36.23
Y L	01.01	00.46
CrK	32.38	24.93
CoK	28.24	19.18

a) b)

Figure 2 – An energy dispersive spectrum (a) of the coatings and SEM images of a cross section of the coating (four-layer coating) (b)

A distinctive feature of the synthesized layers is the almost complete absence of a crystalline structure for all types of synthesized multilayer Co-Cr-Al-Y coatings, which is most likely due to the amorphous properties of cobalt and its tendency to form metallic glasses.

Figure 4 shows that the structure of the samples is columnar, microcracks are noticeable, which may indicate the presence of microstresses in the film, while ion etching showed these microstresses. However, it is possible that ion etching slightly destroys the film during thinning, and microcracks may be a consequence of the destruction of the film surface.

Film layering is also clearly visible in all TEM images. In the STEM mode, the number of layers is displayed more clearly, the boundaries of all layers are clear, which means that the process of layer growth during deposition took place in the optimal mode.

Elemental analysis showed that Co and Cr are distributed in the layers in the form of a gradient. At the same time, the content of Co in a single-layer coating is the maximum value – 27.63%, in a 4-layer coating – the minimum value – 19.4%. The chromium content, on the contrary, increases with the increase in the number of layers. So, in a single-layer coating, this value is 18.82%, and in an 8-layer coating – 24.15%. Aluminum is evenly distributed over all layers of the film. Its content remains largely unchanged. In a 1-layer coating – 9.75%, 4-layer – 8.85%. Yttrium is located in the form of a small thin layer at the film/substrate interface; during thinning with the help of ion argon guns, it is etched away until destruction (EDS detects a weak peak that "merges" with a large silicon peak). The silicon content in the coating in 1, 2 and 4-layer coatings is in the range of 5.00 – 5.44%. In this case, in an 8-layer coating, this value is 3.89%. This is due to the formation of a diffuse region at the film–substrate interface. The oxygen content in the multilayer coating was found to be in the range of 10-20%. The presence of oxygen in the surface layer of the coatings is due to its adsorption on the cut surface after removal from the vacuum chamber, as well as after argon etching.

Figure 5 shows the results of X-ray phase analysis by the method of a grazing beam of coating samples of 4- and 8-layer coatings.

For all synthesized Co-Cr-Al-Y coatings, the main peaks can be distinguished: $2\theta \approx 30°$ and 57°, corresponding to the peaks of the first and third order of the silicon substrate (111). Dominant peak of Cr (110) at $2\theta \approx 43°$, pronounced for multilayer coatings of 2- and 8-layers and much less intense for a single-layer coating. This correlates with the significantly lower Cr concentration in the single layer coating measured from the EDS results. Fourth order peaks are Y(411) and Y(444). The absence of Co and Al peaks is probably because they form an X-ray amorphous layer, which is confirmed by the results

of TEM. Summing up the results of TEM and XRD, we can state the formation of an amorphous Co/Al matrix with Cr and Y nanocrystals distributed in the thickness of the coating. The formation of intermetallic compounds in the deposited Co-Cr-Al-Y system was not detected.

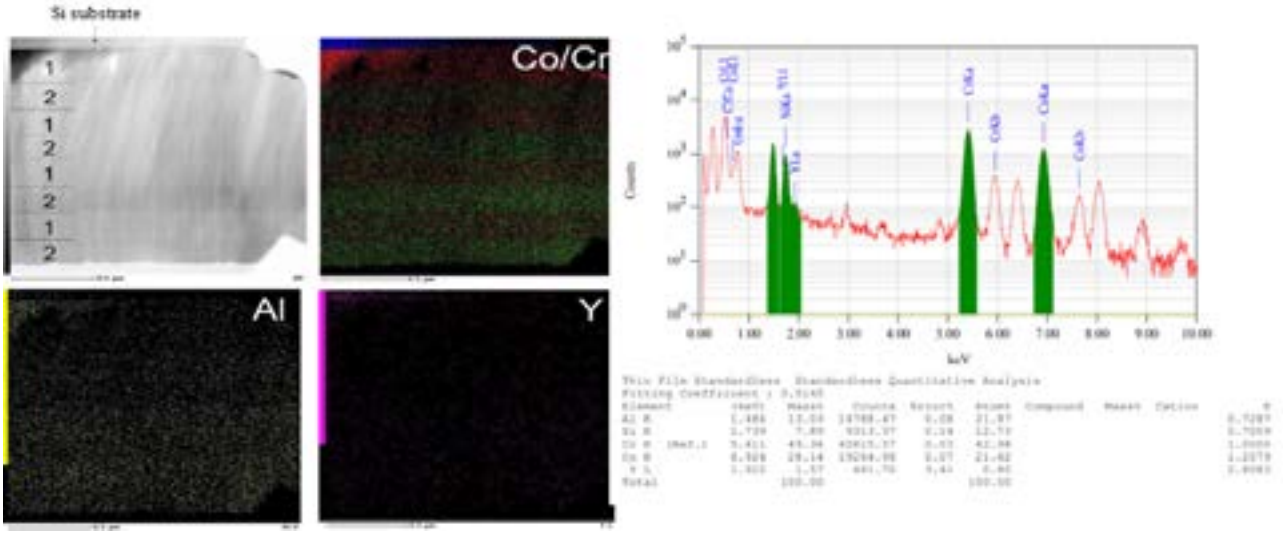

a) b)

Figure 3 – TEM images of the cross section of the coating (a) and its elemental mapping (four-layer coating) (b)

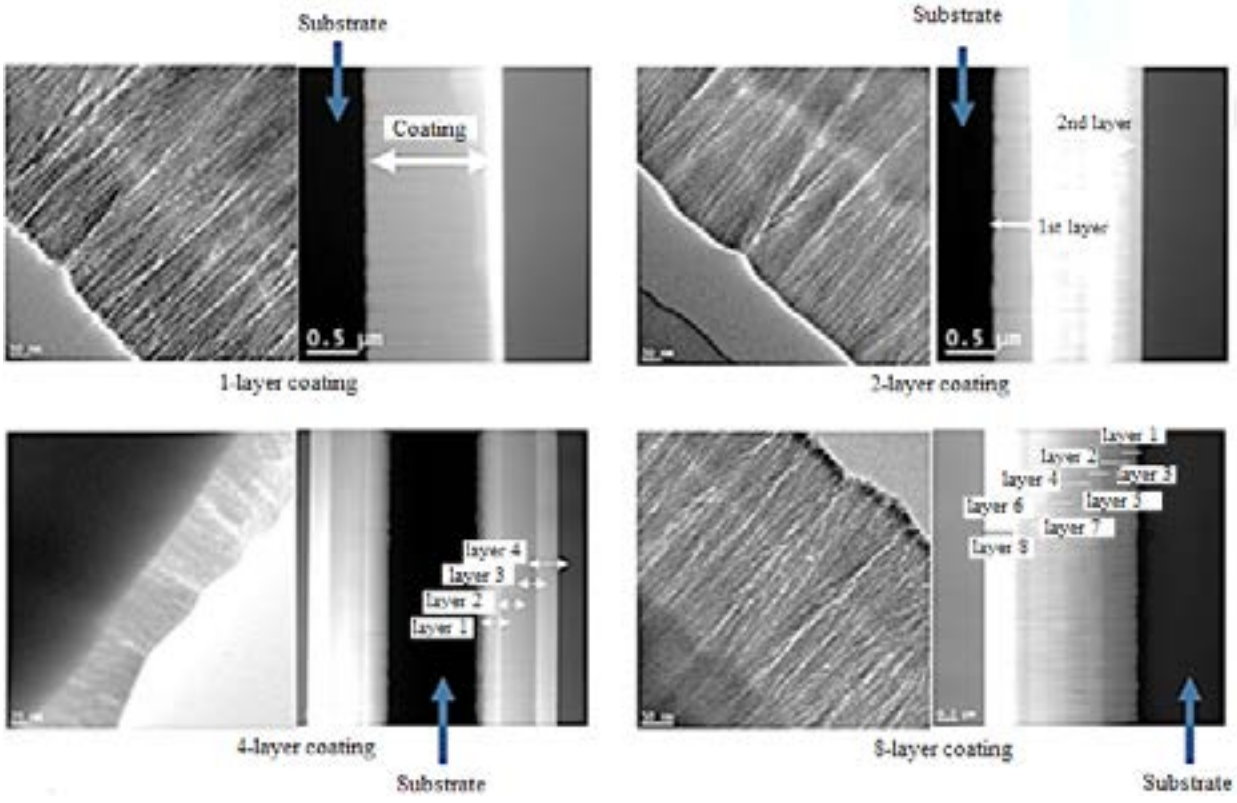

Figure 4 – Microstructure of various sections of all series of coatings

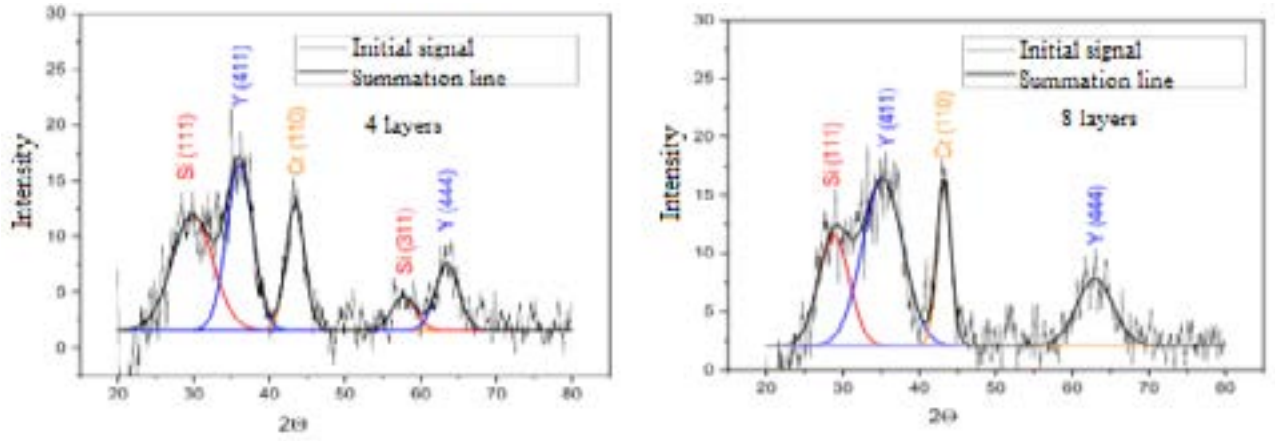

a) b)

Figure 5 – X-ray phase analysis: (a) four-layer coating; (b) eight-layer coating

The results of studies of the structural-phase state of Cr-Al-Co-Y coatings because of thermal treatment in an Ar medium at 400 °C showed some changes in comparison with untreated samples. In the case of the single-layer sample, it was not possible to detect extraneous reflections except for the reflections of the silicon substrate 111 and 220. These reflections are mainly due to the defocus of the incident beam on the sample at small angles of incidence. However, for the remaining samples, the appearance of reflections of a number of phases was noticed: SiO_2, CoO, $AlSi_{0.5}O_{2.5}$, and $CrAl_{0.42}Si_{1.58}$.

A further increase in the annealing temperature in Ar at 800°C does not lead to significant changes. In the case of a sample consisting of two composite layers, the reflections of various impurity phases disappeared and the Co_3O_4 phase was formed. It should be noted that the $CoCr_2O_4$ phase, which also has a spinel-type structure, has a similar set of reflections in position and intensity, and the elemental analysis data showed a fairly homogeneous distribution of chemical elements in the material. In this regard, overlapping of peaks in the diffractogram may occur, and this phase, meanwhile, may be present in the sample. In the case of the sample with eight layers of the composite, the formation of a phase similar to Y_2O_3 was also observed.

For samples annealed at 1000 °C, the formation of a spinel-type phase (Co_3O_4–$CoCr_2O_4$) was observed in all cases. In the sample with two layers, impurities were also found similar to those observed at lower annealing temperatures, but were not observed for the sample annealed at 800°C. In this case, this is because the samples had different areas and, therefore, contained different amounts of the substance, based on which the reflections of impurity phases could not be observed in the case of one sample, but the phases themselves could be preserved. In the case of 2-layer and 4-layer composites, the yttrium oxide phase was detected (Figure 6).

The structure of the samples, as well as in the unannealed ones, is columnar, the same microcracks are observed as in the unannealed samples. The layers are clearly distinguishable on the TEM, STEM images, and on the EDS maps. There is a "mixing" of elements in the layers of annealed samples (Figure 7).

Similarly, to the previous series (annealed at 400°C), there is a "mixing" of elements in the film layers.

The structure of the samples annealed at 1000°C is shown in Figure 8.

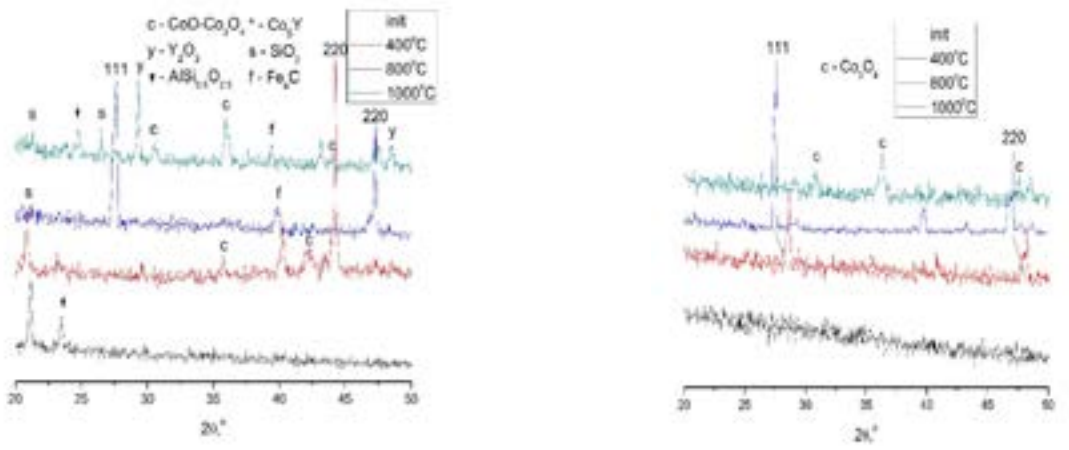

a) b)

Figure 6 – X-ray diffraction patterns of the Y-Co-Al-Cr sample in asymmetric geometry depending on the annealing temperature of the samples: (a) – single-layer; (b) – four-layer coatings

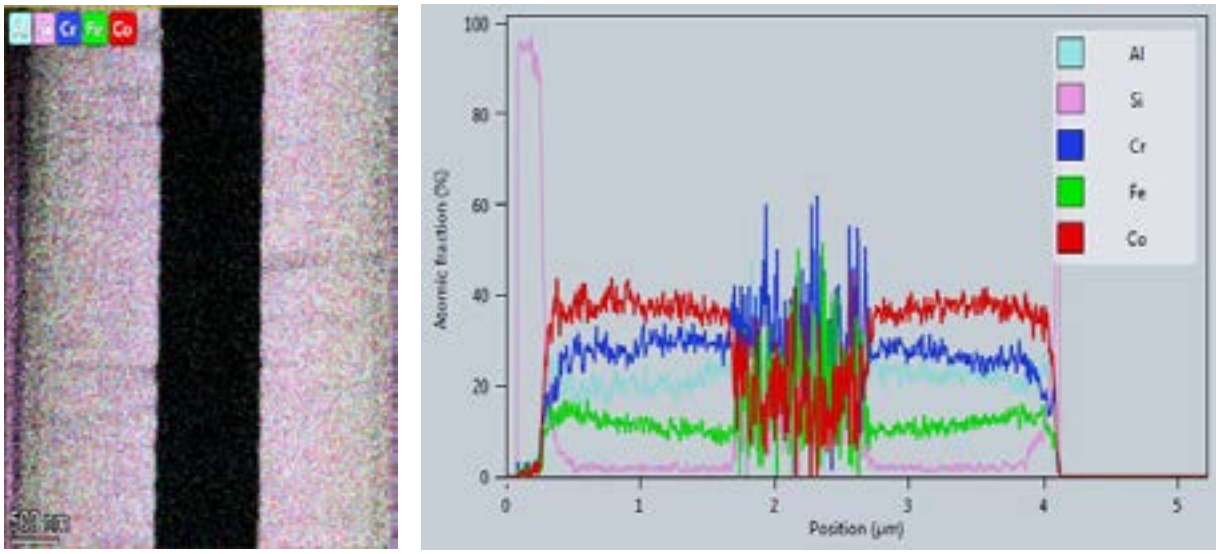

Figure 7 – EDS analysis of single-layer coating at 1000 °C

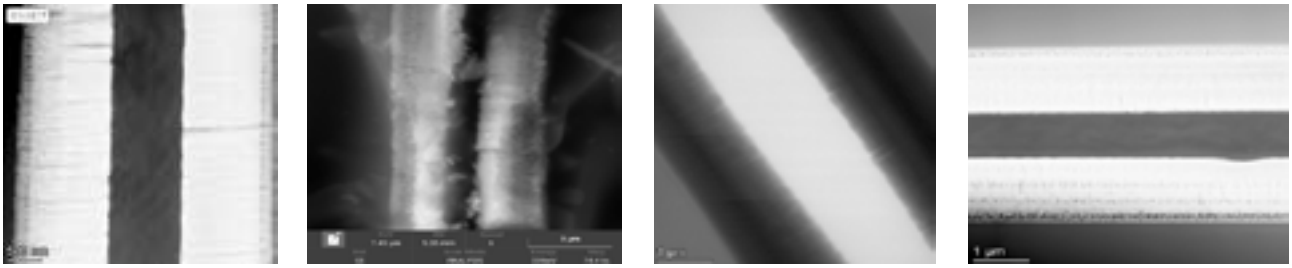

a) b) c) d)

Figure 8 – Structure of samples annealed at 1000°C: (a) 1-layer; (b) 2-layer; (c) 4-layer; (d) 8-layer samples

.The structure is similar to all previous samples; the presence of layers is clearly distinguishable in all modes of TEM (also SEM). As with the previous annealed samples, mixing of the film layers is noticeable. The silicon content in the coatings after heat treatment increased significantly – more than 10 times. This applies to 1-layer coating (400°C) – 29.52%, 2-layer coating (400°C) – 33.10%. It was observed that the cobalt content decreases with increasing annealing temperature. So, for 1, 2, 4 and 8-layer coatings annealed at a temperature of 400°C, the cobalt content is 31.30; 17.10; 7.57; 3.58% respectively. For 1, 2, 4, and 8-layer coatings annealed at 800°C, the cobalt content is 4.00; 19.91; 4.50; 10.37% respectively. Aluminum is distributed evenly over all layers of the film. The maximum content of Al in 1-layer coatings subjected to thermal treatment at temperatures of 400 and 1000˚C. The minimum value for the Al content is set in the 8-layer coating (400˚C) – 1.49%. In the remaining samples, this figure ranges from 3.60 to 8.22%. Chromium and cobalt are distributed in a gradient. The average value of the chromium content is generally similar to samples without thermal treatment. However, it has been found that for 8-layer (400°C), 1-layer (800°C) and 2-layer (1000°C), the chromium content is 1.38, 3.20 and 4.60%, respectively. After heat treatment of coatings, it was possible to establish the content of Y: in 1-layer (400˚C) – 0.72%, in 8-layer (400˚C) – 0.04%, in 1-layer (1000˚C) – 0 .97%, in 4-layer (1000˚C) – 0.32%, in 8-layer (1000˚C) – 0.52%. At an annealing temperature of 400°C, the oxygen content in 1 and 8 layer coatings was not established, similarly for 1 and 4 layer coatings at a processing temperature of 1000°C. The oxygen content in 2 and 4 layer coatings at the annealing temperature is 25.80 and 45.82%, respectively. As noted above, the presence of oxygen in the surface layer of the coatings is due to its adsorption on the cut surface after being removed from the vacuum chamber.

4 Conclusions

The structural-phase state before and after heat treatment of multilayer Co-Cr-Al-Y coatings on a silicon substrate, obtained by the magnetron method, has been studied. According to the results of SEM measurements, it was revealed that unannealed coatings form dense coatings with a columnar structure typical for metal coatings. The total thickness of one layer of the composite coating, which includes sequential Co-Cr-Al-Y components, ranges from 2.0 ± 0.2 μm, and the thickness of a separate sublayer of each element is 0.4 μm. The study of the local and integral elemental composition of coatings shows that the matrix has a gradient character. According to the data of energy dispersive analysis, the concentration of chromium in the coating increases with an increase in the number of layers, with a proportional decrease for cobalt, which is associated with the influence of the second layer with an increased concentration of chromium.

Transmission microscopy results confirm the SEM and EDS measurements. The structure contains clear layer boundaries for each type of multilayer coating. Elemental mapping by constituent elements showed a relatively uniform distribution of Al and Y in the thickness of the coating and layers of enriched/depleted Co/Cr alternate. A large amount of Y in the substrate during elemental mapping is associated with the superposition of the spectra of Y and Si in the EDS spectrum. A distinctive feature of the synthesized layers is the almost complete absence of a crystalline structure for all types of synthesized Co-Cr-Al-Y multilayer coatings, which is associated with the amorphous properties of cobalt and its tendency to form metallic glasses.

For all Co-Cr-Al-Y coatings, the main peaks can be distinguished: $2\theta \approx 30°$ and 57°, corresponding to the peaks of the first and third order of the silicon substrate (111). Dominant peak Cr (110) at $2\theta \approx 43°$, pronounced for multilayer coatings of 2-8 layers and much less intense for a single-layer coating. This correlates with the significantly lower Cr concentration in the single layer coating measured from the EDS results.

The results of studies of the structural-phase state of Cr-Al-Co-Y coatings after the heat treatment in an Ar medium at 400 ° C showed some changes in comparison with untreated samples. The appearance of reflections of a number of phases was noticed: SiO_2, CoO, $AlSi_{0.5}O_{2.5}$, and $CrAl_{0.42}Si_{1.58}$. A further increase in the annealing temperature in Ar at 800°C does not lead to significant changes. For samples annealed at 1000°C, the formation of a spinel-type phase (Co_3O_4–$CoCr_2O_4$) was observed in all cases. In the sample with two layers, impurities were also found similar to those observed at lower annealing temperatures, but were not observed for the sample annealed at 800°C.

Based on the data obtained, it can be stated that the main process occurring during the annealing of

these composites is the formation of a spinel-type phase. In this case, despite the symbol Co_3O_4, the composition of the resulting spinel may be different, and may include Cr, Y, and Al, based on the possible charge states of these cations (Cr^{3+}, Al^{3+}, Y^{3+}). Their final formation for all samples occurs in the temperature range of 800-1000°C. In this case, the yttrium oxide phase can form separately from particles with this structure, which is due to the large size of the Y^{3+} cation. Apparently, one of the main reasons for the formation of spinel structures is the partial acidification of films, which was already demonstrated for the initial amorphous samples by the TEM method, and the uniform character of oxygen saturation of the layers indicates that the samples were acidified at the stage of their deposition onto the substrate. The calcination of samples in an inert atmosphere does not lead to the reduction of oxides, but to their crystallization. This allowed to conclude that in the future, to obtain composite layers by heat treatment, it is necessary to use a medium with a more reducing character, for example, a mixture of Ar + H_2 or He + H_2 gases, which will contribute to the reduction of the original spinels.

Acknowledgment

This research is funded by the Science Committee of the Ministry of Education and Science of the Republic of Kazakhstan (Grant No. AP08053322).

References

1. B. Bhushan. Principles and applications of tribology // Industrial Lubrication and Tribology -1999. -Vol. 51. -No. 6. -P. 313-313. https://doi.org/10.1108/ilt.1999.51.6.313.1

2. S.Ya. Betsofen, L.M. Petrov, Su S. K., A.N. Lutsenko. Study of the structure of protective coatings on a nickel heat-resistant alloy // 6th Int. Conf. "Films and Coatings'2001": Proceedings. report -SPb., 2001. – P. 477-482.

3. N.A. Khaponen, A.S. Lisyansky. Survivability of turbines near and beyond the park resource // Safety of labor in industry. – 2004. – No. 7. – P.16 (in Russian).

4. V.I. Gladshtein. Influence of operating time up to 350 thousand hours on service characteristics and structure of cast housing parts of steam turbines and fittings // Metal Science and Thermal Processing of Metals. – 2007. – No. 2. – P.21-23 (in Russian).

5. A.A. Smirnov, S.A. Budinovsky, P.V. Matveev, D.A. Chubarov. Development of heat-shielding coatings for HPT blades from nickel single-crystal alloys VZHM4, VZHM5U // Proceedings of All-Russian Research Institute of Aviation Materials, No. 1, 2016, P.17-24 (in Russian).

6. V. Kumar, A. M. Vijay, J. J. Duthie, S. Archan. Analyzing and establishing the protective coating for low pressure turbine blades of Adour MK811 engine, Project Report, Bachelor of Engineering, Department of Aeronautical Engineering, Kumaraguru College of Technology, Coimbatore-49, India, April 2011.

7. P. Zhang, K. Yuan, R. L. Peng, X.-H. Li, S. Johansson. Long-term oxidation of MCrAlY coatings at 1000 C and an Al-activity based coating life criterion // Surface and Coatings Technology. – 2017. -Vol. 332. -No.25. -P. 12-21. https://doi.org/10.1016/j.surfcoat.2017.09.086

8. H.S. Nithin, Vijay Desai, M.R. Ramesh. Elevated temperature solid particle erosion behaviour of carbide reinforced CoCrAlY composite coatings // Materials Research Express. -2018. -Vol. 5. -P. 066529. https://doi.org/10.1088/2053-1591/aac998

9. G.A. Bleykher et al. Features of copper coatings growth at high-rate deposition using magnetron sputtering systems with a liquid metal target // Surface and Coatings Technology. – 2017. – Vol. 324. – P. 111–120. https://doi.org/10.1016/j.surfcoat.2017.05.065

10. A.V. Yuryeva et al. Effect of material of the crucible on operation of magnetron sputtering system with liquid-phase target // Vacuum. – 2017. – Vol. 141. – P. 135– 138. https://doi.org/10.1016/j.vacuum.2017.04.001

11. B. Rakhadilov, M. Maulet, M. Abilev, Z. Sagdoldina, R. Kozhanova. Structure and tribological properties of Ni–Cr–Al-Based gradient coating prepared by detonation spraying // Coatings. – 2021. -Vol. 11. -P. 218. https://doi.org/10.3390/coatings11020218

12. 12. H. Ikezi. Coulomb solid of small particles in plasmas // The Physics of Fluids. – 1986. – Vol. 29. – N. 6. – P. 1764-1766. https://doi.org/10.1063/1.865653

13. 13. L. Wang, X.H. Zhong, Y.X. Zhao, S.Y. Tao, W. Zhang, Y. Wang, X.G. Design and optimization of coating structure for the thermal barrier coatings fabricated by atmospheric plasma spraying via finite element method // Journal of Asian Ceramic Societies. -2014. -Vol. 2. -P.102-116. https://doi.org/10.1016/j.jascer.2014.01.006

14. 14. S. A. Khrapak, B. A. Klumov, P. Huber, V. I. Molotkov, A. M. Lipaev, V. N. Naumkin, A. V. Ivlev, H. M. Thomas, M. Schwabe, G. E. Morfill, O. F. Petrov, V. E. Fortov, Y. Malentschenko, S. Volkov. Fluid-solid phase

transitions in three-dimensional complex plasmas under microgravity conditions // Physical Review E. -2012. -Vol. 85. -N. 6. -P. 66-75. https://doi.org/10.1103/PhysRevE.85.066407

15. 15. I. Tacikowski, I. Sutkowski, J. Senatorski, J. Michalski. Modyfikowane warstwy azotowane wytwarzane w procesie regulowanym. porfczonym z utwardzaniem cieplnym podtoza // Inzynieria Materialowa. -2000. –Vol. 22. – P. 449-452. (in Polish).

16. 16. A. Karakurkchi, N. Sakhnenko, R. Atchibayev. Research on the improvement of mixed titania and Co(Mn) oxide nano-composite coatings // IOP Conference Series: Materials Science and Engineering. -2018. – P. 69-74.

17. 17. M. Ved' , N. Sakhnenko, I. Yermolenko. Composition and corrosion behavior of iron-cobalt-tungsten // Eurasian Chemico-Technological Journal. -2018. -Vol.20(3).- P. 145-152.

18. 18. G. Yar-Mukhamedova, N. Sakhnenko. Nano-composition Ti-Co(Mn) coatings investigation // International Multidisciplinary Scientific GeoConference Surveying Geology and Mining Ecology Management, SGEM. -2018. –P. 1-15

19. 19. A. Zhilkashinova, M. Abilev, A. Pavlov, N. Prokhorenkova, M. Skakov, A. Gradoboev, A. Zhilkashinova. Ion-plasma spraying and electron-beam treatment of composite Cr-Al-Co-ZrO_2-Y_2O_3 coating on the surface of Ni-Cr alloy, coatings. -2021. -Vol.11(3). -P. 321. https://doi.org/10.3390/coatings11030321

20. 20. A. Zhilkashinova, M. Skakov, A Zhilkashinova, A. Gradoboyev. Multilayer ion-plasma coating CR-AL-CO-Y and its phase composition // Reports of the national academy of sciences of the Republic of Kazakhstan. -2021. –Vol. 4.–No. 338. – P. 158 – 166. https://doi.org/10.32014/2021.2518-1483.73

21. 21. A. Zhilkashinova, M. Skakov, A. Zhilkashinova, I. Ocheredko. Computational – experimental method of forecasting the lifetime of CO-CR-Al-Y composite coatings // Reports of the national academy of sciences of the Republic of Kazakhstan. -2022. -Vol. 1. -N. 341. –P. 117–123. https://doi.org/10.32014/2022.2518-1483.140

22. 22. S.Klemme, J.C. Miltenburg. The heat capacities and thermodynamic properties of $NiAl_2O_4$ and $CoAl_2O_4$ measured by adiabatic calorimetry from T = (4 to 400) K // Journal of Chemical Thermodynamics. -2009. -Vol. 41. -P. 842–848

23. 23. J. Li, X. Zhou, Y. Liu, Y. Chen, J. Zhang, R. Huang, J. Tan, Z. Li, B. Yang. Effects of different post-treatments on arc erosion resistance of cold-sprayed AgC composite electric contact // *Coatings.* -2021. -Vol. *11.* -P. 363. https://doi.org/10.3390/coatings11030363

Funded by Al-Farabi KazNU

IRSTI 29.17.15; 29.17.35; 29.03.77 https://doi.org/10.26577/phst.2022.v9.i1.07

Instability of mechanical equilibrium and some features of concentration convection in isothermal ternary gaseous systems

A. Zhussanbayeva , V.N. Kossov* , O.V. Fedorenko and M. Zhaneli

Abai Kazakh National Pedagogical University, Almaty, Kazakhstan,
*e-mail: kosov_vlad_nik@list.ru

(Received 11 April 2022; received in revised form 23 May; accepted 18 June 2022)

Empirical research of the formation of convection streams in a ternary gaseous compound He + R12 – Ar at various pressures and concentrations of the miscible components has been implemented. Experimental data obtained have demonstrated that the intensiveness of convection streams increases with increasing pressure. It is noted that in the system under consideration, the initiation of convection streams is possible when the content of Freon-12 in the mixture is more than 0.1 mole fraction. A numerical study of the unstableness of mechanical balance in the mixture He + R12 – Ar with significantly different diffusion coefficients of gas mixture components has been carried out by means of the splitting scheme in terms of physical parameters. The presented mathematical model makes it possible to describe the process of formation of a convective structure for various compositions of mixture. The onset of instability is accompanied by the formation of curved concentration profiles. Within the numerical framework, the onset times of various mixing regimes are determined.

Keywords: diffusion, convection, gas mixtures.
PACS numbers: 51.20.+d, 51.10.+y

1 Introduction

Convective motions in a single-component medium where density has monotonous temperature dependence are researched carefully and reported in [1-4]. Mentioned works present approaches, which allow for channels of various geometric shapes to investigate free gravitational convection, which makes it possible to predict mixing modes for specific conditions. For single-phase systems, the occurrence of thermoconcentration gravitational flows is the heterogeneity of the density of medium caused by temperature variations. The directions of the force of gravity and the density gradient of the medium have a significant effect on the formation of convective instability. In this case, the medium has a stable stratification if the gravity and density gradient vectors are codirectional. This situation does not contribute to the emergence of convective flows.

In binary non-isothermal mixtures, it is necessary to take into account diffusion, which leads to additional mechanisms for the occurrence and development of convective flows [5, 6]. One of the features of the research, which conducted in [5, 6] was the assumption, that heat and dissolved matter as components affecting the general medium density distribution. It follows from this that for multicomponent mixtures, convective separation effects will also appear, the reason of occurrence of which is distinction between the interdiffusion constants of the mixture constituents. Finding out of the influence of the constituents' diffusibility is possible when studying isothermal mixing. Experimental and numerical data of multicomponent gas mixtures [7-14] have shown that the unstableness of mechanical balance of the mixture may be realized under the condition of a decrease in density with height. This condition is not representative when studying the thermal convection problems described in [1-5] for single-component systems. For such situations, the component with the highest molar mass was transferred more intensively, which was noted by the authors of the work [15]. Thus, when solving problems of complex mass transfer, it is necessary to pay special attention to problems aimed at studying and clarifying the conditions under which it is possible to separate a component with certain properties during multicomponent mixing.

Purpose of the article is an empirical research of the unstableness of mechanical balance and the

change of modes of "diffusion – concentration gravitational convection" in an isothermal three-component helium – Freon – argon gas mixture at various pressures and compositions for a case when the mixture density deflates with altitude change. The regime change "diffusion – concentration gravitational convection" border is defined. A comparison of the computation data with the empirical results is implemented.

2 Experiment

A ternary mixture of gases He (1) + R12 (2) – Ar (3) was subject to study at different contents of Freon-12 in the mixture. The order of the components in the mixture under study is indicated by the quantity in parentheses. The composition of the initial mixtures was selected in such a way that the investigated mixture was hydrostatically stable when the immixture process started.

The divided transport of constituents was carried out in an experimental device that implements the two-flask method. The diffusion cell consists of two flasks (an upper one with volume V_u and a lower one with volume V_l) connected by a vertical cylindrical channel (see Fig. 1a). The geometric characteristics of a diffusion cell with a cylindrical channel have the following values: V_l = (214.5 ± 0.5)×10^{-6} m^3, V_u = (226.8 ± 0.5)×10^{-6} m^3, L = (165.00 ± 0.05)×10^{-3} m. The studies were fulfilled at a constant temperature equal to 298.0 K and pressures within (0.15 – 0.60) MPa. The pressure and the temperature measurement accuracy was 0.02 MPa and 0.1 K respectively. Measurement of the concentration of components was implemented by gas chromatography. The error in measuring the concentration did not exceed 1–3%.

Operation method on the experimental bench was described in detail for similar devices in [16], so we will dwell on the main procedures that allow us to obtain experimental data for the mixture under study. The upper flask 2 through the system of valves 9, 11 and the pressure gauge 7 is filled with the initial mixture from the cylinder 5 to a predetermined pressure. A similar procedure for filling gas the lower flask 3 of the apparatus from the cylinder 6 with is carried out through the manometer 8 and the system of valves 10, 12. After fixing the experiment pressure, the valves 9, 11 and 10, 12 are blocked. The mixing of gases through the connecting channel of a given geometry 1 occurs when the valve 4 is opened with simultaneous registration of time. When the experiment is finished, the valve 4 is closed and the mixing time is fixed. Then the studied mixtures are fed to the outlets 15, and then transported to the chromatograph for analysis.

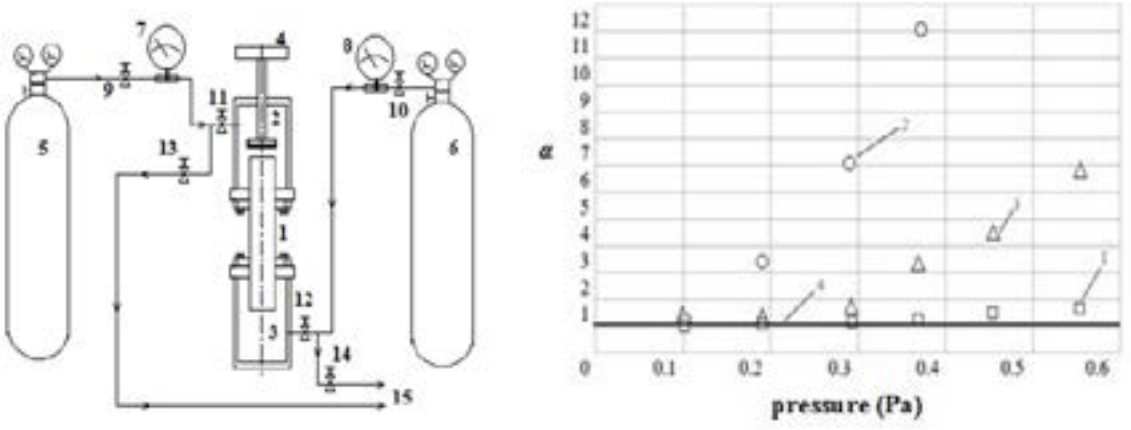

a) (b)

Figure 1 – Experimental studies of the unstableness of mechanical balance in triple gas mixtures: (a) Experimental setup [17]; (b) Pressure dependence of the factor α for the system 0.7 He (1) + 0.3 R12 (2) – Ar (3), T = 298.0 K: 1 – helium, 2 – Freon-12, 3 – argon, 4 – calculation assuming diffusion

During experiments, it was supposed to study the mixing of a two-component system arranged in the top flask 2 with a pure constituent located in the bottom flask 3 (see Fig. 1a). To exclude convective mechanisms caused by the unstable density stratification of the system [1-5], the lighter (in terms of density) binary mixture was located above the heavy gas. Thus, the condition of the negative direction of the density gradient was initially formed, under which the implementation of the diffusion type of mixing without convective disturbances is possible. The placement of the mixture components relative to the diffusion channel associated with the opposite direction of the change in density per unit length was not considered. The duration of the experiment at predetermined temperature and pressure was 60 minutes. Such mixing times provided sufficient values for the diffused concentrations of the components, which made it possible to carry out chromatographic analysis.

The experimental concentration values c_{exp} were normalized to the theoretical values c_{theor} calculated in the diffusion approximation using the Stefan-Maxwell equations [18]. Figure 1b indicates a typical pressure relationship of the nondimensional factor $\alpha = c_{exp} / c_{theor}$ for the analyzed system. An analysis of the data presented in this figure shows that in the pressure range up to 0.15 MPa, diffusion occurs in the system. It is confirmed by the fact that all constituents of the considered system have the value of the nondimensional factor α_i equal to one. For each component of the mixture, the parameter α_i starts to raise when an experimental pressure equals to 0.15 MPa. A particularly significant increase was noted for Freon-12 and, to a lesser extent, for the most diffusively mobile He. Thus, the transition from diffusion to convective mixing is possible when the pressure in the experiment is equal to or exceeds 0.15 MPa. The growth of the rate of convective flows formation is associated with a subsequent raise in pressure. The type of mixing in which the intensity of mixing decreases with increasing pressure is not representative when studying diffusion process. Distributions similar in form were also observed for other primary combinations of the systems. If the Freon-12 content in the initial mixture is less than 0.1 mole fraction, diffusion occurs in the system. The α_i parameters for each component will be approximately equal to one.

3 Numerical analysis

Let us consider the process of mixing in a cylindrical channel, in which the main diffusing components are diluted by the third component. Figure 2 explains the problem statement. A mixture of light gas 1 (with molar mass M_1) and heavy gas 2 (with molar mass M_2) contains in the upper part of channel S_1. This mixture diffuses into a gas with an intermediate molar mass M_3, which arranges in the section S_2 (where S_2 is the bottom region of channel).

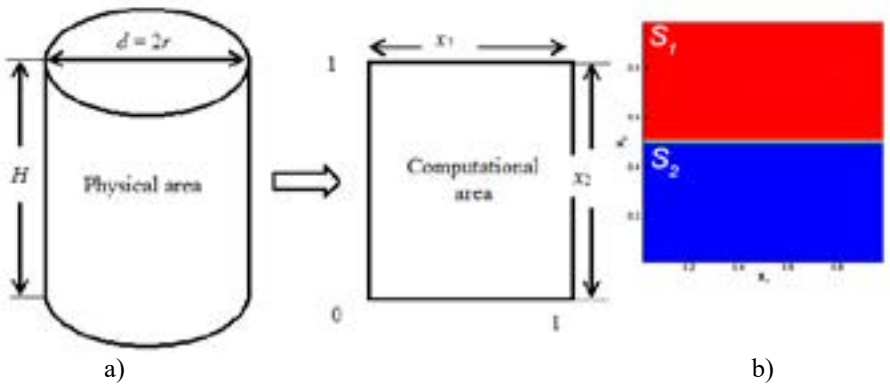

Figure 2 – Model of multicomponent diffusion: (a) Natural and numerical regions of immixture; (b) Placement of three-component system at the starting terms

The use of the Boussinesq approximation for a system of fluid dynamics equation written for disturbed quantities makes it possible to determine the conditions for three-component gas mixtures under which the transition from diffusion to convection is possible. The mentioned system of

equations is composed of the motion equation in the form of the Navier-Stokes equation, the equations of convective diffusion and the conservation equation of particles number in the mixture. When writing the considered system of equations, it is necessary to take into account the conditions of independent diffusion, which for a three-component system under the condition of constant temperature can be represented as follows $\sum_{i=1}^{3}\vec{j}_i = 0$ and $\sum_{i=1}^{3} c_i = 1$. Then the considered system of equations has the form [19]:

$$\rho\left[\frac{\partial\vec{u}}{\partial t}+(\vec{u}\nabla)\vec{u}\right]= \\ =-\nabla p+\eta\Delta\vec{u}+\left(\frac{\eta}{3}+\xi\right)\nabla\mathrm{div}\vec{u}+\rho\vec{g}$$

$$\frac{\partial c_1}{\partial t}+\vec{v}\nabla c_1=\mathrm{div}\left[D_{11}^{*}\nabla c_1+D_{12}^{*}\nabla c_2\right], \\ \frac{\partial c_2}{\partial t}+\vec{v}\nabla c_2=\mathrm{div}\left[D_{21}^{*}\nabla c_1+D_{22}^{*}\nabla c_2\right], \quad (1)$$

$$\frac{\partial n}{\partial t}=-\mathrm{div}\left(n\vec{v}\right),$$

where c_i is the concentration of the i-th component; D_{ij}^{*} are the practical diffusion coefficients; $\vec{g}$ is the gravity acceleration vector; n is the number density; p is the pressure; t is the time; $\vec{u}$ is the mass-averaged velocity; $\vec{v}$ is the mean-number velocity of the ternary mixture; ρ is the density; η and ξ are the shear and bulk viscosity coefficients.

The equation of medium state should be added to the system of equations (1):

$$\rho=\rho_0(1-\beta_1 c_1^{/}-\beta_2 c_2^{/}), \quad (2)$$

where $\beta_i=\frac{1}{\rho_0}\left(\frac{\partial\rho}{\partial c_i}\right)_{p,T,c_j}$; $c_i^{/}$ is the concentration perturbation of the i-th constituent.

The method of small perturbations is used when solving the system of equations (1). Using this method, the system under consideration is written for the perturbed quantities as:

$$\frac{\partial\vec{u}}{\partial t}+(\vec{u}\nabla)\vec{u}=-\frac{1}{\rho_0}\nabla p+\nu\nabla^2\vec{u}+g\left(\beta_1 c_1+\beta_2 c_2\right)\vec{\gamma},$$

$$\frac{\partial c_1}{\partial t}+\vec{v}\nabla\langle c_1\rangle=D_{11}^{*}\nabla^2 c_1+D_{12}^{*}\nabla^2 c_2, \\ \frac{\partial c_2}{\partial t}+\vec{v}\nabla\langle c_2\rangle=D_{21}^{*}\nabla^2 c_1+D_{22}^{*}\nabla^2 c_2, \quad (3) \\ \mathrm{div}\,\vec{v}=0,$$

where β_i is the factor specifying the i-th component concentration dependence of the gas mixture density, $\boldsymbol{\gamma}$ is the unitary vector, ν is the kinematic viscosity, ρ_0 is the average mixture density. $< c_i >$ is the invariable average of the concentration considering as the reference point.

The weight-average and number-average velocities have the disturbances of the same order of magnitude. Thus, it is possible to replace $\vec{v}$ by $\vec{u}$ when the diffusion channel length H is much more than the semidiameters r of the diffusion canal.

The combined equation (3) can be presented in the nondimensional form by means of the next measures: H for the specific linear size of the cave, H^2/ν for the time, D^{*}_{22}/H for the velocity, A_iH for the i-th component concentration, and $\rho_0\nu D^{*}_{22}/H^2$ for the pressure. Then equations (3) may be written as:

$$\frac{\partial\vec{u}}{\partial t}+\frac{1}{\mathrm{Pr}_{22}}\nabla\left(\vec{u}\cdot\vec{u}\right)= \\ =-\nabla p+\Delta\vec{u}+\left(\mathrm{Ra}_1\tau_{11}c_1+\mathrm{Ra}_2 c_2\right)\vec{\gamma},$$

$$\frac{\partial c_1}{\partial t}+\frac{1}{\mathrm{Pr}_{22}}\vec{u}\nabla c_1=\frac{1}{\mathrm{Pr}_{11}}\Delta c_1+\frac{1}{\mathrm{Pr}_{22}}\tau_{12}\Delta c_2, \\ \frac{\partial c_2}{\partial t}+\frac{1}{\mathrm{Pr}_{22}}\vec{v}\nabla c_2=\frac{A_1}{A_2}\frac{1}{\mathrm{Pr}_{22}}\tau_{21}\Delta c_1+\frac{1}{\mathrm{Pr}_{22}}\Delta c_2, \quad (4)$$

$$\mathrm{div}\,\vec{u}=0,$$

where $\mathrm{Ra}_i=g\beta_i A_i H^4/D_{22}^{*}\nu$ is the partial Rayleigh number, where A_i is the nondimensional primary gradient of the i-th component concentration, $\mathrm{Pr}_{ii}=\nu/D_{ii}^{*}$ is the diffusion Prandtl number, $\tau_{ij}=D_{ij}^{*}/D_{22}^{*}$ are the factors defining the dependence of practical diffusion coefficients.

The numerical solution of the system of equations (4) is based on the application of a splitting methods by physical quantities [20]. The problem is modeled in the rectangular coordinate system, in which a bidimensional region of the cylinder section with dimensions $H \times d$ is allocated. The considered cylindrical region with a height H and a diameter d is shown in Figure 2a. The calculations used a nondimensional grid 128 x 128, which made it possible to fix the concentration profiles corresponding to the onset and subsequent growth of convective flows.

We assume that initially convection and diffusion lead to the momentum transfer. To find the intermediate velocity field, the three-point double-sweep method is used. In this case, for the convective and diffusion members, which have the second order of accuracy in space, the explicit Adams-Bashforth scheme and the implicit Crank-Nicolson scheme are used [21, 22]. The discretization in space is implemented by the second-order accuracy. The pressure field is determined from the obtained intermediate velocity field by means of the Fourier method. The final recalculation of the velocity field is made on the assumption that the pressure gradient is the only cause of the transfer. Applying the Crank-Nicolson scheme and taking into account the found velocity field, the concentrations of the mixture components are determined using the three-point sweep method.

4 Numerical results

Figure 3 shows the results of a numerical calculation for the mixture 0.70 He (1) + 0.30 R12 (2) – Ar (3) at a pressure of 0.5 MPa and a temperature of 298 K, illustrating the change in the concentration of the heavy component of the mixture with time. The mixture placed at the top of the diffusion channel has a density less than the density of argon located at the bottom. The isoconcentration lines presented in Figure 3 show the following sequence of mixing modes. Figure 3a shows that at the initial time the diffusion process is implemented in the system. The components' concentration profile change in a monotonous manner. Further observation of the mixing dynamics shows that the components' concentration profile are curved (see Fig. 3b). This moment of time determines the unstableness of mechanical balance with the subsequent growth of convective disturbances. Over time, the isoconcentration lines continue to bend, and there are structural formations due to the fact that in the lower part of the computational domain the component concentration with a large molar mass increases. Subsequently, the convective structure detaches (see Fig. 3d) and moves in the diffusion channel in the gravity field. The performed computational investigation subject to pressure influence indicated that at the final stages of mixing, compound structured streams arise due to a significant bend of the concentration profiles with pressure growth. Moreover, the characteristic times of the onset of the corresponding mixing regimes decrease. Thus, the intensity of convective mixing increases with increasing pressure, which is also confirmed by the experimental data shown in Figure 1b.

5 Conclusions

An experimental study was carried out to define the conditions that determine the transition from a stable diffusion process to diffusion mixing with the formation of convective flows. For the experimental study of this transition, the experimentally measured concentrations were compared with the concentration values calculated using the Stefan-Maxwell equations. Such a comparison is presented as a pressure dependence of the nondimensional factor α.

Empirical results obtained for the mixture 0.70 He (1) + 0.30 R12 (2) – Ar (3) show that, starting from a pressure of 0.15 MPa, there is change of the diffusion mode to convective one due to the violation of the mechanical balance of the mixture. Examination of the change of nondimensional factor α subject to pressure indicated that the component with the large molar mass has the significant transference in the pressure range from 0.15 to 0.60 MPa. This behavior of Freon-12 concentration on pressure indicates an intensification of the convective flows rate.

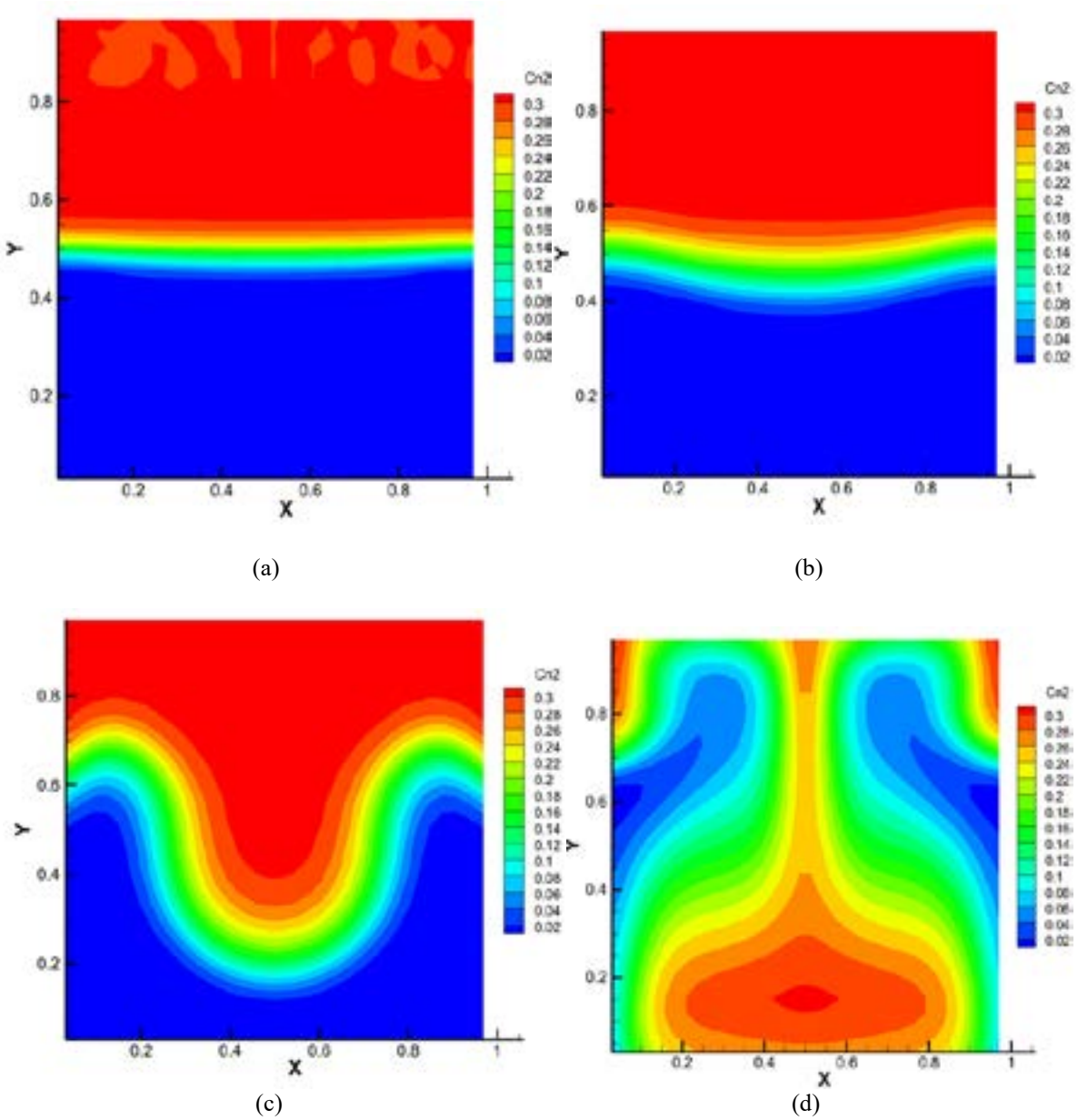

Figure 3 – Concentration profiles for the system 0.70 He (1) + 0.30 R12 (2) – Ar (3) at p = 0.5 MPa, T = 298.0 K, L = 0.165 m, r = 3.05×10^{-3} m: (a) t = 3.6 s; (b) t = 9.7 s; (c) t = 21.2 s; (d) t = 43.2 s

Within the framework of a numerical study, the dynamics of the formation of convective structures in the system 0.70 He (1) + 0.30 R12 (2) – Ar (3) at a pressure of 0.5 MPa was studied, at which, as shown by the experimental data presented in the work, a convective type of mixing is observed in the system. The curvature of the concentration profiles causes the initiation of unstability. The intense distortion of the components concentration profiles is associated with the pressure growth in the experiment.

Acknowledgments

This research has been funded by the Science Committee of the Ministry of Education and Science of the Republic of Kazakhstan (grant number AP09259248).

References

1. A. Bejan. Convection heat transfer. New York DC: Wiley Ed., 2004.
2. Y. Jaluria, K.E. Torrance. Computational heat Ttansfer. New York DC: CRC Press Ed., 2002.
3. Gershuni, G.Z. and Zhukhovitskii, E.M. Convective stability of incompressible fluids. Jerusalem: Keter Publishing House, 1976.
4. S. Chen, J. Tölke, M. Krafczyk. Numerical investigation of double-diffusive (natural) convection in vertical annuluses with opposing temperature and concentration gradients // Int. J. Heat and Fluid Flow. – 2010. – Vol. 31. – P.217-226. https://doi.org/10.1016/j.ijheatfluidflow.2009.12.013
5. M. Sankar, Y. Do. Numerical simulation of free convection heat transfer in a vertical annular cavity with discrete heating // Int. Comm. Heat Mass Transfer. – 2010. – Vol. 37. – P. 600-606. https://doi.org/10.1016/j.iicheatmasstransfer.2010.02.009
6. Y.-P. Hu, Y.-R.Li, M.-H. Li, L. Zhang, Si-Zh. Li. Effects of enclosure geometry and thermal boundary condition on Rayleigh-Benard convection of cold water near its maximum density // Int. J. Therm. Sci. -2017. -Vol. 120. -P. 220-232. https://doi.org/10.1016/j.ijthermalsci.2017.06.013
7. V.V. Dil'man, D.A. Lipatov, V.A. Lotkhov, V.A. Kaminskii. Instability in unsteady-state evaporation of binary solutions into an inert gas // Theor. Found. Chem. Engin. – 2005. – Vol. 39. – No. 3. – P. 566-572. https://doi.org/10.1007/s11236-005-0118-0
8. V.V. Dil'man, V.A. Lotkhov. Molecular turbulent evaporation in a gravitational field // Theor. Found. Chem. Engin. – 2015. – Vol. 49. – No. 1. – P. 102-106. https://doi.org/10.1134/S0040579515010017
9. V. Kossov, O. Fedorenko, D. Zhakebayev. Features of multicomponent mass transfer in gas mixtures containing hydrocarbon components // Chem. Eng. Technol. 2019. – Vol. 42. – No. 4. – P. 896-902. https://doi.org/10.1002/ceat.201800604
10. V.A. Kaminskii. Special modes of three-component diffusion in gases // Rus. J. Phys. Chem. A. – 2011. – Vol. 85. No. 12. – P. 2203-2208. https://doi.org/10.1134/S0036024411120156
11. V.A. Kaminskii, N.Yu. Obvintseva. Evaporation of a liquid under the conditions of convective instability in the gas phase // Russ. J. Phys. Chem. A. – 2008. – Vol. 82. – No. 7. – P. 1215–1220. https://doi.org/10.1134/S0036024408070297
12. O.E. Aleksandrov. Equation of convective diffusion of a multicomponent mixture in a capillary for an arbitrary velocity field // Fluid Dynamics. – 2006. – Vol. 41. – No. 6. – P. 976-983. https://doi.org/10.1007/s10697-006-0112-1
13. T.P. Lyubimova, N.A. Zubova. Onset of convection in a ternary mixture in a square cavity heated from above at various gravity levels // Microgravity Sci. Technol. – 2014. – Vol. 26. – P. 241-247. https://doi.org/10.1007/s12217-014-9383-z
14. G.A. Ruev, A.V. Fedorov, Fomin, V.M. "Description of the Anomalous Rayleigh-Taylor Instability on the Basis of the Model of Dynamics of a Three-Velocity Three-Temperature Mixture". *J. Appl. Mech. Tech. Phys*. Vol. 50, no. 1 (2009): 49-57. https://doi.org/10.1007/s10808-009-0007-0
15. Kosov, V.N., Seleznev, V.D., Zhavrin, Yu.I. "Separation of Components during Isothermal Mixing of Ternary Gas Systems under Free-Convection Conditions". *Tech. Phys.* Vol. 42, no. 10 (1997): 1236-1237. https://doi.org/10.1134/1.1258905
16. Asembaeva, M.K., Kosov, V.N., S.A. Krasikov, O.V. Fedorenko. Effect of the channel inclination angle on convective mixing caused by instability of mechanical equilibrium of ternary gas mixture at isothermal diffusion // Tech. Phys. Letters. – 2019. – Vol. 45. – No. 21. – P. 1071–1074. https://doi.org/10.1134/S1063785019110038
17. V. Kossov, O. Fedorenko, A. Kalimov, A. Zhussanbayeva. Diffusion mechanisms for the occurrence of the instability of mechanical equilibrium of a ternary gas mixture containing carbon dioxide // Fluids. – -2021. – Vol. 6. – No. 5. – P. 177. https://doi.org/10.3390/fluids6050177
18. R.B. Bird, W.E. Stewart, E.N. Lightfoot. Transport Phenomena. New York DC: John Wiley & Sons Ed., 2007.
19. V. Kossov, S. Krasikov, O. Fedorenko. Diffusion and convective instability in multicomponent gas mixtures at different pressures // Eur. Phys. J. Special Topics. – 2017. – Vol. 226. – P. 1177-1187. https://doi.org/10.1140/epjst/e2016-60201-1
20. I.M. Navon. Pent: A periodic pentodiagonal systems solver // Commun. Appl. Num. Meth. – 1987. – Vol. 3. – No. 1. – P. 63-69.
21. J. Kim, P. Moin. Application of a fractional-step method to incompressible Navier-Stokes equations // J. Comput. Phys. – 1985. – Vol. 59. – No. 2. – P. 308-323. https://doi.org/10.1016/0021-9991(85)90148-2
22. B.T. Zhumagulov, D.B. Zhakebayev, A.U. Abdibekova. The decay of MHD turbulence depending on the conducting properties of environment // Magnetohydrodynamics. – 2014. – Vol. 50. – No. 2. – P. 121-138. http://doi.org/10.22364/mhd

Funded by Al-Farabi KazNU

CONTENTS